Collisions

Collision Cross section

Collision rate coefficient

Reaction Cross section

Reaction rate coefficient

Electron collisions

Rutherford atom

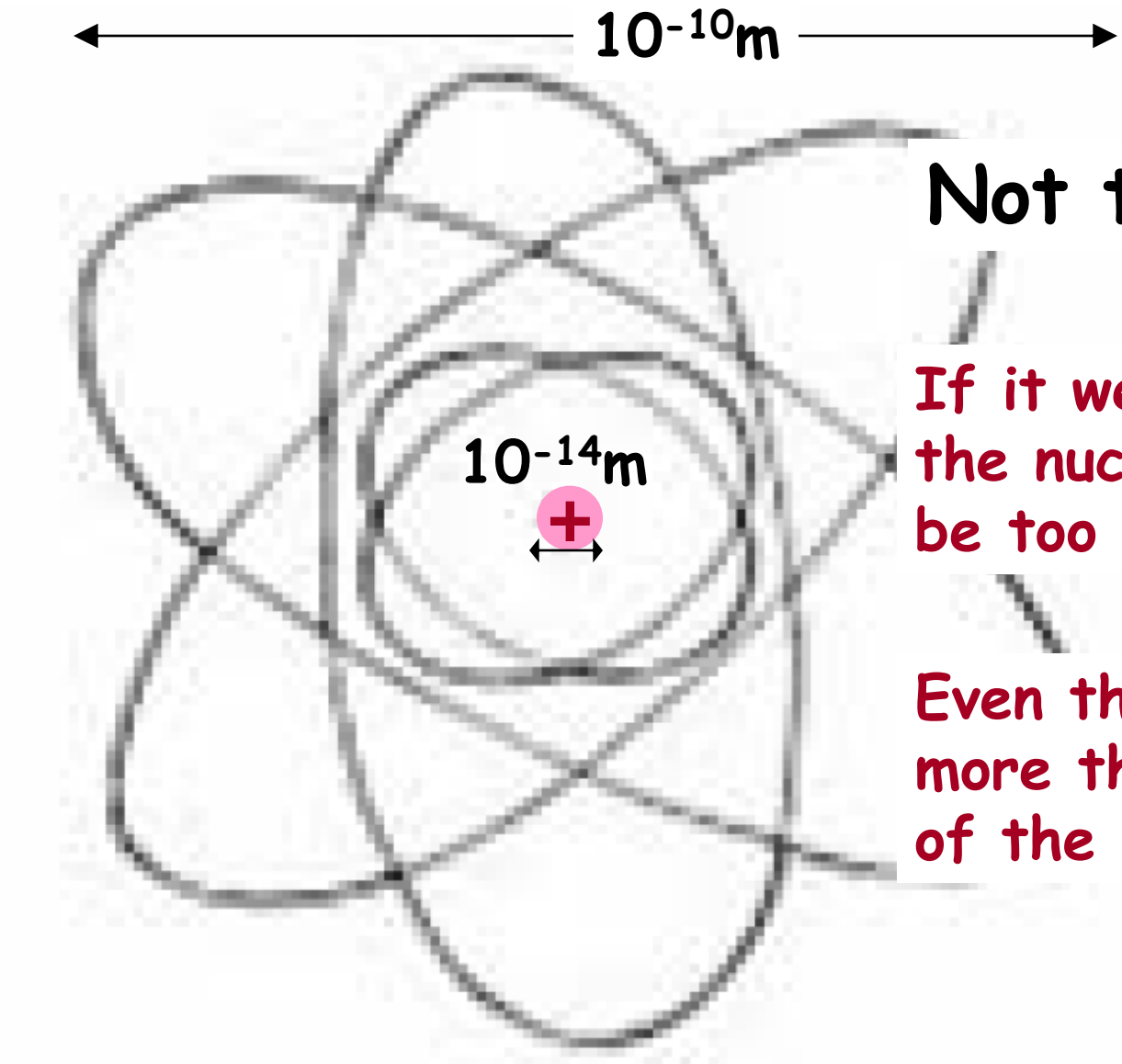

Not to scale!!!

If it were to scale, the nucleus would be too small to see

Even though it has more than 99.9% of the atom's mass

Collisions in plasma

Reactions in plasma

Interactions of particles in plasma

Collisions of electrons with atoms

De Broglie wave length

$$\lambda_{DB} = \frac{h}{p} = \frac{h}{Mv} \sim \frac{h}{\sqrt{MT}}$$

Classical or quantum approach?

$$\lambda_e(4K) \sim 540\,A \sim 54x10^{-9}\,m$$

Electron:

1eV → v=5.9x10^{7}cm s^{-1}

$\tau \sim a_0/v \sim 10^{-8}/\ 5.9x10^7 = 2x10^{-16}$s

$\lambda \sim 2A = 2x10^{-8}$cm de Broglie

Ar+:

1eV → v=2x10^{5}cm s^{-1}

$\tau \sim a_0/v \sim 10^{-8}/\ 2x10^5 \sim 6x10^{-14}$s

$\lambda \sim 9x10^{-11}$cm de Broglie

Collisions of electrons with atoms

Classical or quantum approach?

Electron:

1eV → $v=5.9\times10^{7}$cm s^{-1}

$\tau\sim a_0/v \sim 10^{-8}/ 5.9\times10^{7}=2\times10^{-16}$s

$\lambda\sim 2A = 2\times10^{-8}$cm de Broglie

Ar+:

1eV → $v=2\times10^{5}$cm s^{-1}

$\tau\sim a_0/v \sim 10^{-8}/ 2\times10^{5}\sim 6\times10^{-14}$s

$\lambda\sim 9\times10^{-11}$cm de Broglie

H_3^* + e at 10 K ????

$$\lambda_e(4K) \sim 540\,A \sim 54x10^{-9}\,m$$

Rydberg atom

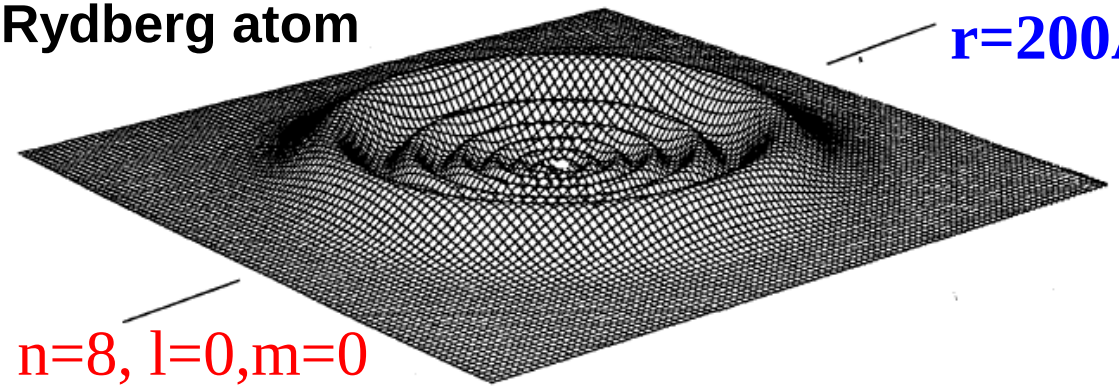

De Broglie wave length

$$\lambda_{DB} = \frac{h}{p} = \frac{h}{Mv} \sim \frac{h}{\sqrt{MT}}$$

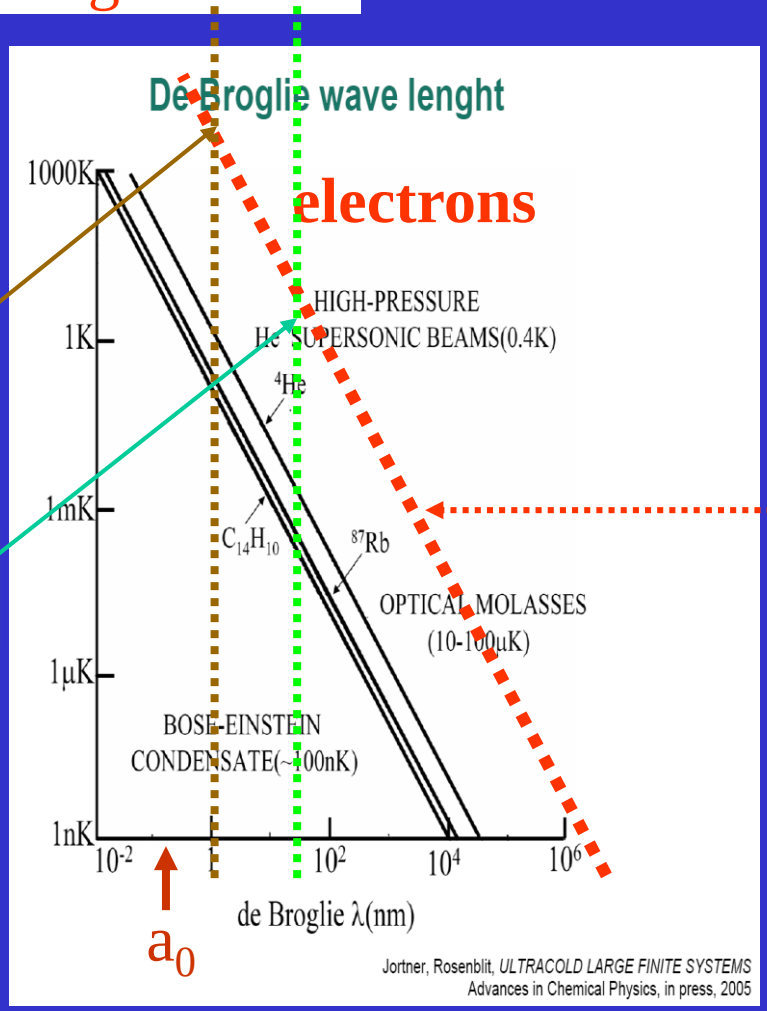

1eV

$$\lambda_{eDB}(1eV) \sim 11.6\,A \sim 1.16x10^{-9}\,m$$

4K

$$\lambda_{eDB}(4K) \sim 540\,A \sim 54x10^{-9}\,m$$

$$\lambda_{DB} = \frac{h}{m_e v_e} \sim \frac{h}{\sqrt{m_e T}}$$

$$T \sim= \frac{1}{\lambda_{DB}^{\,2}}$$

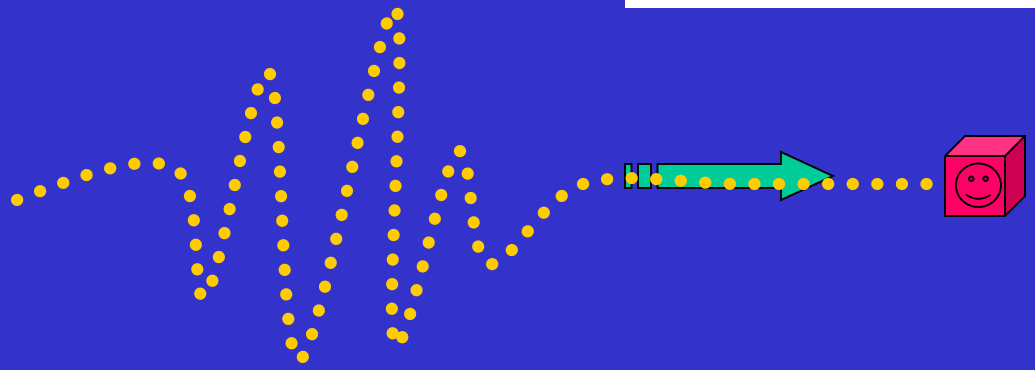

"Electron-Driven Processes: Scientific Challenges and Technological Opportunities"

1. Workshop on "Fundamental Challenges in Electron-Driven Chemistry", Berkeley, October 9 & 10, 1998
   Organizers: C. William McCurdy, Lawrence Berkeley National Laboratory
   Thomas N. Rescigno, Lawrence Livermore National Laboratory

(1998)

Current Status and Future Perspectives of Electron Interactions with Molecules, Clusters, Surfaces, and Interfaces

Kurt H. Becker, Stevens Institute of Technology (SIT)
C. William McCurdy, Lawrence Berkeley National Laboratory (LBNL)
Thomas M. Orlando, Pacific Northwest National Laboratory (PNNL)
Thomas N. Rescigno, Lawrence Livermore National Laboratory (LLNL)
and Lawrence Berkeley National Laboratory (LBNL)

This report can be found on the World Wide Web at:
http://attila.stevens-tech.edu/physics/People/Faculty/Becker/EDP

Other related reports can be found at the following web sites:
http://www.lbl.gov/ICSD/mccurdy/epic_home.htm
http://www.er.doe.gov/production/bes/chm/RadRprt.doc

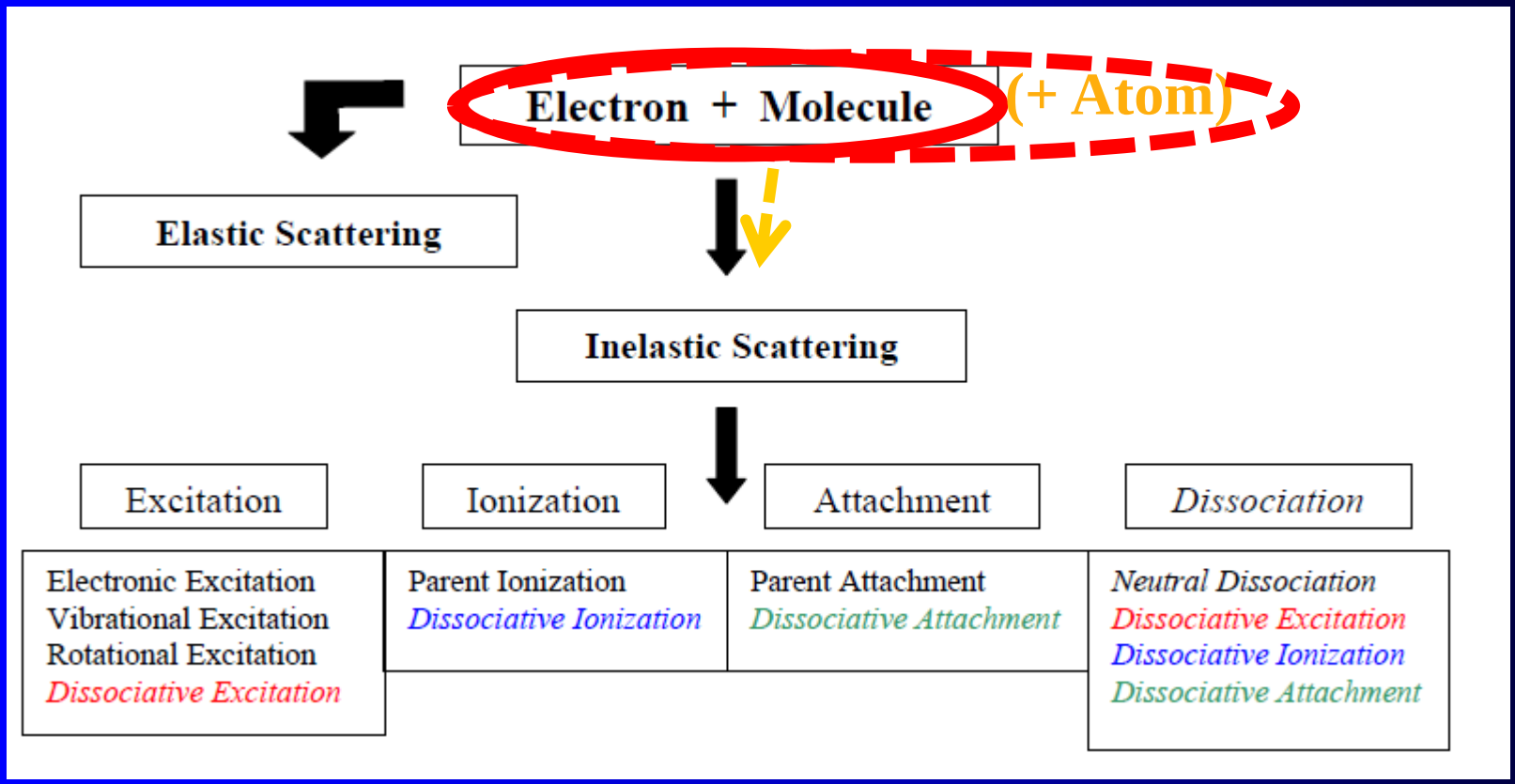

$H_2^+ + Ar \Rightarrow ArH^+ + H$

Single collision

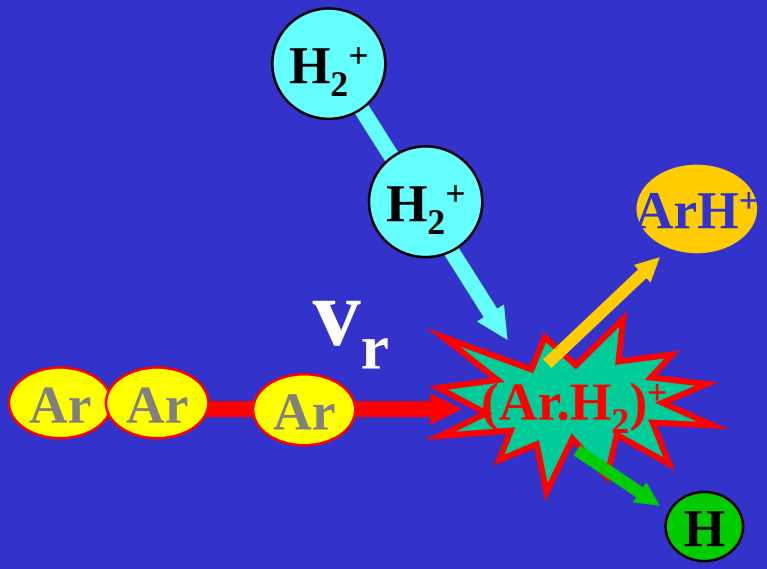

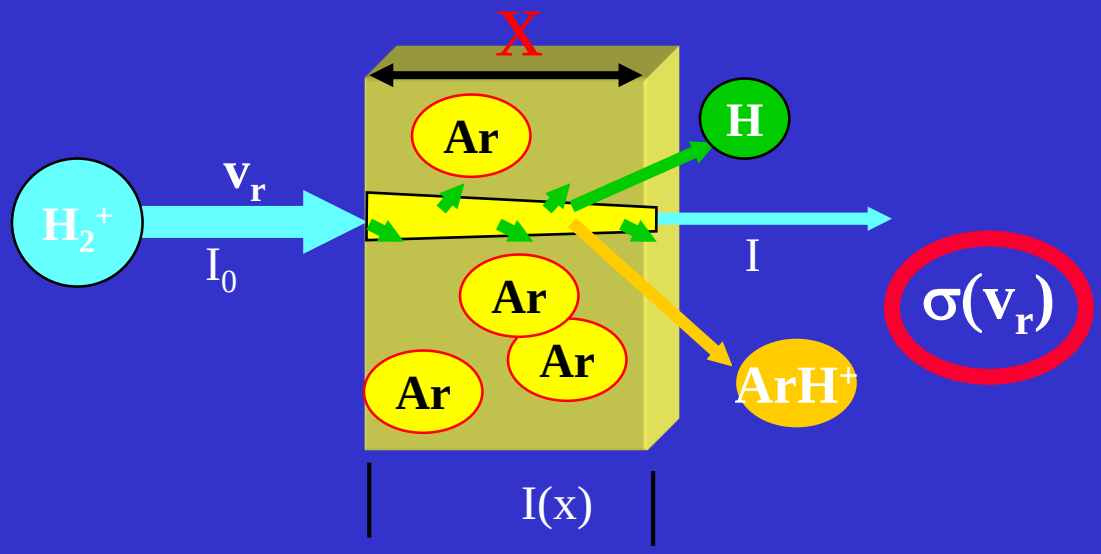

Reaction cross section

Collisional cross section

$$I = I_0 \exp(-\sigma n_{Ar} x)$$

Single collision

$$H_2^+ + Ar \Rightarrow ArH^+ + H$$

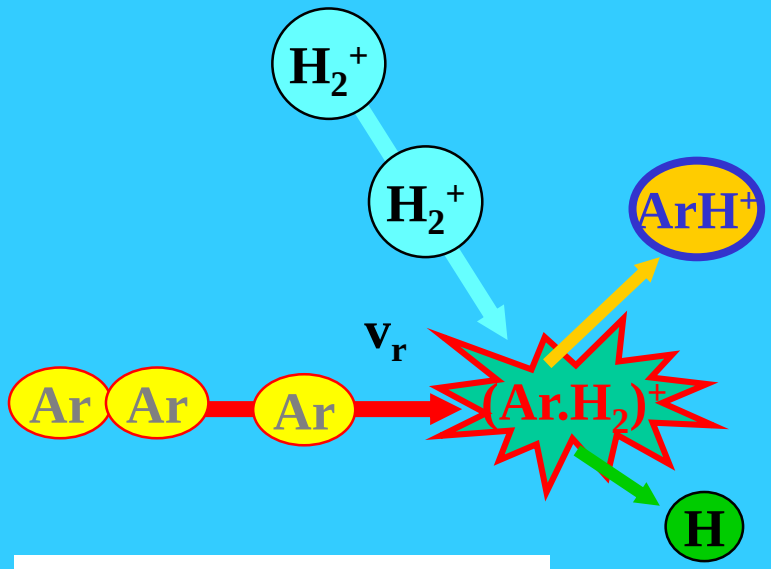

reaction cross section

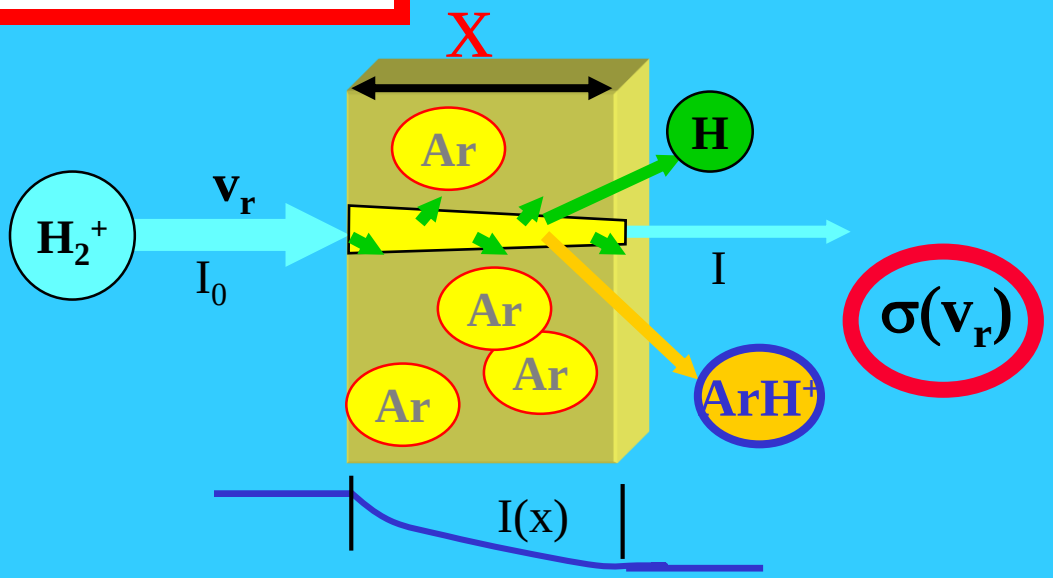

$$I = I_0 \exp(-\sigma n_{Ar} x)$$

$$\nu_{coll} = +nV_{rel} = +n\nu S = +n\nu\pi\delta^2 = +n\nu\sigma$$

Collisional cross section

$$\frac{dI}{dt} = -\frac{I}{\tau_{coll}} = -I\nu_{coll}$$

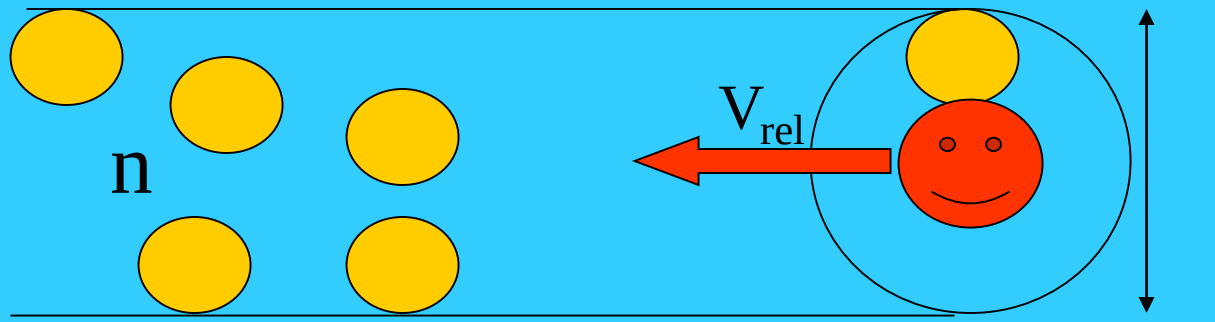

$$I(t) = I_0 \exp(-\nu_{coll} t) = I_0 \exp(-\sigma n \nu_{rel} t)$$

$$I = I_0 \exp(-\sigma n_{Ar} x)$$

Single collision

$$H_2^+ + Ar \Rightarrow ArH^+ + H$$

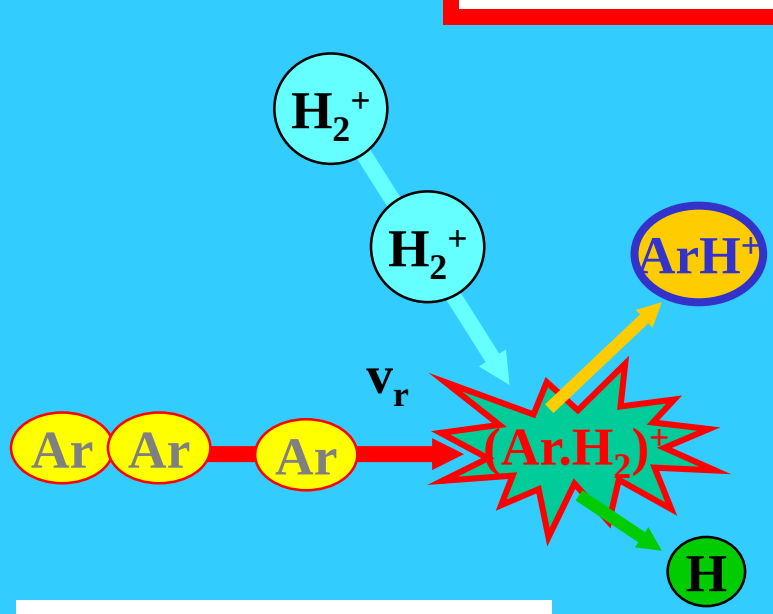

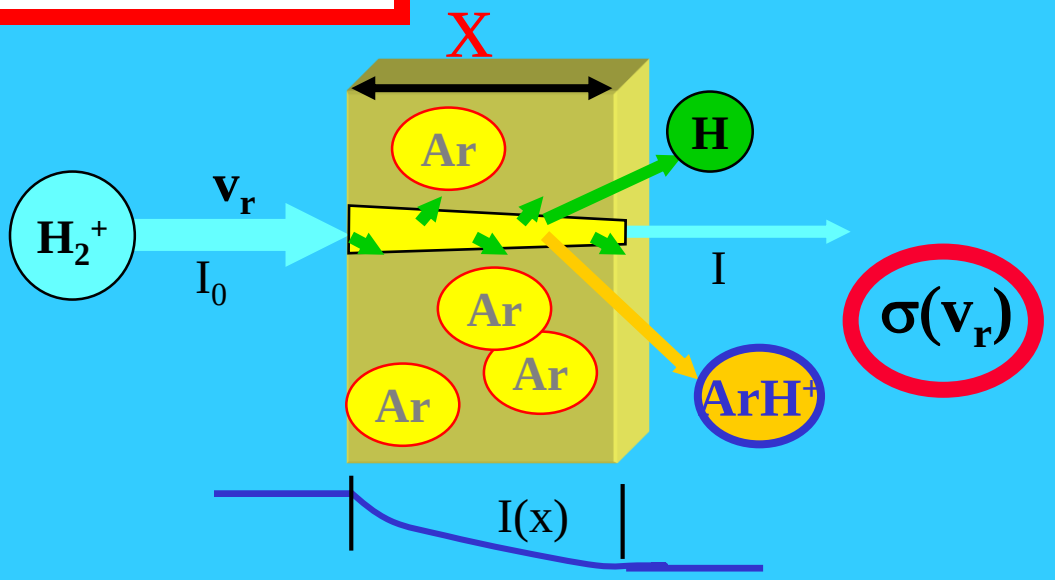

reaction cross section

$$I = I_0 \exp(-\sigma n_{Ar} x)$$

Proportionality factor

$$\frac{dI}{dx} \sim -INx \qquad \frac{dI}{dx} = -\sigma INx$$

$$\frac{dI}{Idx} = \frac{d\ln(I)}{dx} = -\sigma Nx$$

$$I(x) = I_0 \exp(-\sigma Nx)$$

Impact ionization

2.3. Electron impact ionization

The electron impact ionization is the most fundamental ionization process for the operation of ion sources.

Why?

- The cross section for the impact ionization is by orders of magnitudes higher than the cross section for the photo ionization.
- The cross section depends on the mass of the colliding particle. Since the energy transfer of a heavy particle is lower, a proton needs for an identical ionization probability an ionization energy three orders of magnitudes higher than an electron

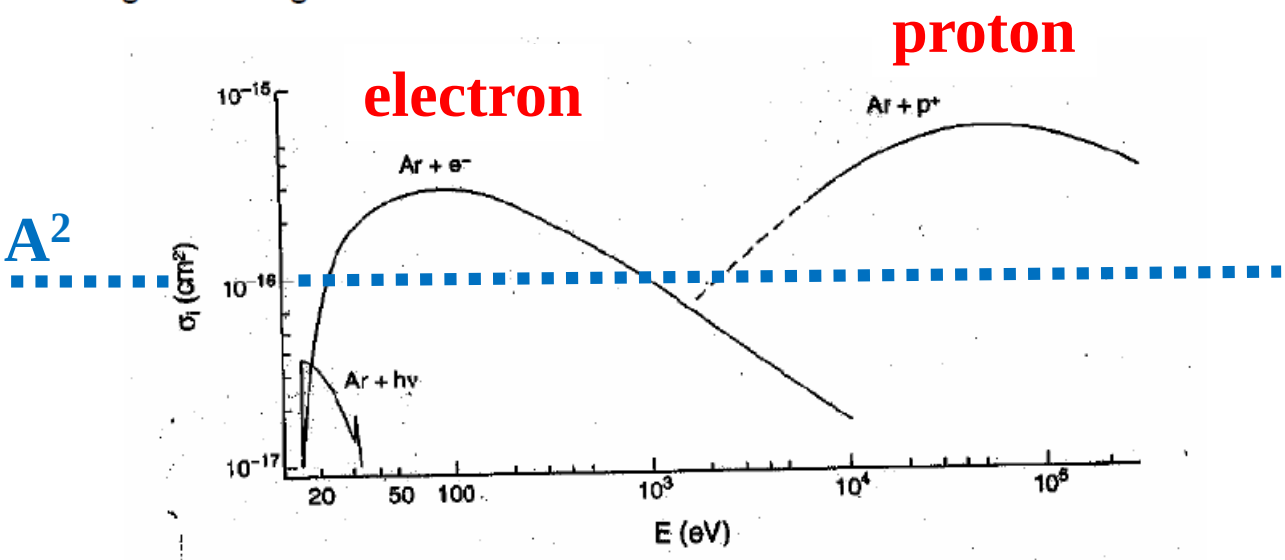

FIGURE 4
Ionization cross sections as functions of energy for ionizing collisions with fast electrons, protons, and photons. (From Winter, H., in *Experimental Methods in Heavy Ion Physics*, Springer-Verlag, [illegible]. With permission.)

Cross section

$$A^+ + B \rightarrow C^+ + D$$

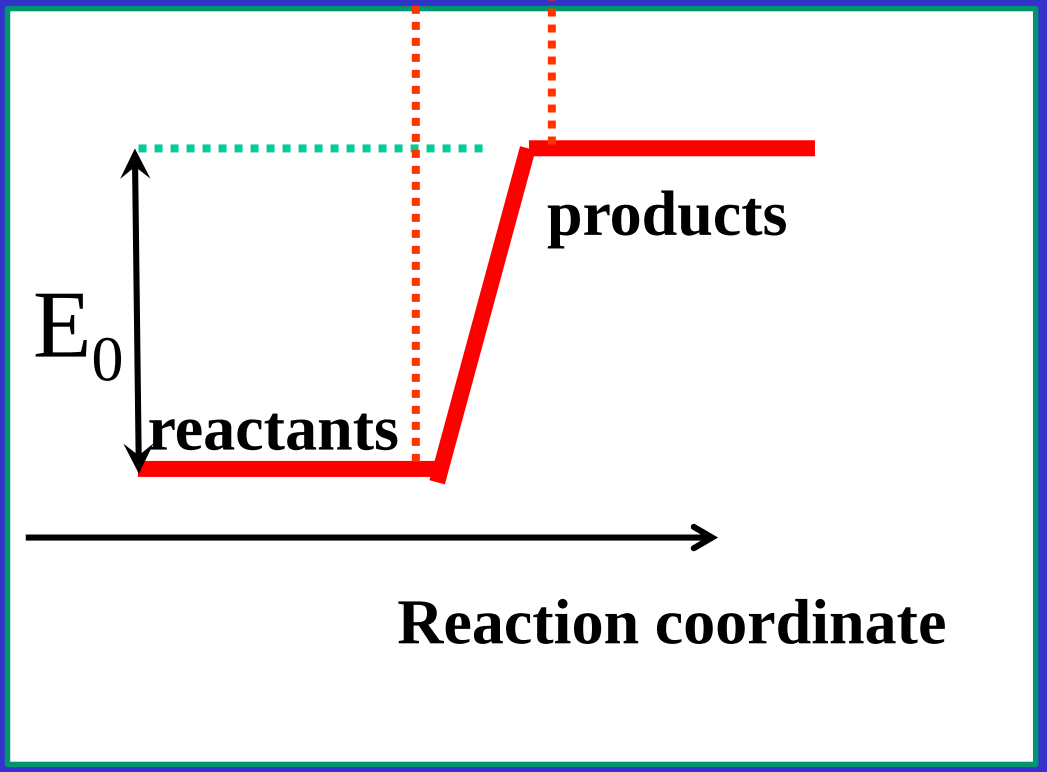

Reaction cross section

Collisional cross section

Cross sections for vibrational excitation, dissociation, ionization…H_2

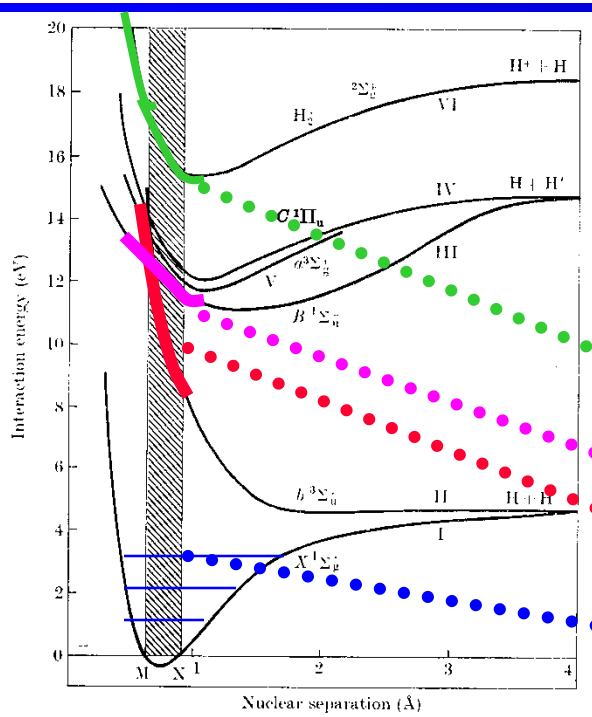

FIG. 13.1. Potential energy curves for electronic states of H_2 and H_2^+ lying within 20 eV of the ground state.

H_2 + e

→ $H_2(v)$ + e ……. Vibrational excitation

→ H + H +e……. Dissociation

→ H_2^* + hν + e … Photon excitation

→ H_2^+ +e + e….. Ionization

→ H^+ + H + e + e Dissociative Ionization

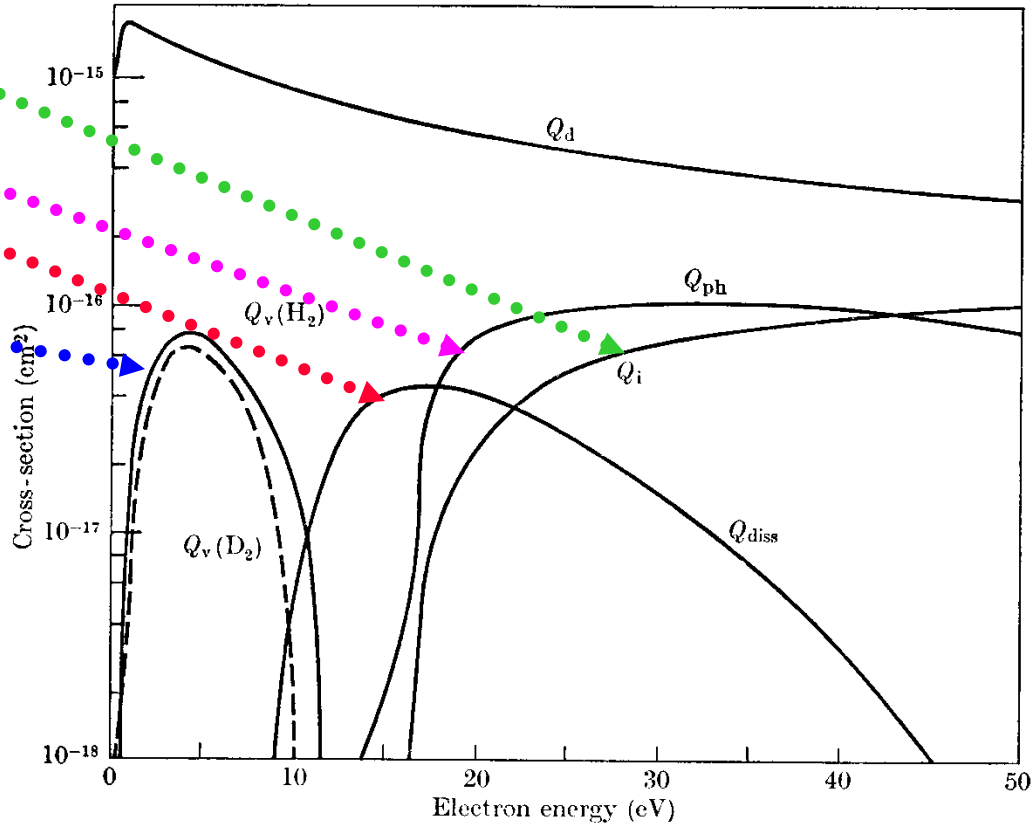

FIG. 13.37. Cross-sections assumed by Engelhardt and Phelps in their analysis of swarm data in H_2 and D_2 for electrons of characteristic energy greater than 1 eV. Q_d momentum-transfer cross-section, Q_i, ionization cross-section, Q_{diss} dissociation cross-section, Q_{ph} photon excitation cross-section, Q_v vibrational excitation cross-section (—— H_2, ——— D_2).

Details of interaction of electron with H_2 (1990)

Probability .....

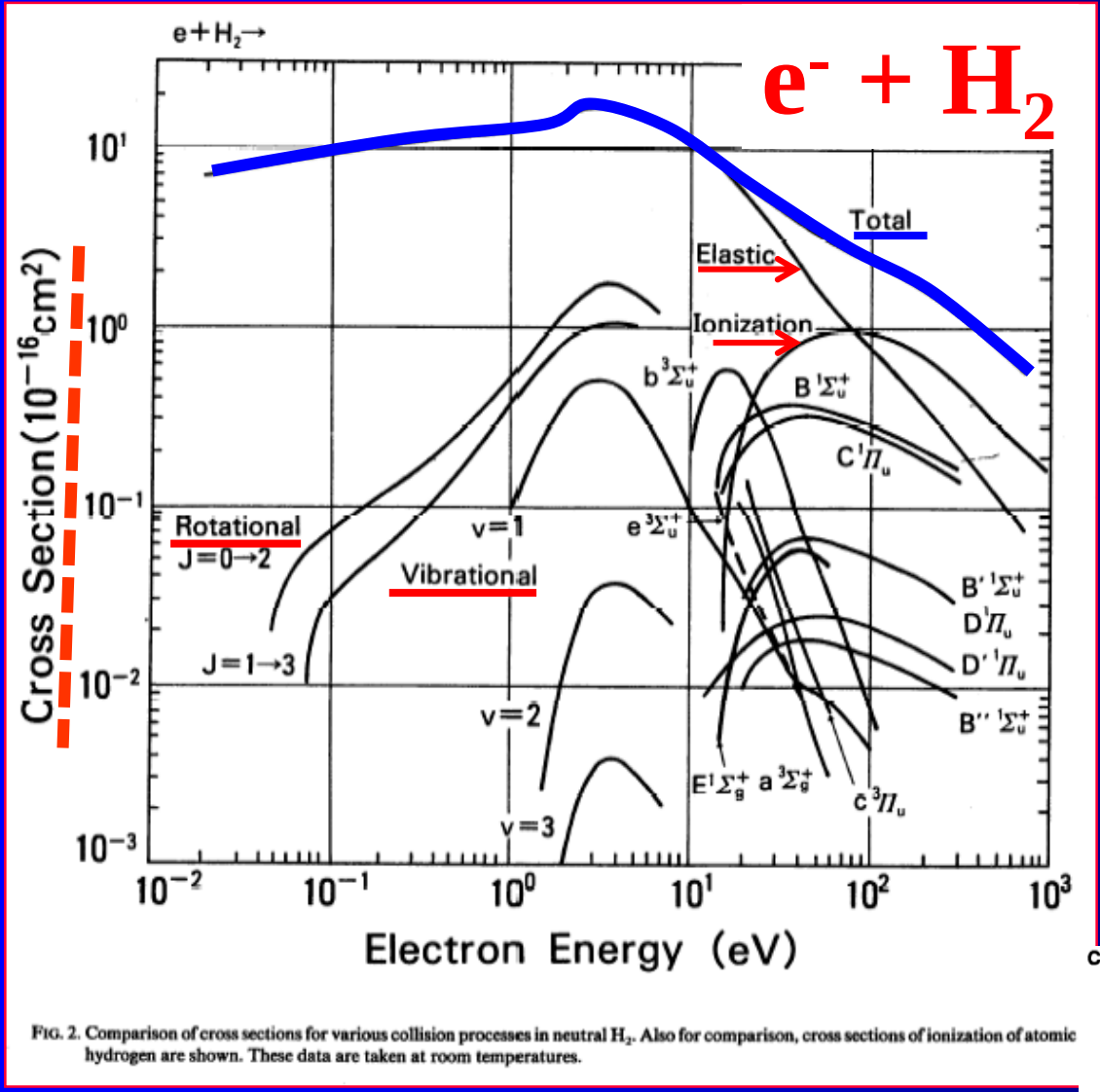

FIG. 2. Comparison of cross sections for various collision processes in neutral H_2. Also for comparison, cross sections of ionization of atomic hydrogen are shown. These data are taken at room temperatures.

(1990)

Cross Sections and Related Data for Electron Collisions with Hydrogen Molecules and Molecular Ions[a]

H. Tawara, Y. Itikawa,[b] H. Nishimura,[c] and M. Yoshino[d]

National Institute for Fusion Science,[c] *Nagoya 464-01, Japan*

(Received July 5, 1989; revised manuscript received November 1, 1989)

Data are compiled and evaluated for collision processes of excitation, dissociation, ionization, attachment, and recombination of hydrogen molecules and molecular ions (H_2^+, H_3^+) by electron impact as well as for properties of their collision products.

Key words: electron impact; hydrogen molecule; hydrogen molecular ion; scattering; elastic integral; vibrational excitation; rotational excitation; dissociation; ionization; photon emission; cross section.

J. Phys. Chem. Ref. Data, Vol. 19, No. 3, 1990

Electron scattering cross-section on Ar

e + H_2

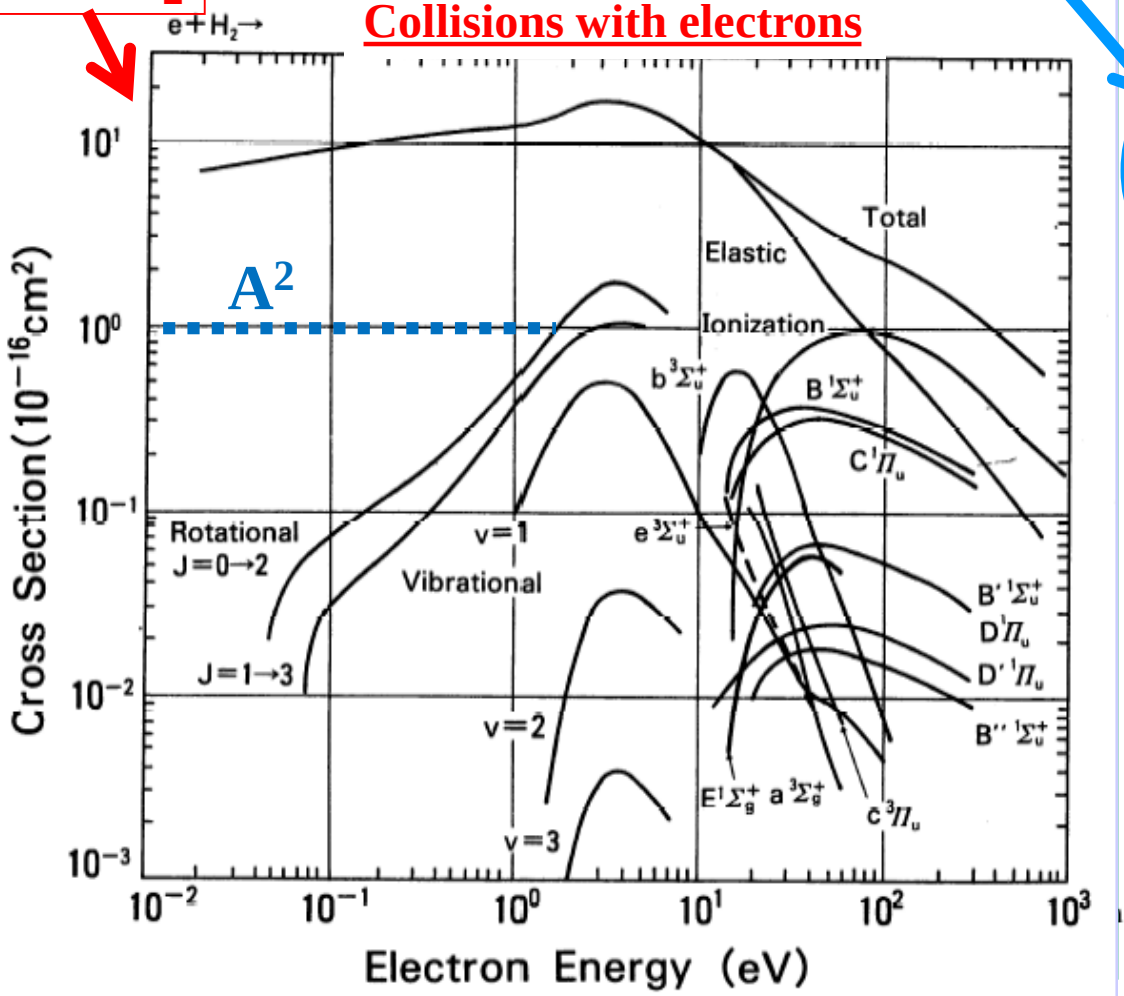

FIG. 2. Comparison of cross sections for various collision processes in neutral H_2. Also for comparison, cross sections of ionization of atomic hydrogen are shown. These data are taken at room temperatures.

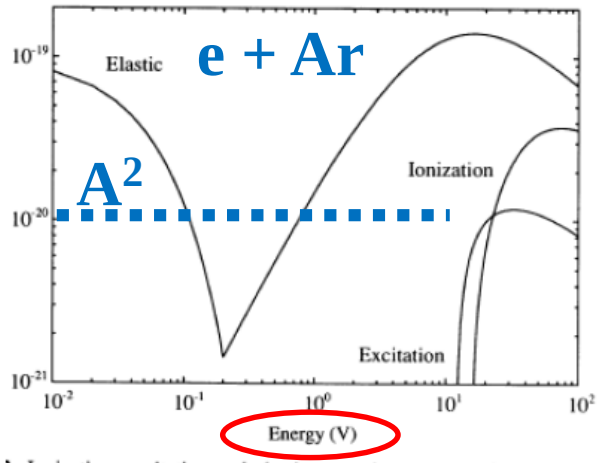

3. Ionization, excitation and elastic scattering cross sections for electrons in
piled by Vahedi, 1993).

gas

Lieberman&Lichtenberg

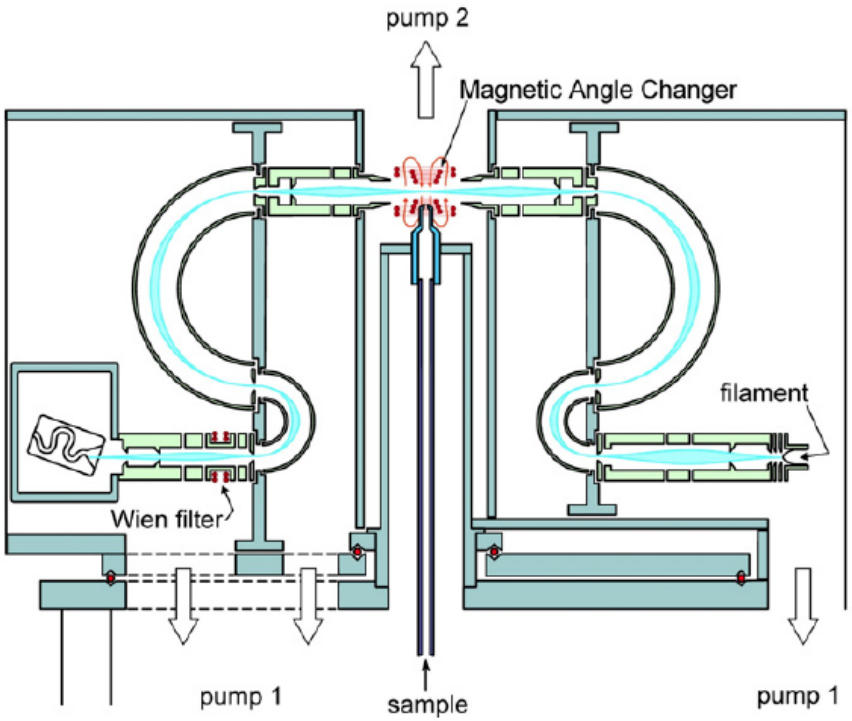

Fig. 3. The electron spectrometer of Allan (6).

Two Experimental Advances. The basic workhorse used in a large number of electron-scattering studies is the electron spectrometer. Free electrons are formed into a beam and energy selected by various combinations of electrostatic and magnetic fields. The use of electrostatic fields is most common, because they are more easily controlled and shielded than their magnetic counterparts. This is particularly important when it is essential to preserve the direction of low-energy electrons following the collision process.

Fig. 3 exhibits an example of such a spectrometer (6), which combines the characteristics of a conventional electrostatic device with an important innovation. It can be used for elastic scattering and electron impact excitation studies. The electron gun consists of a source of electrons produced by thermionic emission from a heated filament. The electrons are collimated and focused by an electrostatic lens system onto the input aperture of a double hemispherical energy selector. Those electrons within a narrow band of energies satisfying the criteria for transmission through the selector are then focused on the gas beam produced by a nozzle arrangement. Scattered electrons from the interaction region traveling in the direction of the scattered electron analyzer are similarly focused onto the input aperture of its double hemispherical analyzer, and the transmitted electrons are finally being focused into a single-channel electron multiplier detector.

One drawback of conventional electron spectrometers is that the angular range of the electron analyzer is limited by the physical presence of other components of the spectrometer. This limitation was overcome by Read and Channing (4) who applied a localized static magnetic field to the interaction region of a conventional spectrometer. The incident electron beam and the scattered electrons are, respectively, steered to and from the interaction region through angles set by the field (hence, the common name "magnetic angle changer" or "MAC"). This steering means that electrons normally scattered into inaccessible scattering angles are rotated into the accessible angular range of the electron analyzer while the magnetic field design is such that it leaves the angular distribution of the electrons undistorted. The spectrometer shown in Fig. 3 has a MAC fitted, thereby enabling the full angular range 0–180° to be accessed.

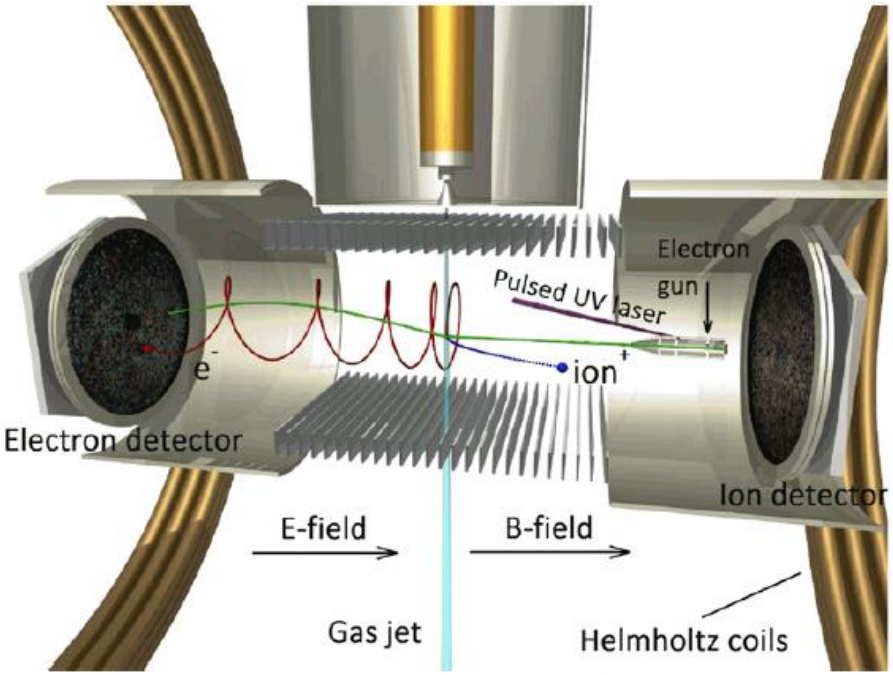

Fig. 4. The reaction microscope of Ren et al. (7). The projectile-electron beam is crossed with a supersonic gas beam. The projectile is created by a pulsed UV laser illuminating a photocathode. The outgoing electrons and ions are extracted by a homogeneous electric (E) field, created by a series of parallel electrodes, and detected by 2D position- and time-sensitive multihit detectors. A pair of Helmholtz coils generates a uniform magnetic (B) field, which forces the electrons into cyclotron trajectories and guides them onto the detector. The time of flight for each particle from the collision region to the respective detector is determined by the clock signals from the projectile pulse and the detectors.

A recent version, developed by Ren et al. (7) to study single ionization processes is shown in Fig. 4. The RM operates on entirely different principles from conventional electron spectrometers. Briefly, a pulsed beam of electrons crosses a supersonic atom beam. The ejected electrons and the recoiling ions are extracted in opposite directions by a weak uniform electric field parallel to the incident electron beam direction. A uniform magnetic field is also applied in this direction to confine electrons emitted perpendicular to the electric field. After passing through field-free drift regions, the slow ejected electrons are detected in two time- and position-sensitive multihit detectors, allowing for the vector momenta of all particles to be calculated. Unlike most conventional coincidence electron spectrometers, which only enable measurements in a single plane at any one time, this technique allows for data to be collected over a large part of the entire 4π solid angle simultaneously.

Without going into detail, we emphasize the difficulty of obtaining absolute cross sections. Most of the time, some cross-normalization to "known" (or believed to be known) other data, such as cross sections for another target in a mixed-flow setup, data for angle-integrated state-to-state transitions after performing angle-differential measurements, total (summed over all accessible exit channels) cross sections, or even theoretical predictions, is required. Only in exceptional cases, absolute total ionization or recombination cross sections can be obtained directly (after carefully determining many experimental parameters) and fed into plasma models. An example is the crossed-beam apparatus developed by Müller and collaborators (8, 9).

$$H_2^+ + Ar \Rightarrow ArH^+ + H$$

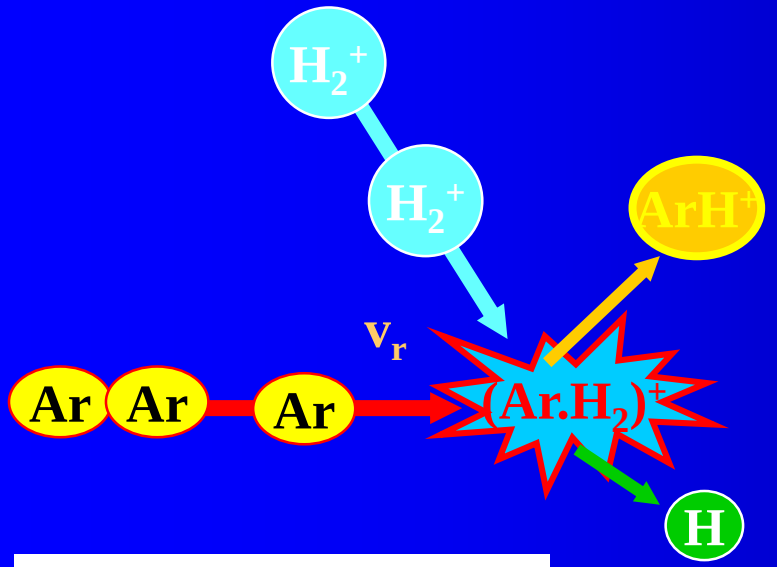

reaction cross section

$$A^+ + B \rightarrow C^+ + D$$

$$\frac{dA^+}{dt} = -k_{BIN} A^+ B$$

$$[A^+]_t = [A^+]_{t=0} \cdot e^{-k[B]t}$$

$$\nu_{coll} = -nV_{rel} = -n\nu S = -n\nu\pi\delta^2 = -n\nu\sigma$$

$$\frac{dI}{dt} = -\frac{I}{\tau_{coll}} = -I\nu_{coll}$$

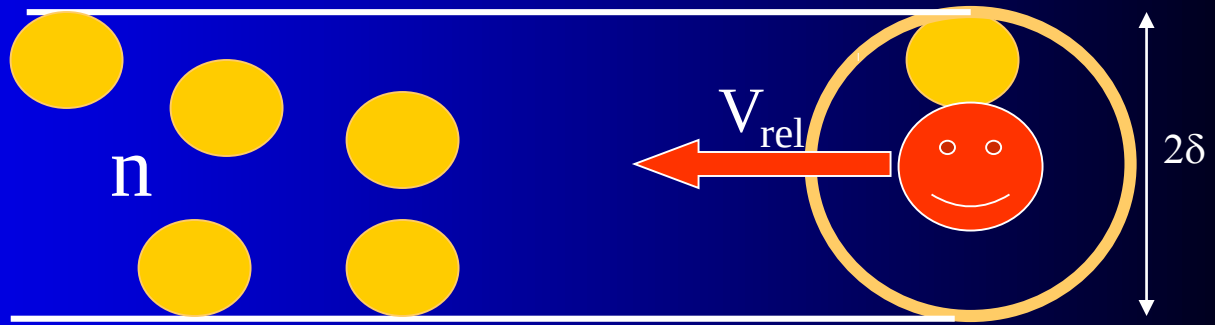

$$I(t) = I_0 \exp(-\nu_{coll} t) = I_0 \exp(-\sigma n \nu_{rel} t) \Leftrightarrow$$

$$\mathbf{I = I_0 \exp(-\sigma n_{Ar} x)}$$

Kinetics of elementary process

$$H_2^+ + Ar \Rightarrow ArH^+ + H$$

$$A^+ + B \rightarrow C^+ + D$$

$$\frac{dA^+}{dt} = -k_{BIN} A^+ B$$

$$[A^+]_t = [A^+]_{t=0} \cdot e^{-k[B]t}$$

Multiple collision

@ T

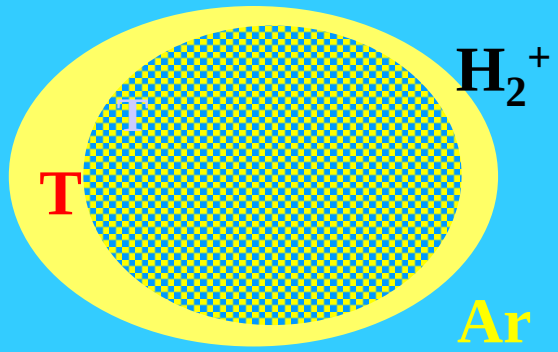

reaction rate coefficient

$d(n_{H2^+})/dt = -k\, n_{H2^+}.\, n_{Ar}$

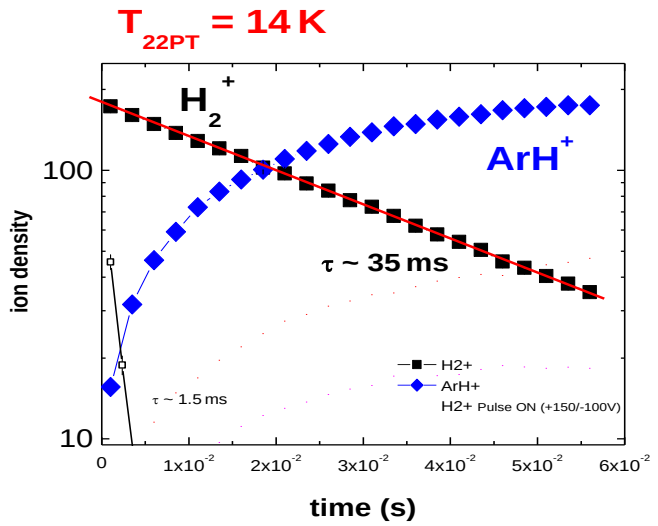

$n_{H2^+}. = (n_{H2^+})._0 \exp(-k n_{Ar} t)$

k(T)

reactions

$$A^+ + B \rightarrow C^+ + D$$

$$\frac{dA^+}{dt} = -k_{BIN} A^+ B$$

$$[k_{BIN}] = cm^3 s^{-1}$$

$1/\tau = k_{BIN}[B] = \ldots n v\rho \ldots = [B] v\rho \ldots . [B] \langle v\rho \rangle$

$$k_{BIN} = \langle v\rho \rangle$$

Kinetics of elementary process

$$H_2^+ + Ar \Rightarrow ArH^+ + H$$

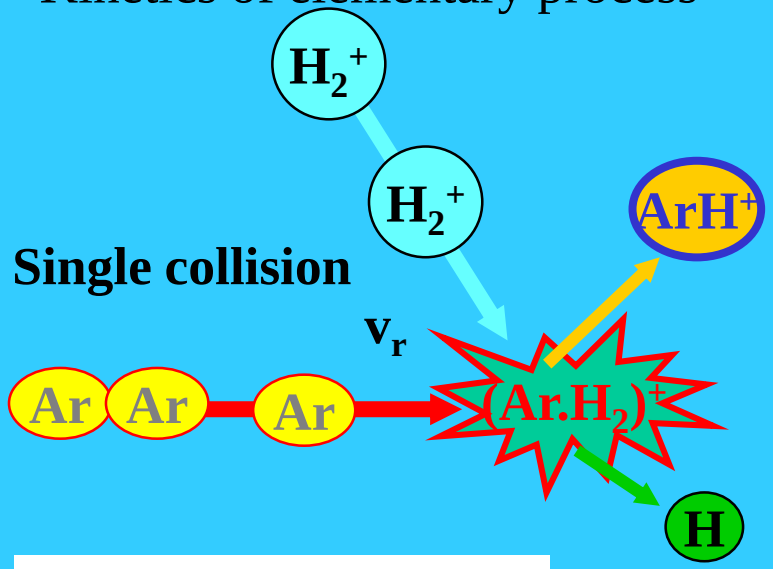

reaction cross section

$$I = I_0 \exp(-\sigma n_{Ar} x)$$

Multiple collision

@ T

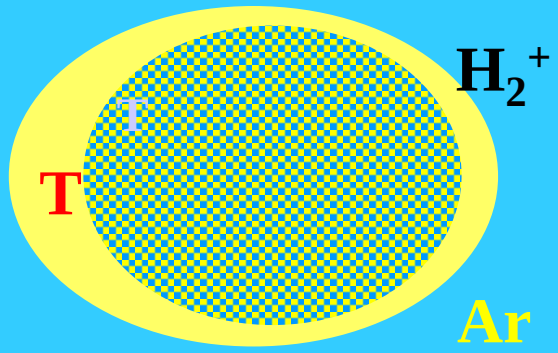

reaction rate coefficient

$$d(n_{H2^+})/dt = -k\, n_{H2^+}.\, n_{Ar}$$

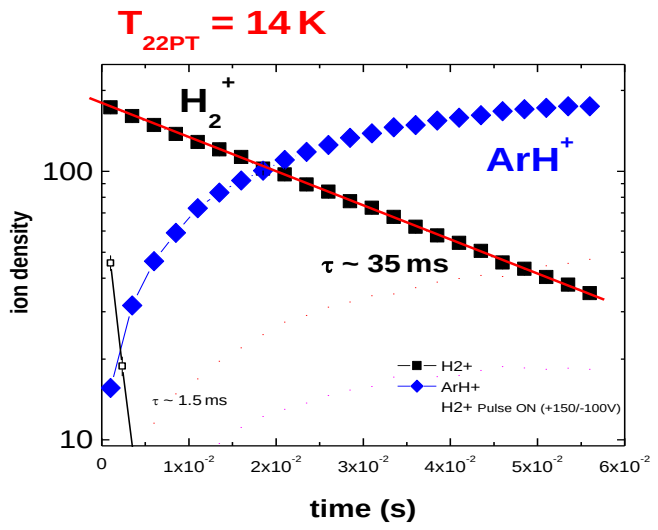

$$n_{H2^+}. = (n_{H2^+}).{}_0 \exp(-k n_{Ar} t)$$

$\sigma(v_r)$

$k(T) = \langle v\sigma \rangle$

$k(T)$

$$A^+ + B \rightarrow C^+ + D$$

$\sigma(v_r)$

$$k_{BIN} = k_{BIN}(T)$$

$$\mathbf{k(T)=<v_r\sigma(v_r)>}$$

$$k = \int_v f_T(v).v.\sigma(v)dv = k(T)$$

Ar

Electron scattering cross-section on Ar

$$k = \int_v f_T(v).v.\sigma(v)dv = k(T)$$

Electrons – Boltzman distribution with T_e

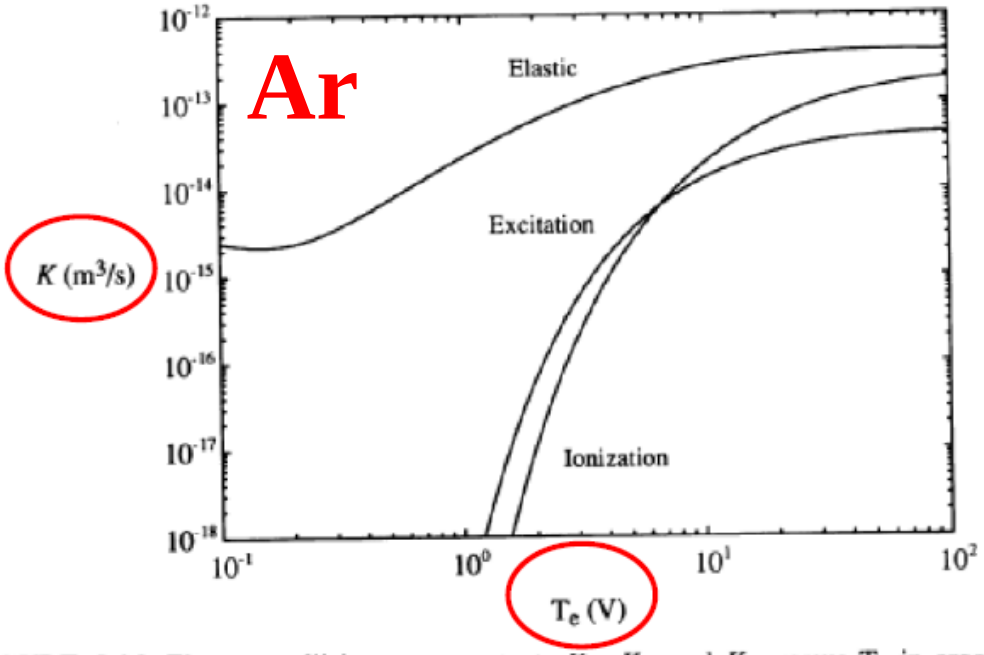

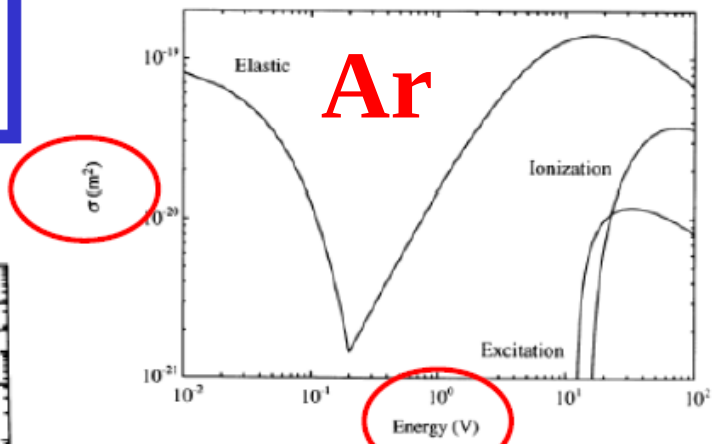

3. Ionization, excitation and elastic scattering cross sections for electrons in
mpiled by Vahedi, 1993).

$$\alpha(T, T_e) \propto \int_0^\infty \sqrt{E}\,\sigma_w(E,T) f(E,T_e) dE$$

FIGURE 3.16. Electron collision rate constants K_{iz}, K_{ex} and K_m versus T_e in argon gas (compiled by Vahedi, 1993).

What if we have metastables?

Lieberman&Lichtenberg

Reaction coordinate

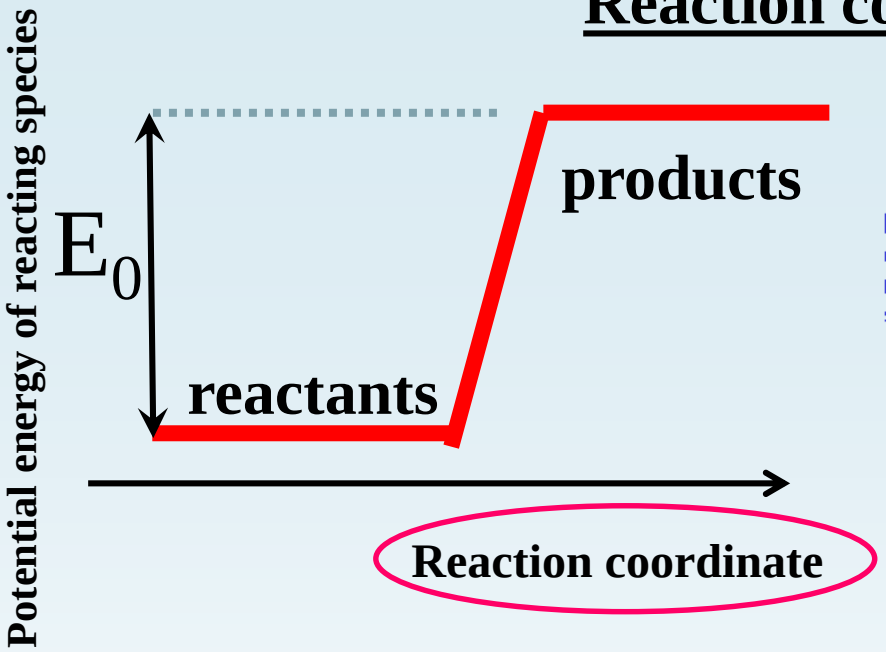

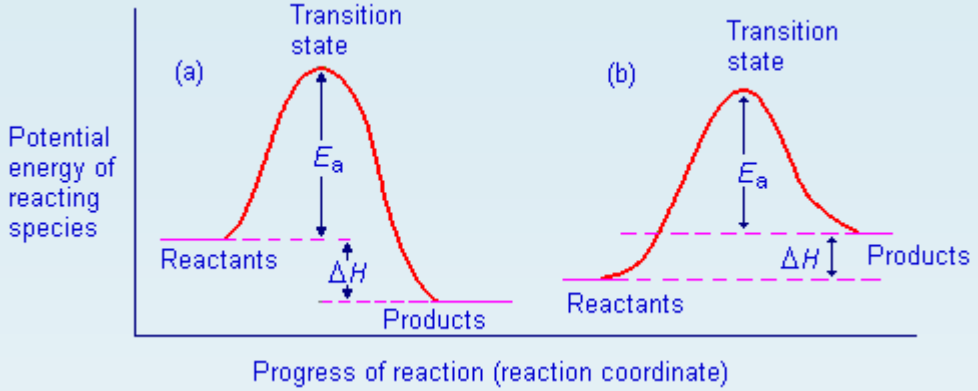

Collisional energy

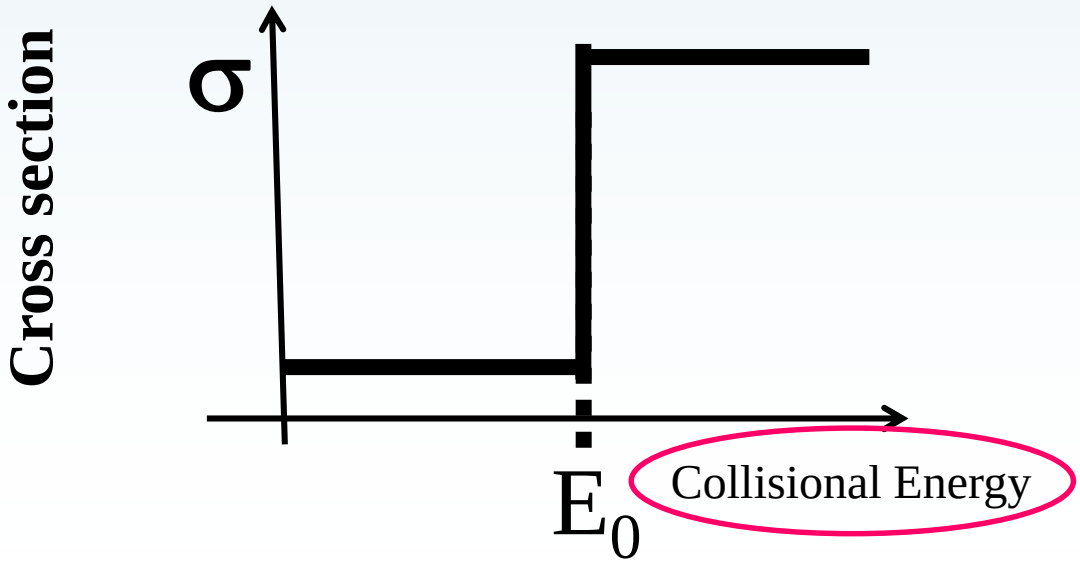

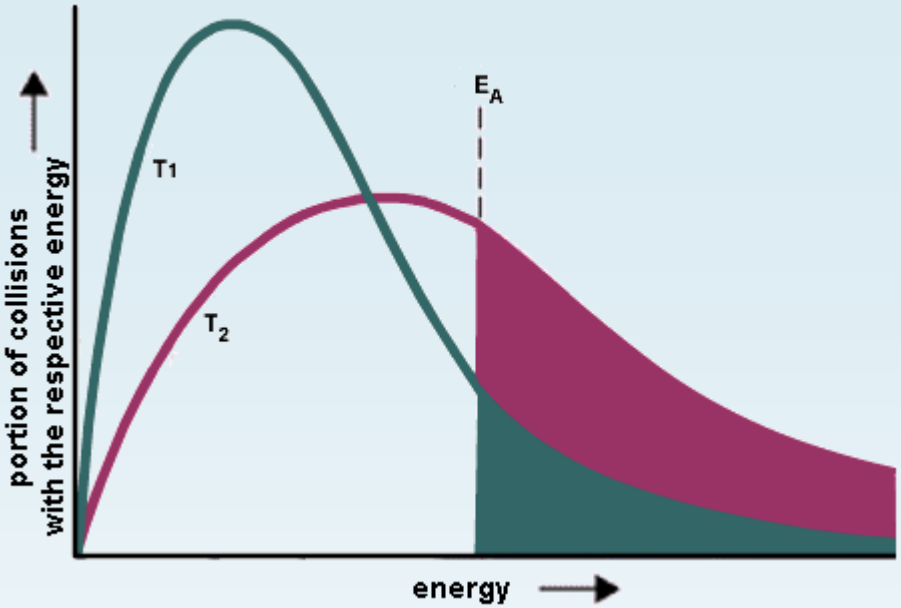
portion of collisions
with the respective energy
T1
T2
EA
energy

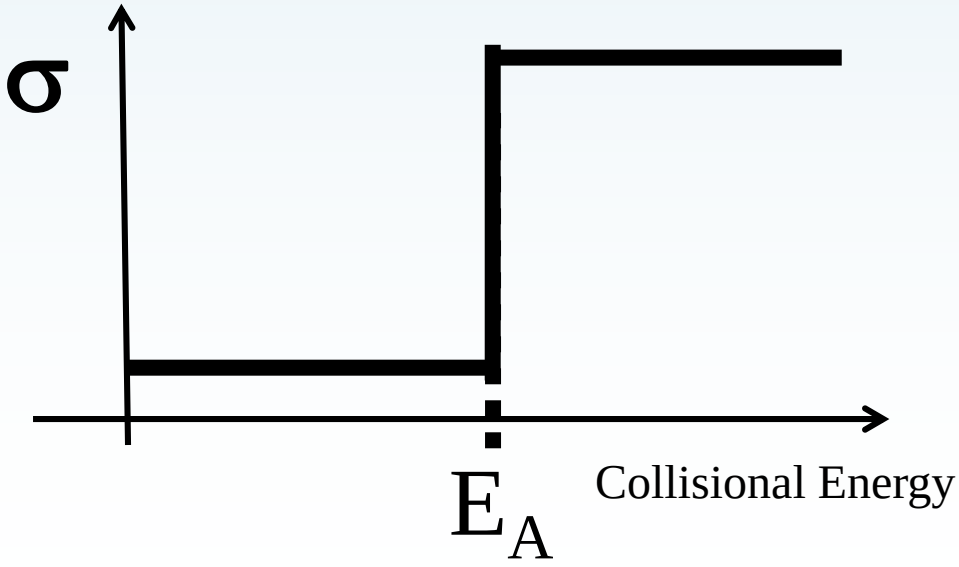
σ
EA
Collisional Energy

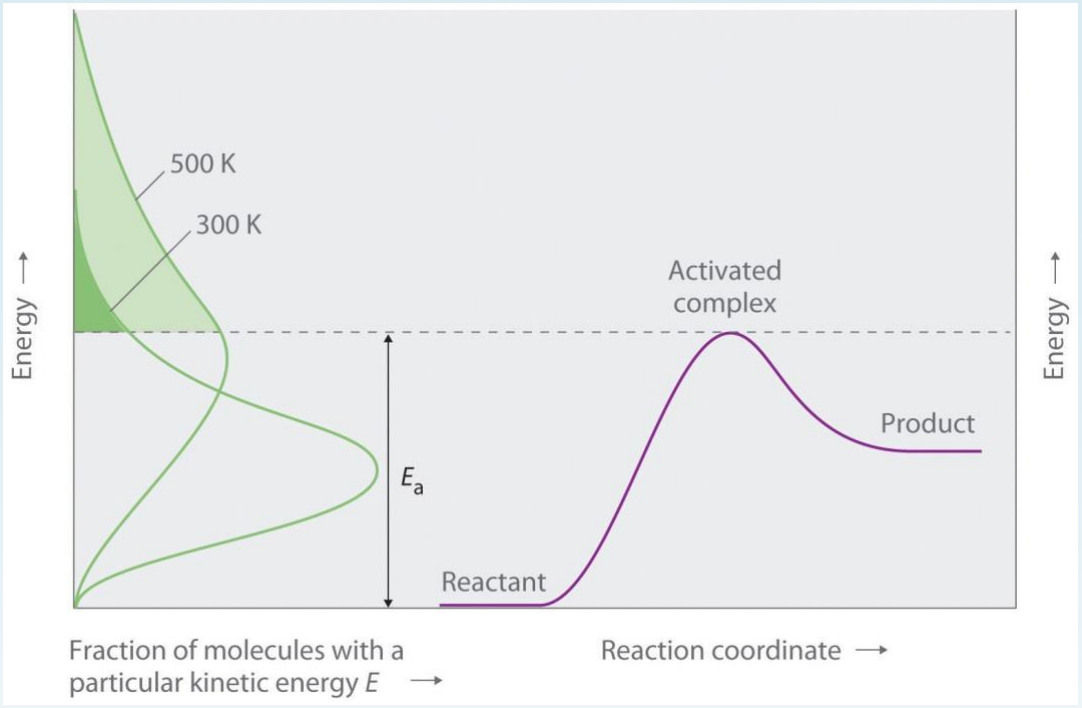

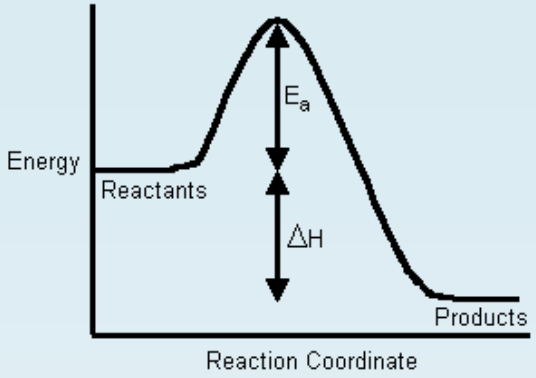

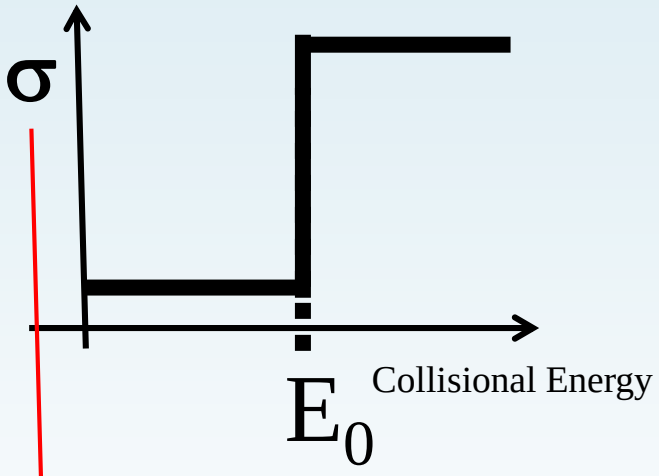

The thermal average rate constant

The thermal average reaction rate constant

The reaction rate coefficient

The thermally averaged rate constant $\alpha_{th}(T)$ (in a.u.) is obtained from the energy-dependent cross-section $\sigma(E)$ as

$$\alpha_{th}(T) = \frac{8\pi}{(2\pi kT)^{3/2}} \int_0^\infty \sigma(E_{el}) e^{-\frac{E_{el}}{kT}} E_{el} dE_{el}, \quad (4)$$

where T is the temperature. Temperature dependencies $\alpha_{th}(T)$ for different rovibrational transitions $v \rightarrow v'$ obtained using equation (4) are shown in Fig. 3 as solid lines.

It is written for process with electron energy e.g. exciatation by collisions with electrons

Higher temperatures favor products for an endothermic reaction

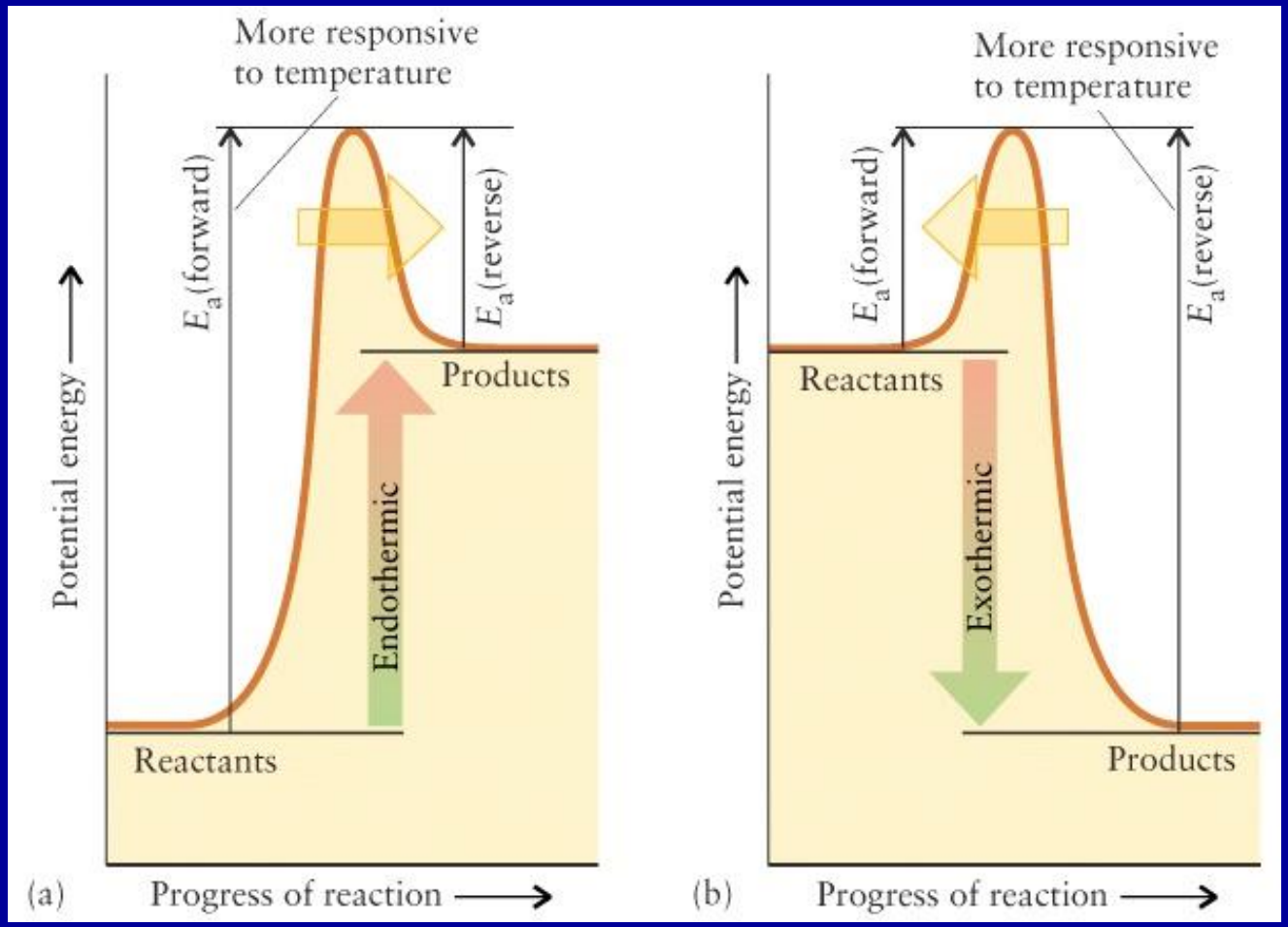

Endothermic reaction: E_a(forward) > E_a(reverse)

Exothermic reaction: E_a(forward) < E_a(reverse)

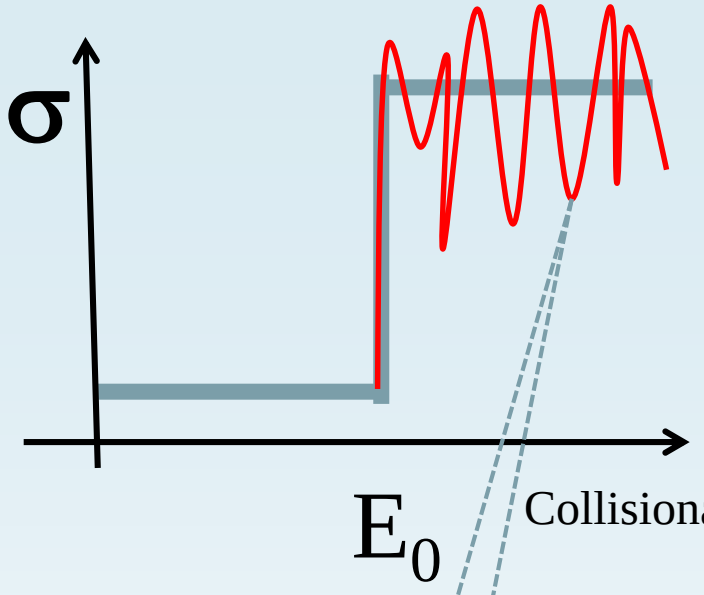

Electron impact rotational excitation of CH⁺

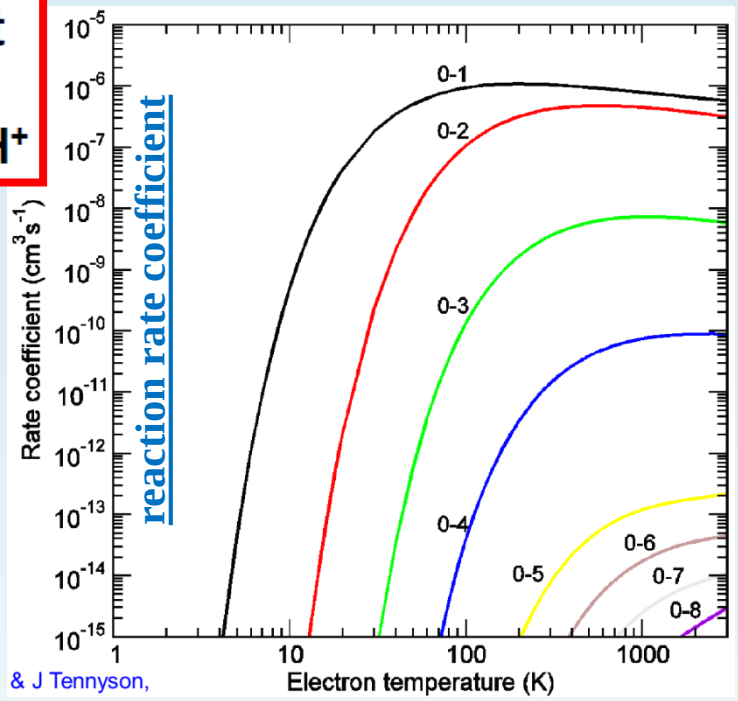

The thermally averaged rate constant $\alpha_{th}(T)$ (in a.u.) is obtained from the energy-dependent cross-section $\sigma(E)$ as

$$\alpha_{th}(T) = \frac{8\pi}{(2\pi kT)^{3/2}} \int_0^\infty \sigma(E_{el}) e^{-\frac{E_{el}}{kT}} E_{el} dE_{el}\,, \qquad (4)$$

where T is the temperature. Temperature dependencies $\alpha_{th}(T)$ for different rovibrational transitions $v \rightarrow v'$ obtained using equation (4) are shown in Fig. 3 as solid lines.

For further discussion, it is convenient to represent the cross-section $\sigma(E_{el})$ in the form

$$\sigma(E_{el}) = \frac{\pi}{k^2} P(E_{el})\,, \qquad (5)$$

where k is the wave vector of the incident electron, $P(E_{el})$ is the probability for vibrational (de-)excitation at collision energy E_{el}.

Arrhenius dependence

$$k = A\, e^{-\frac{E_a}{RT}}$$

activation energy

pre-exponential factor

average kinetic energy

$$\ln k = \ln A - \frac{E_a}{RT}$$

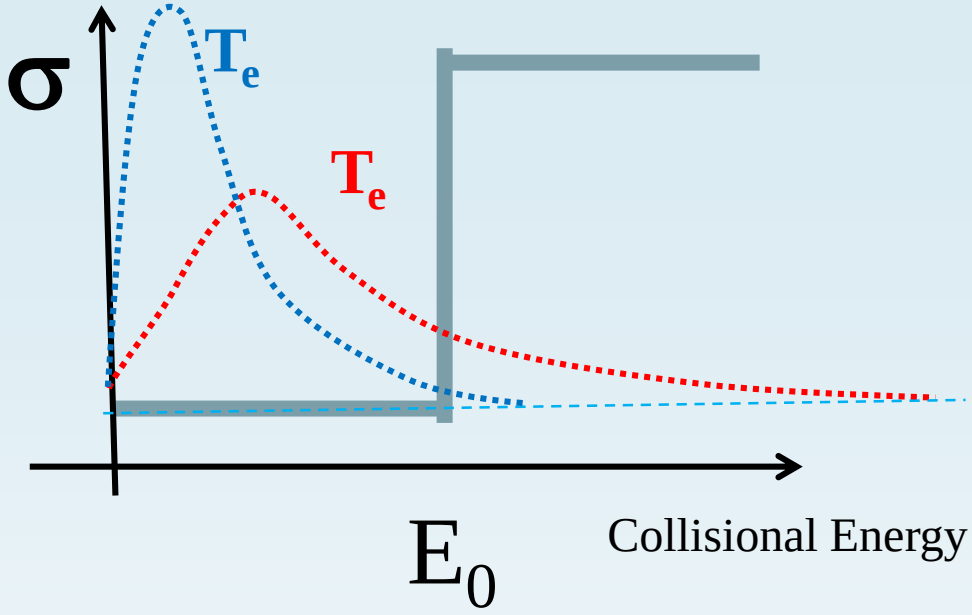

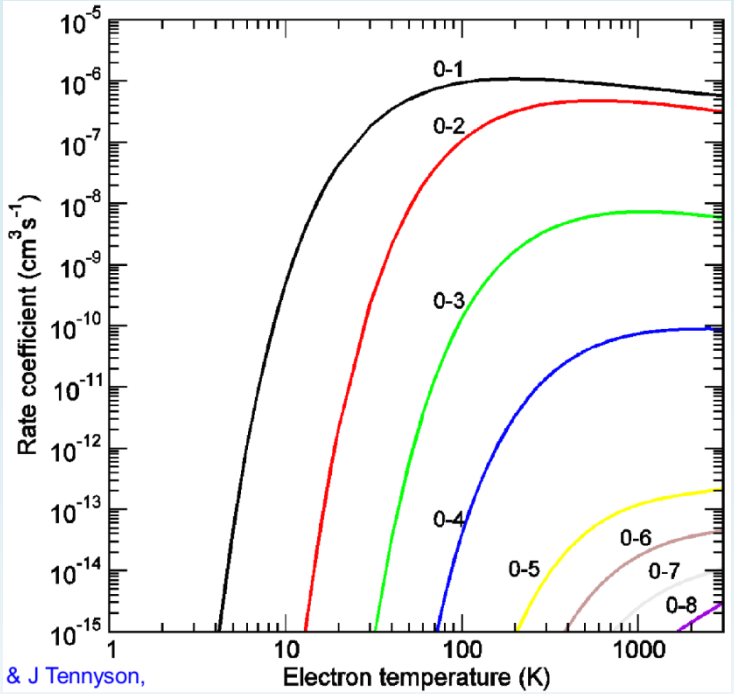

Arrhenius plot

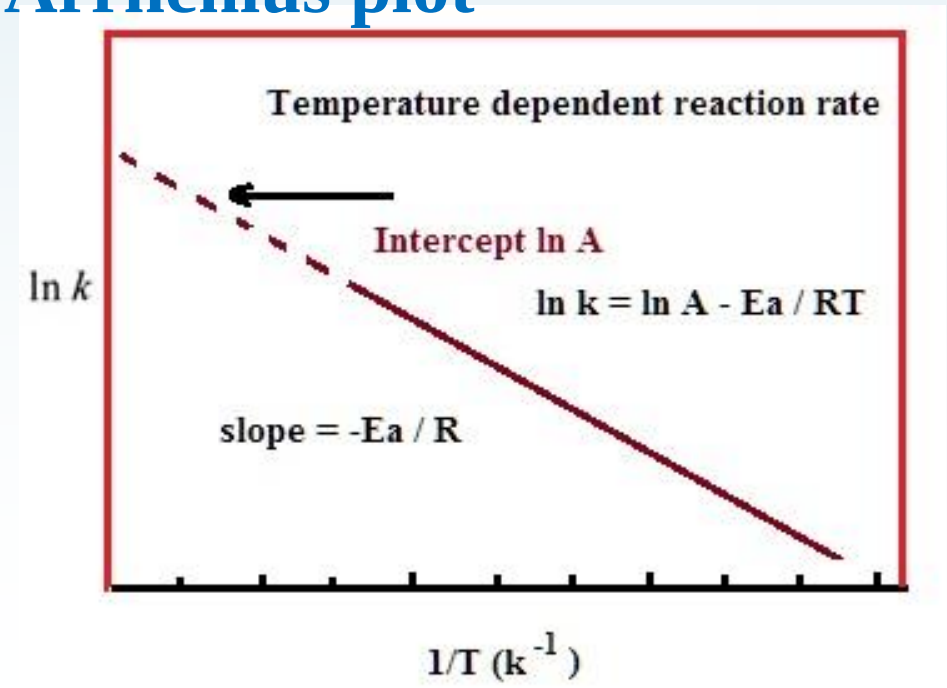

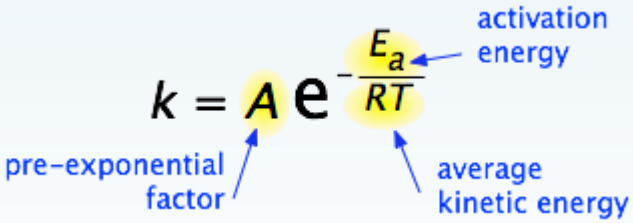

$$\ln k = \ln A - \frac{E_a}{RT}$$

Some experiments and data….

Collision cross section of IMR

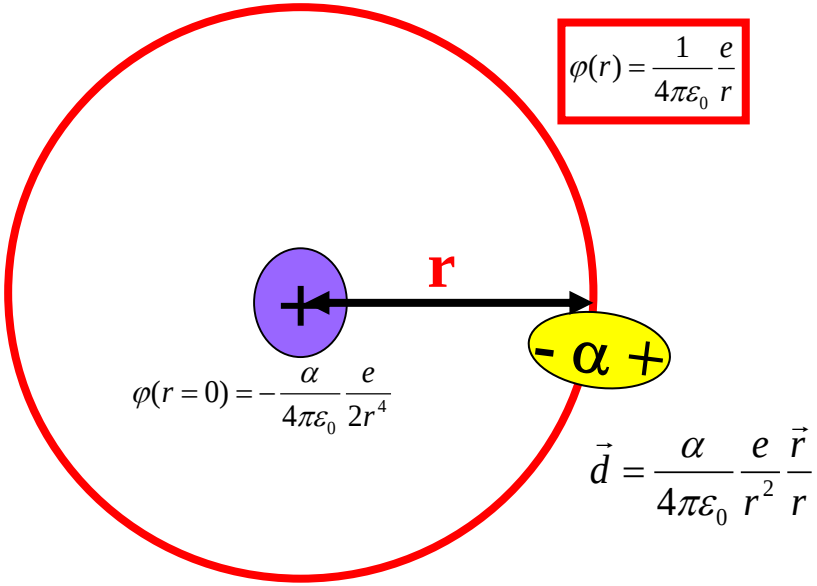

$$\varphi(r) = \frac{1}{4\pi\varepsilon_0}\frac{e}{r}$$

$$\varphi(r=0) = -\frac{\alpha}{4\pi\varepsilon_0}\frac{e}{2r^4}$$

$$\vec{d} = \frac{\alpha}{4\pi\varepsilon_0}\frac{e}{r^2}\frac{\vec{r}}{r}$$

α - polarizability

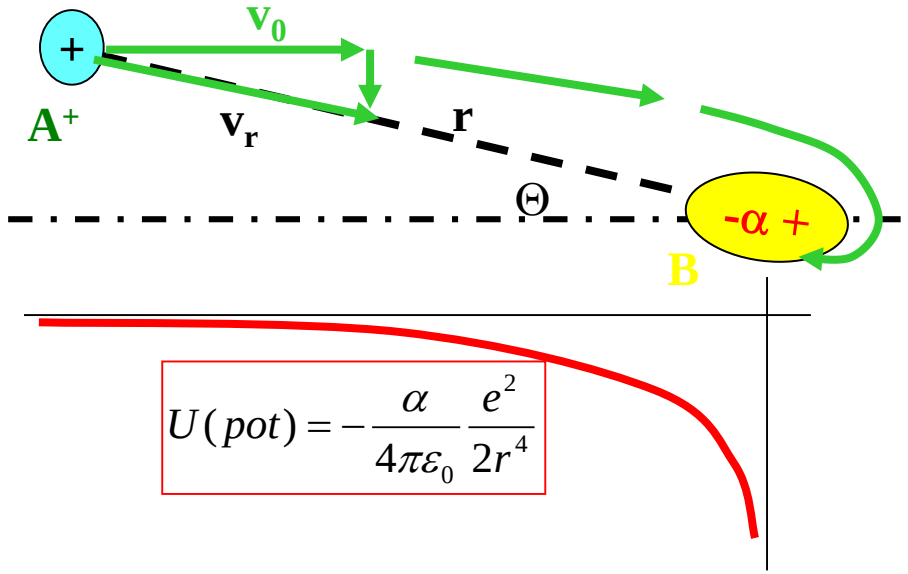

$$U(pot) = -\frac{\alpha}{4\pi\varepsilon_0}\frac{e^2}{2r^4}$$

$$\frac{\mu v_0^2}{2} = \frac{\alpha}{4\pi\varepsilon_0}\frac{e^2}{2r^4}$$

Collision cross section of IMR

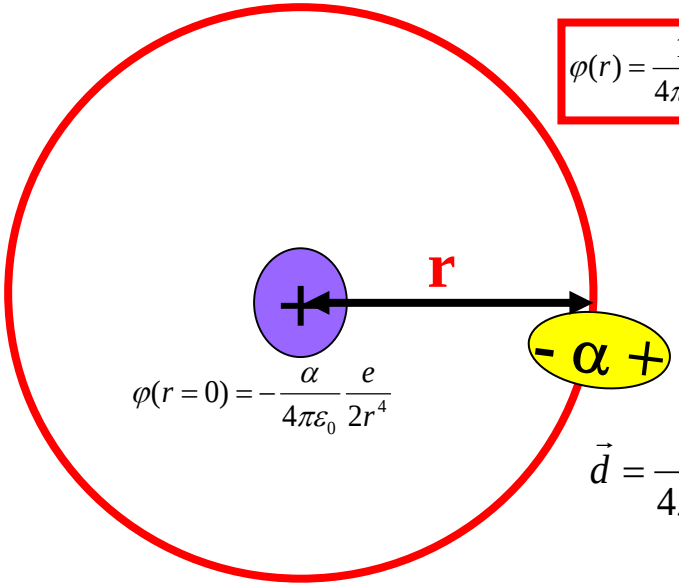

$$\varphi(r) = \frac{1}{4\pi\varepsilon_0}\frac{e}{r}$$

$$\varphi(r=0) = -\frac{\alpha}{4\pi\varepsilon_0}\frac{e}{2r^4}$$

$$\vec{d} = \frac{\alpha}{4\pi\varepsilon_0}\frac{e}{r^2}\frac{\vec{r}}{r}$$

α - polarizability

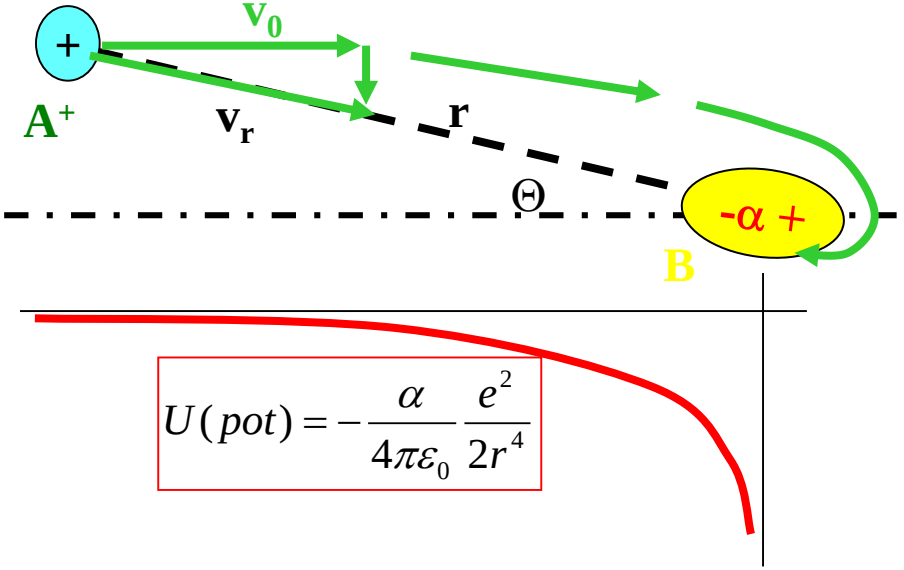

$$U(pot) = -\frac{\alpha}{4\pi\varepsilon_0}\frac{e^2}{2r^4}$$

$$\frac{\mu v_0^2}{2} = \frac{\alpha}{4\pi\varepsilon_0}\frac{e^2}{2r^4}$$

$$\sigma = \pi\rho_0^2 = \frac{2\pi e}{v_0(4\pi\varepsilon_0)}\sqrt{\frac{\alpha}{\mu}}$$

$$\sigma = \pi\rho_0^2 \sim \frac{1}{v_0}\sqrt{\frac{\alpha}{\mu}} \sim \frac{1}{\sqrt{E}}$$

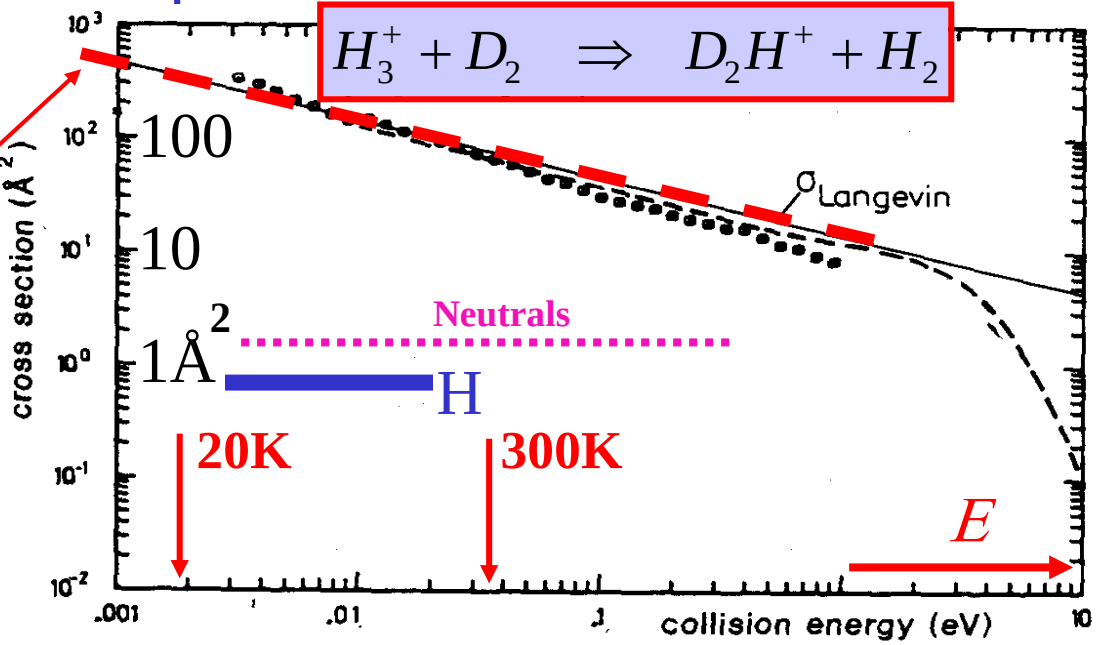

N3+

Actual experiments and theory

2020

$$H_2^+ + H_2 \rightarrow H_3^+ + H$$

ChemPhysChem
Articles
doi.org/10.1002/cphc.202000258

VIP *Very Important Paper*

Formation of H_3^+ in Collisions of H_2^+ with H_2 Studied in a Guided Ion Beam Instrument

Igor Savić,*[a] Stephan Schlemmer,[b] and Dieter Gerlich[c]

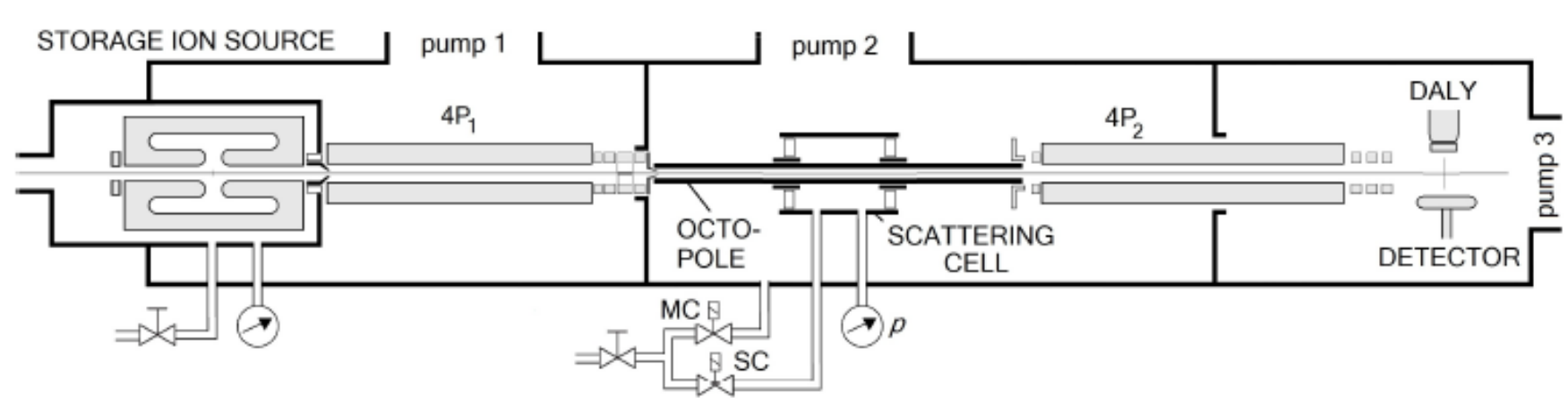

Figure 1. The Guided Ion Beam instrument *NOVion* consists of a storage ion source (SIS), a first quadrupole ($4P_1$), an octopole, guiding the ions through a scattering cell, a second quadrupole ($4P_2$), and a Daly type ion detector. Three separated vacuum chambers are pumped by turbopumps with pumping speeds of 180 l/s for hydrogen. For determining integral cross sections of ions reacting with neutrals, the target gas is leaked alternately into the scattering cell (SC) or into the main chamber (MC) containing the octopole. The net pressure p is the difference between the two values measured under these two conditions, p^{MC} and p^{SC}.

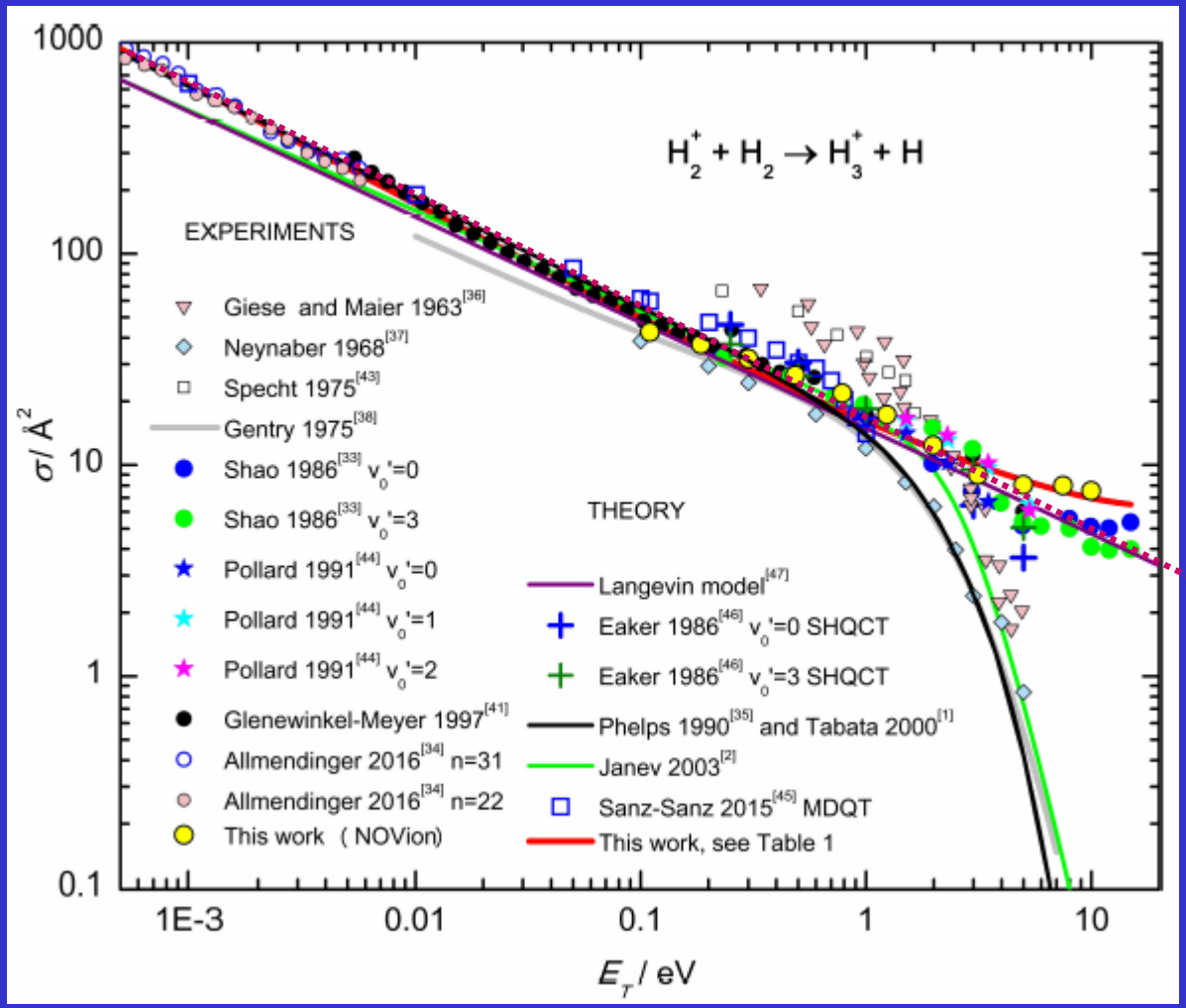

2020

$$H_2^+ + H_2 \rightarrow H_3^+ + H$$

$\sigma_L(E_T)$

$$\sigma = \pi\rho_0^2 \sim \frac{1}{v_0}\sqrt{\frac{\alpha}{\mu}} \sim \frac{1}{\sqrt{E}}$$

Langevin

Figure 2. Dependence of the integral cross section for the reaction $H_2^+ + H_2 \rightarrow H_3^+ + H$ on the collision energy E_T. In the meV and sub-meV energy range, there is good agreement between two different merged beam results, Refs. [34,41]. Note that Allmendinger et al.[34] scaled their relative cross sections to the absolute ones calculated by Sanz-Sanz et al.[45] as described in the caption of figure 10 of Ref. [34]. Between thermal energies and 1 eV, most of the published and tabulated values agree more or less with the function proposed in the compilations by Tabata[1] (black line) and Janev et al.[2] (green line). However, based on results from the sixties and seventies, a steep decline has been predicted above 2 eV. In contrary, our results (yellow filled circles) do not show this trend, in accordance with the guided ion beam results from Shao et al.[33] The data presented in Ref. [35] as tabulated values and in Ref. [1] as an analytical function are nearly identical and are represented here simply by the one black line.

Very recent experiments and theory

$H_2(1=0,1) + H_2^+ \rightarrow$

THE JOURNAL OF CHEMICAL PHYSICS **145**, 244316 (2016)

Observation of enhanced rate coefficients in the $H_2^+ + H_2 \rightarrow H_3^+ + H$ reaction at low collision energies

Pitt Allmendinger,[a] Johannes Deiglmayr,[a] Katharina Höveler, Otto Schullian, and Frédéric Merkt[b]
Laboratory of Physical Chemistry, ETH Zurich, Zurich, Switzerland

(Received 25 October 2016; accepted 29 November 2016; published online 29 December 2016)

2016

k/k_L

$$H_2^* + H_2 \rightarrow H_3^+ + H + e^- \quad (3)$$

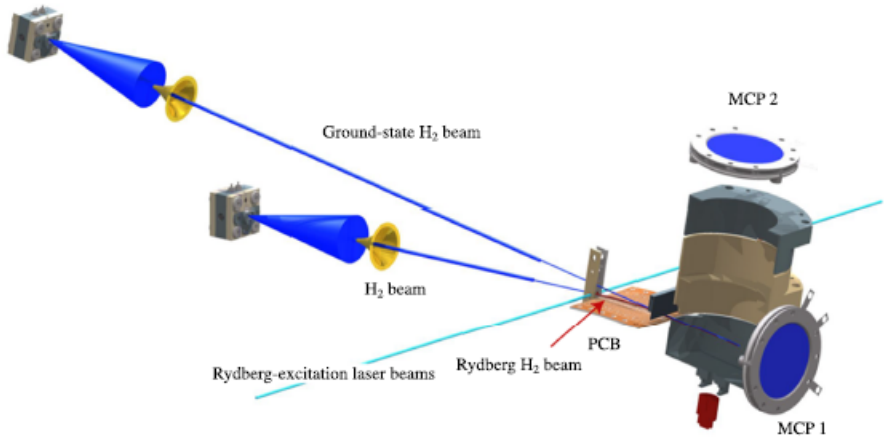

FIG. 1. Schematic representation of the merged-beam apparatus used to study ion-molecule reactions at low collision energies, with the two skimmed supersonic beams initially propagating at an angle of 10°, the Rydberg-Stark deflector made of a curved printed circuit board (PCB), and used to merge the beams after laser excitation, the reaction zone located within an electrode stack (gray), which constitutes the linear time-of-flight mass spectrometer used to detect reactants and products separately. (MCP1) and (MCP2) Microchannel-plate detectors to monitor the flight times of Rydberg H_2 molecules and the ion-time-of-flight spectra, respectively.

k/k_L=1

T[K]

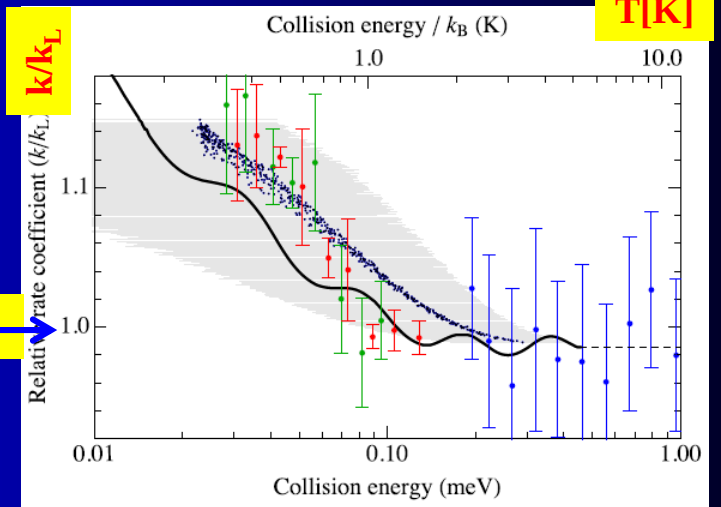

FIG. 3. Comparison of the energy-dependence of the measured relative rate coefficients $k(E)/k_L$ (color dots) to the calculation by Dashevskaya *et al.*[22] for normal H_2 (75% H_2 in $j = 1$ and 25% H_2 in $j = 0$) at fixed collision energies (solid line) and for collision energies averaged over the simulated experimental energy distributions (black dots, gray bars indicate one standard deviation). Green dots: two-pulse sequence ($\Delta t = 7\,\mu$s) and H_2^* Rydberg beam central velocity $v(H_2^*) = 1800$ m/s. Red dots: single-pulse sequence for $v(H_2^*) = 1700$ m/s. Blue dots: single-pulse sequence, $v(H_2^*) = 1540$ m/s. The absolute scaling of each experimental data set was chosen to minimize the deviation from the simulation. The simulation (black dots) is based on the experimental parameters of the two-pulse measurement (green dots), but the result is very similar for the other measurements.

$H_2(1=0,1) + H_2^+ \rightarrow$

k/k_L

THE JOURNAL OF CHEMICAL PHYSICS 145, 244315 (2016)

2016

Relocking of intrinsic angular momenta in collisions of diatoms with ions: Capture of $H_2(j = 0,1)$ by H_2^+

E. I. Dashevskaya,[1,2] I. Litvin,[3] E. E. Nikitin,[1,2] and J. Troe[2,3,a)]
[1]Schulich Faculty of Chemistry, Technion—Israel Institute of Technology, Haifa 32000, Israel
[2]Max-Planck-Institut für Biophysikalische Chemie, Am Fassberg 11, D-37077 Göttingen, Germany
[3]Institut für Physikalische Chemie, Universität Göttingen, Tammannstrasse 6, D-37077 Göttingen, Germany

(Received 25 October 2016; accepted 30 November 2016; published online 29 December 2016)

k/k_L

T[K]

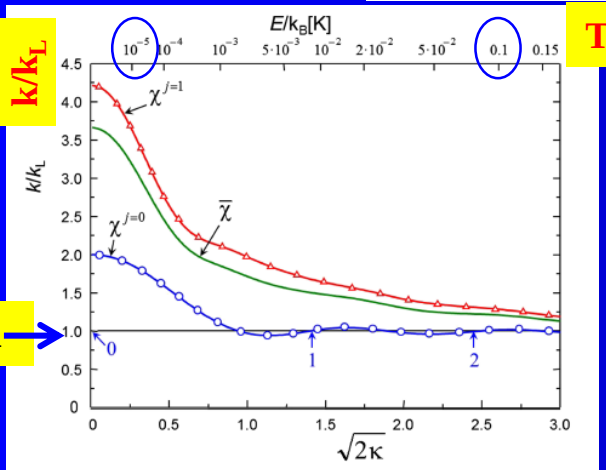

$k/k_L=1$

FIG. 2. Scaled rate coefficients for capture of $H_2(j=0,1)$ by H_2^+ ($\chi^{j=0}, \chi^{j=1}$) and mean rate coefficients for a para-ortho mixture $\bar{\chi} = (1/4)\chi^{j=0} + (3/4)\chi^{j=1}$ (values are given relative to the Langevin limit k_L; the classical opening of successive channels for a charge-induced dipole potential for $j = 0$ is marked by arrows (accurate results from the present work; ANC results are presented in Figs. 4 and 5 in the Appendix).

k/k_L

T[K]

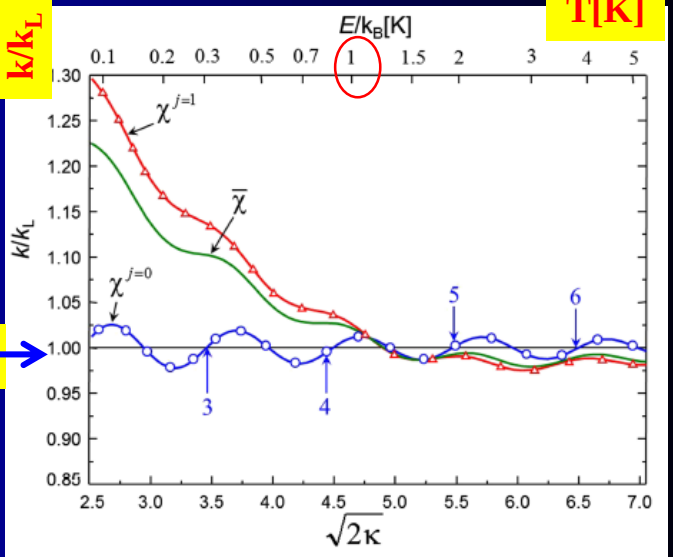

$k/k_L=1$

FIG. 3. As Fig. 2, but for larger energies.

k/k_L

T[K]

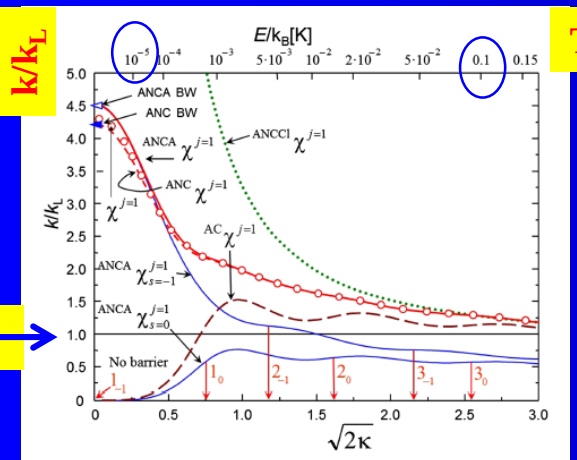

$k/k_L=1$

FIG. 4. Total and partial scaled rate coefficients for capture of $H_2(j = 1)$ by H_2^+ in different approximations across the ultra-low (two classically open channels) and very-low (several classically open channels) energy range. (The classical opening of successive channels for ANC potentials is marked by J_s symbols and arrows. BW = Bethe-Wigner limits.)

k/k_L

T[K]

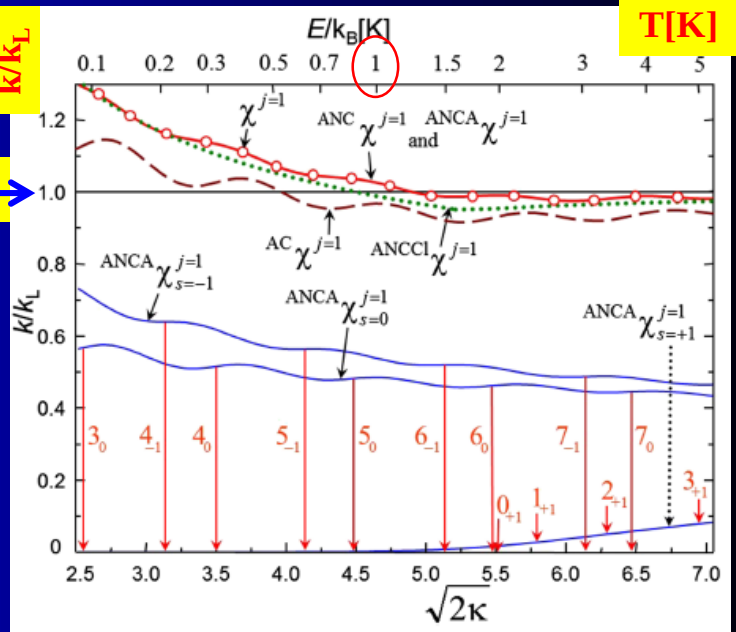

$k/k_L=1$

FIG. 5. As Fig. 4, but for larger energies.

$$H_2^+ + H_2 \rightarrow H_3^+ + H$$

10 K | 100 K | 1000 K

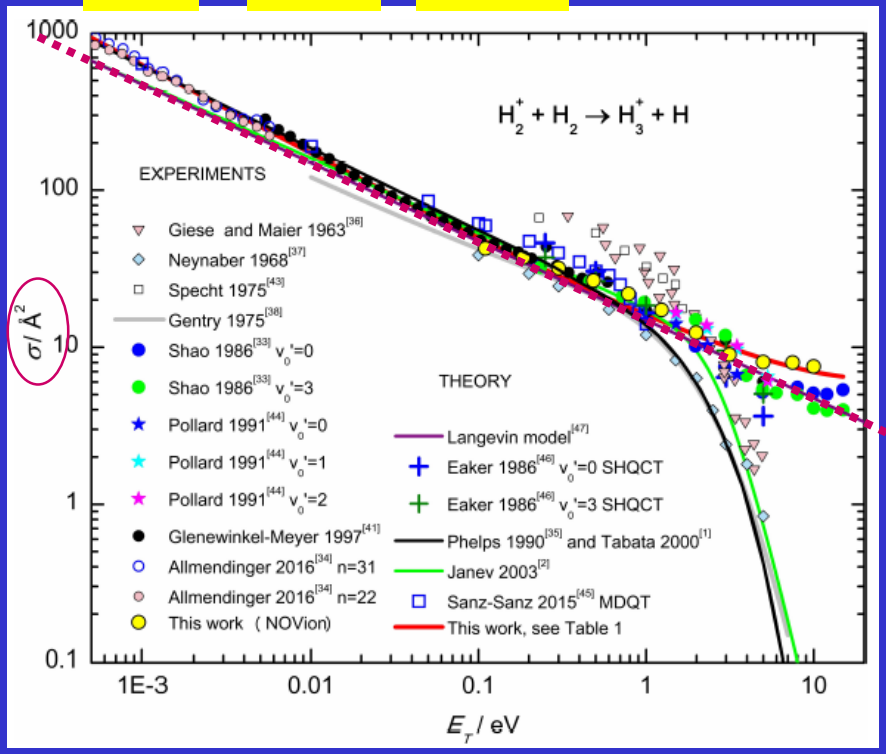

$\sigma_L(E_T)$

$k(T)/k_L=1$

0.1 K | 1 K | T[K]

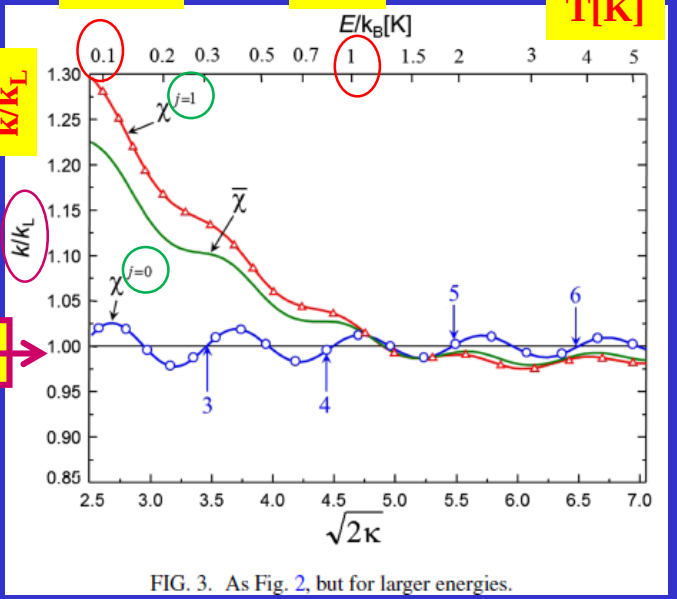

FIG. 3. As Fig. 2, but for larger energies.

For large energies ~0.001 – 10 eV

For large energies ~10 – 100 000 K

For lower energies ~ 0. 1 – 5 K

Older experiments and theory

Electron scattering cross-section on Ar

$$k = \int_v f_T(v).v.\sigma(v)dv = k(T)$$

Electrons – Boltzman distribution with T_e

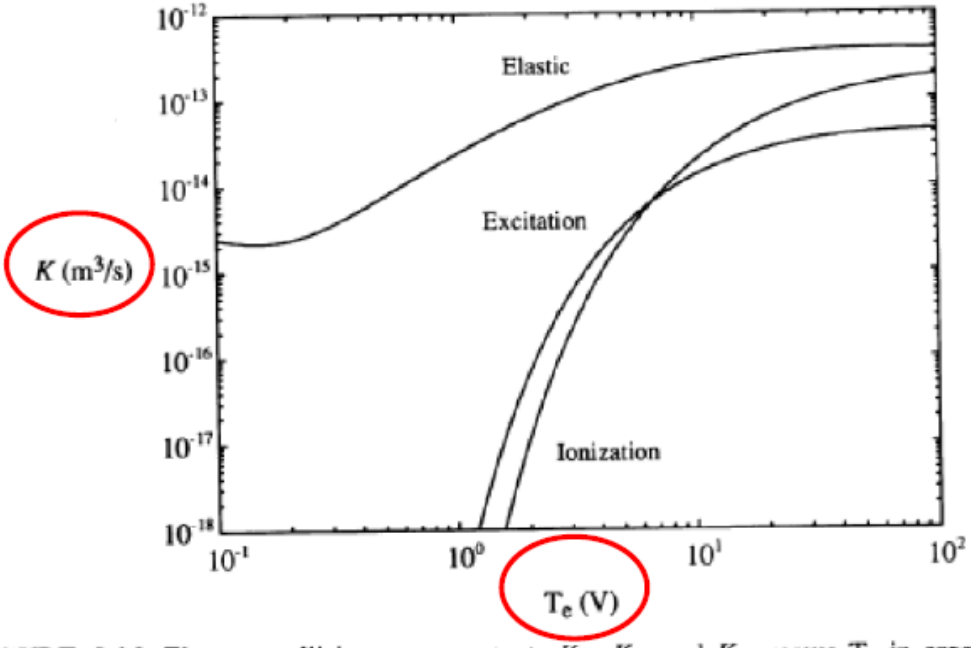

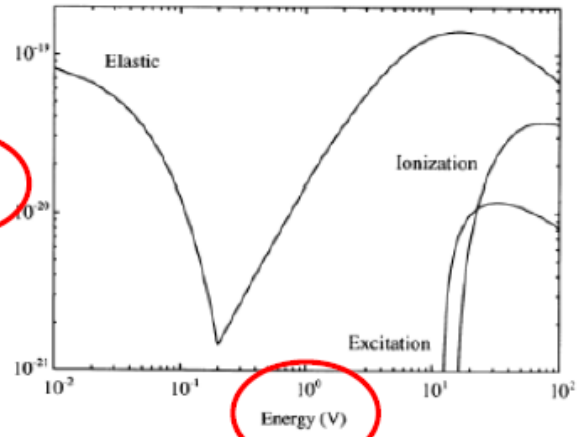

3. Ionization, excitation and elastic scattering cross sections for electrons in ıpiled by Vahedi, 1993).

$$\alpha(T, T_e) \propto \int_0^\infty \sqrt{E}\,\sigma_w(E, T) f(E, T_e) dE$$

FIGURE 3.16. Electron collision rate constants K_{iz}, K_{ex} and K_m versus T_e in argon gas (compiled by Vahedi, 1993).

What if we have metastables?

Lieberman&Lichtenberg

IMR thermal

$$\sigma = \pi\rho_0^2 = \frac{2\pi e}{v_0(4\pi\varepsilon_0)}\sqrt{\frac{\alpha}{\mu}}$$

$$k = \int_v f_T(v).v.\sigma(v)dv = k(T)$$

$k_{coll} \sim 10^{-9} cm^3 s^{-1}$

$k_{col} = \langle v\rho \rangle \sim \langle v1/v \rangle = \text{const.}$

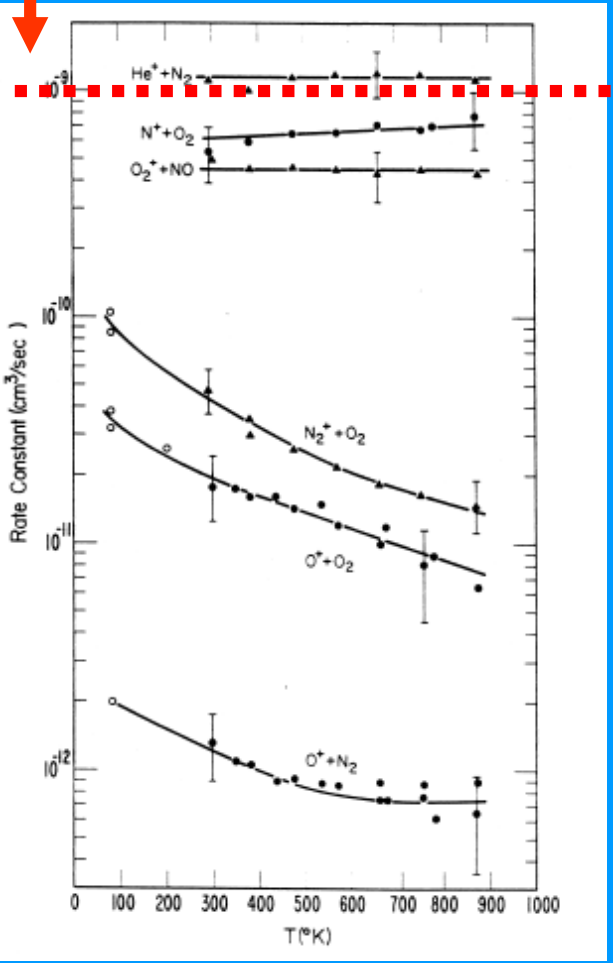

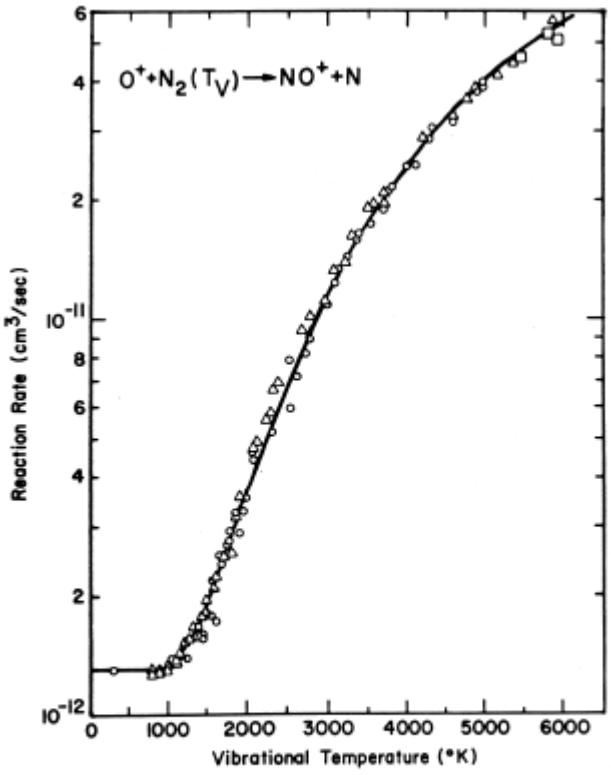

Fig. 12. Measurements of the variation of the rate coefficient for the reaction of $O^+ + N_2 \rightarrow NO^+ + N$ with the vibrational temperature of N_2 [16].

Ionic composition of the atmosphere

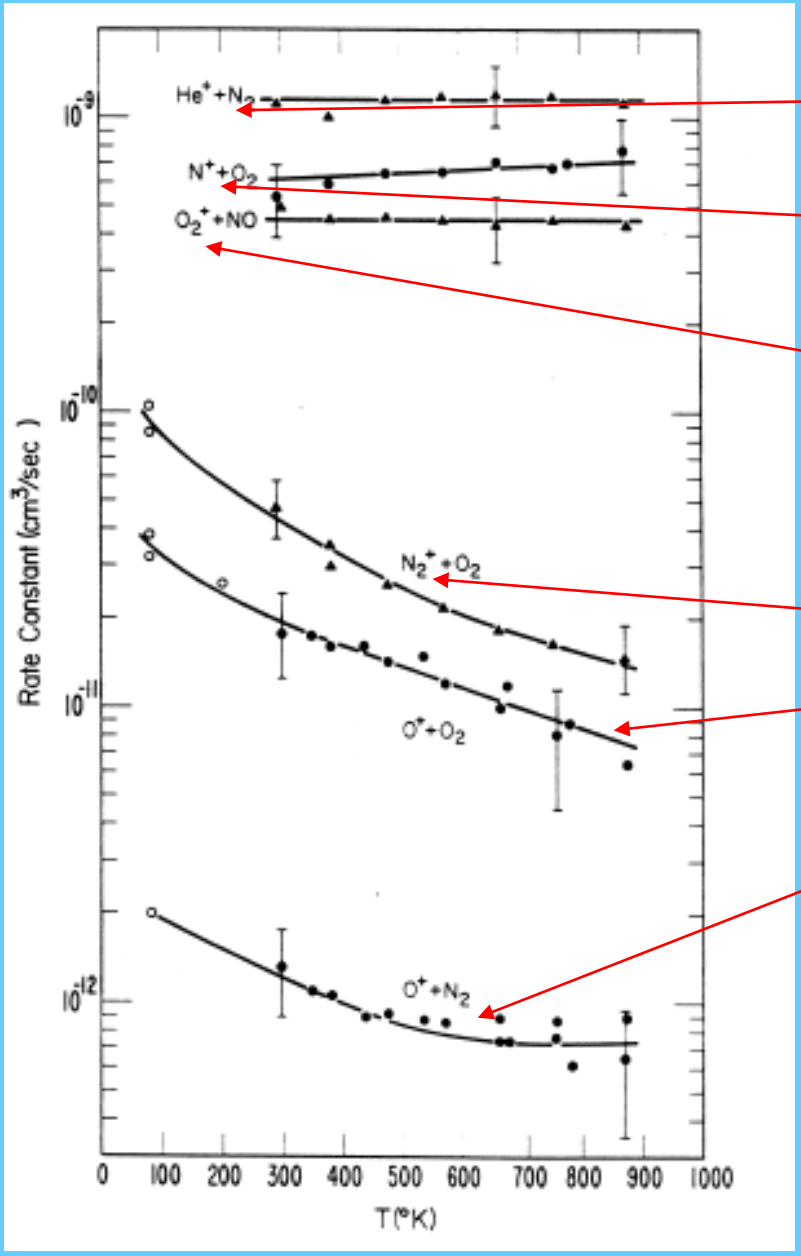

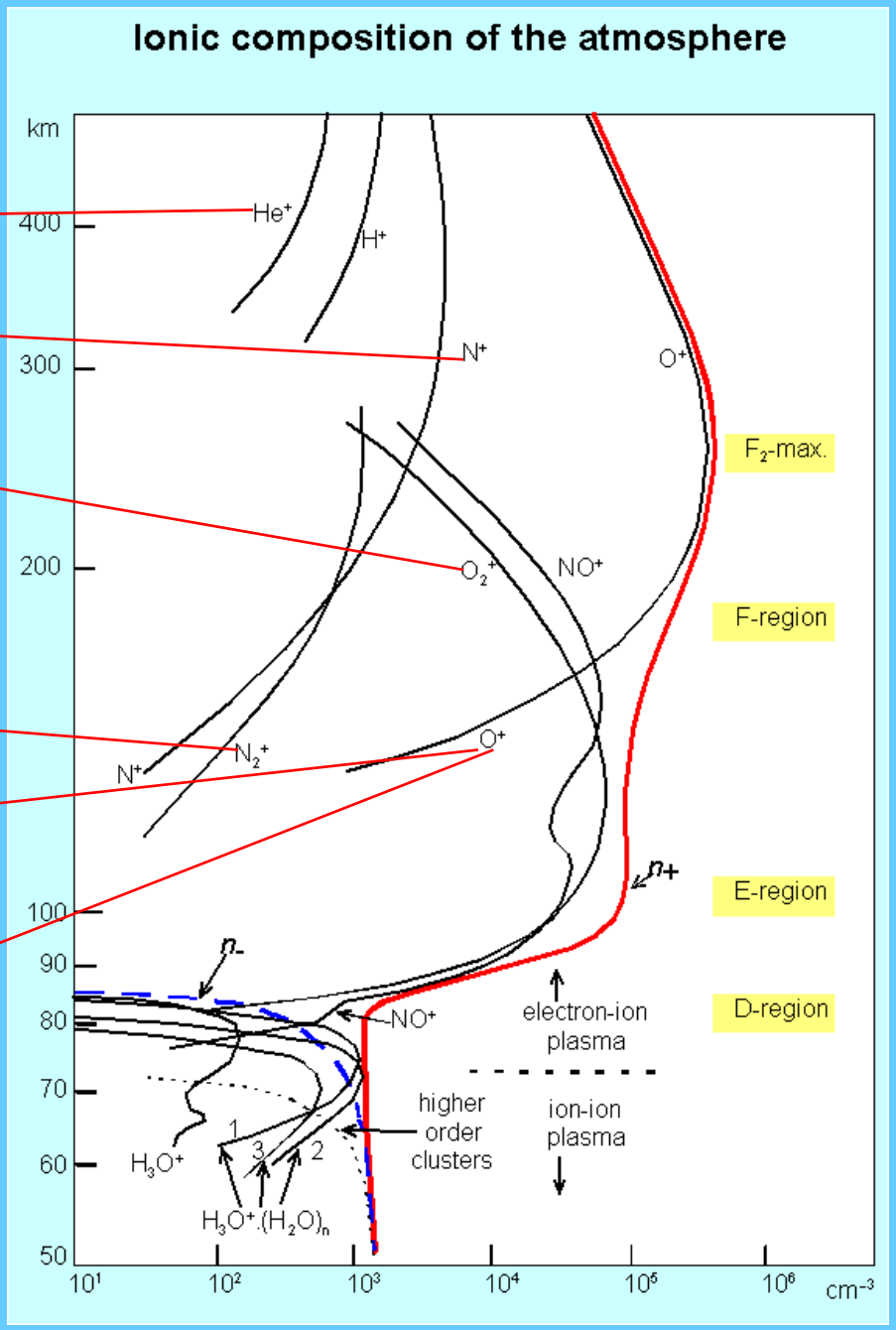

Reaction Rate of IMR relevant for ionosphere

k_{IMR}

$k_{coll} \sim 10^{-9} cm^3 s^{-1}$

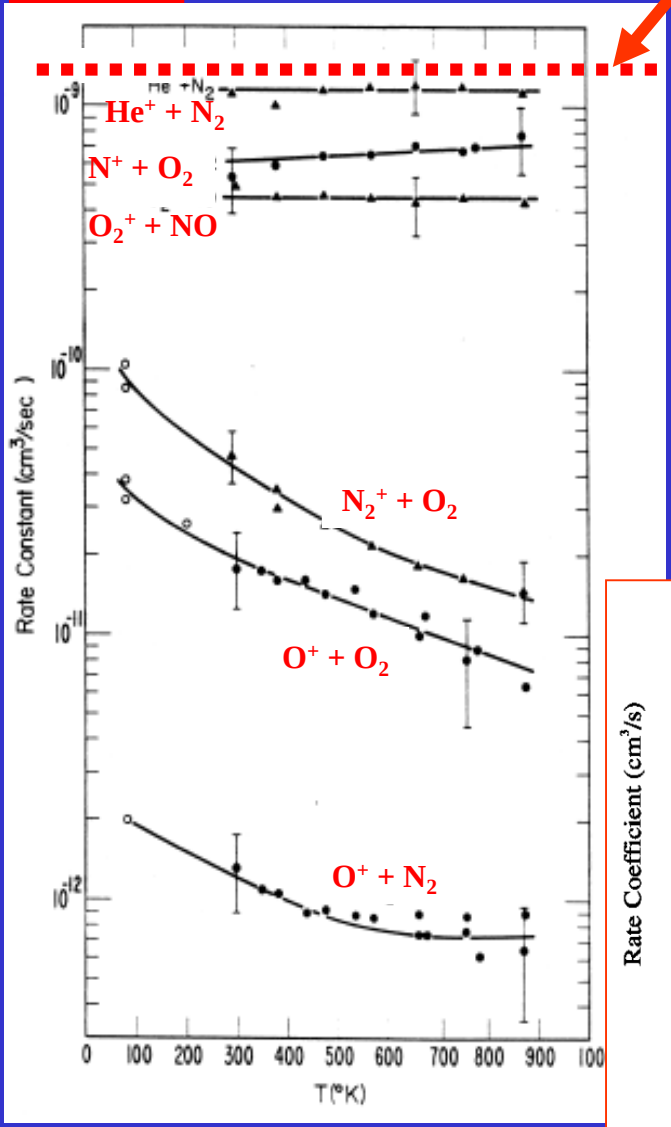

1975-90

1990-00

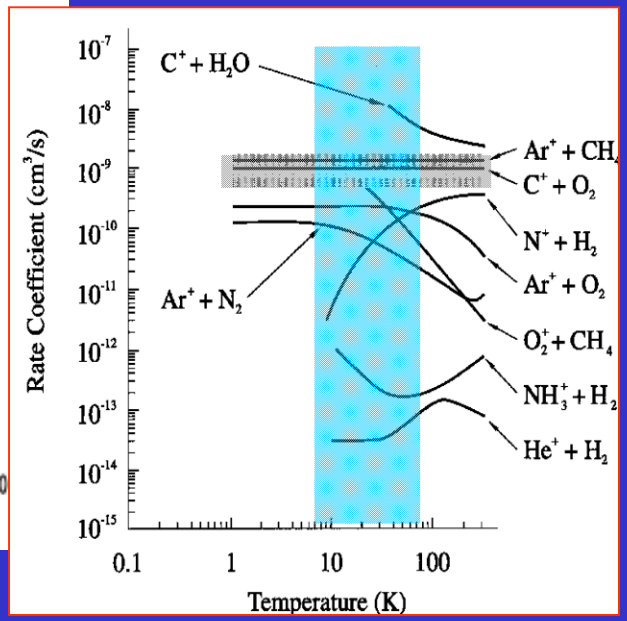

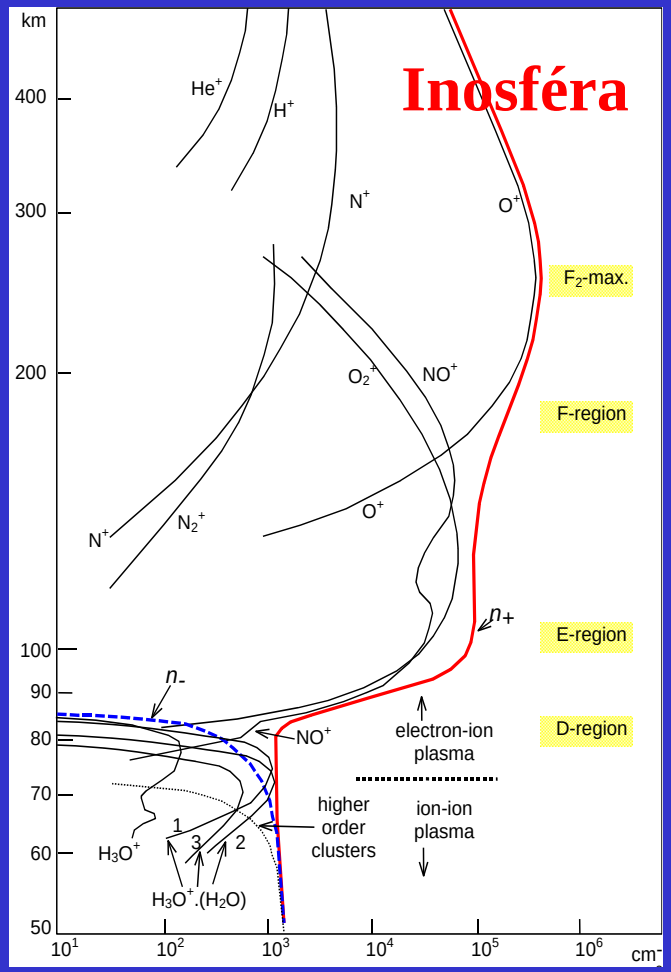

Reacation cross section

$$A^+ + B \rightarrow C^+ + D$$

$$\frac{dA^+}{dt} = -k_{BIN} A^+ B$$

$$H_3^+ + D_2 \rightarrow D_2H^+ + H_2$$

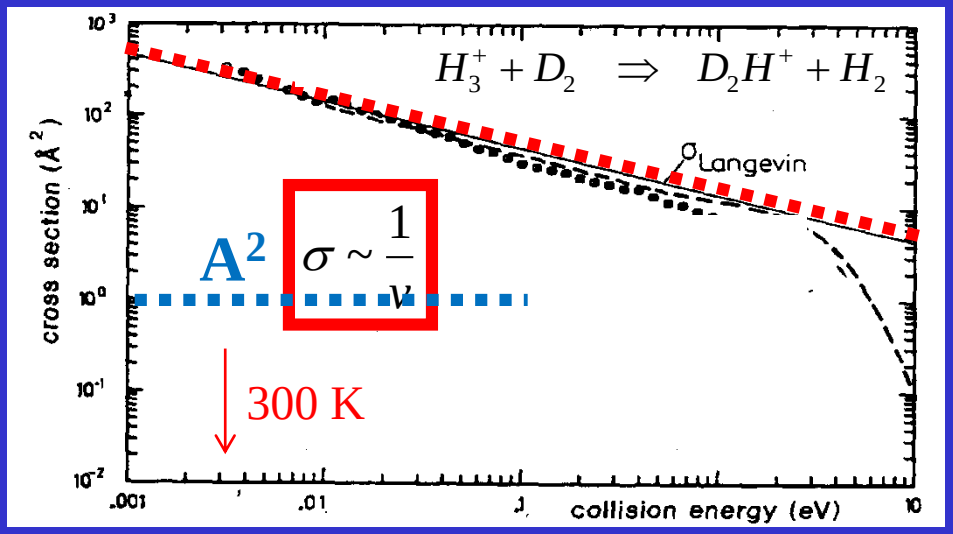

$$CCl_4 + e \rightarrow Cl^- + CCl_3$$

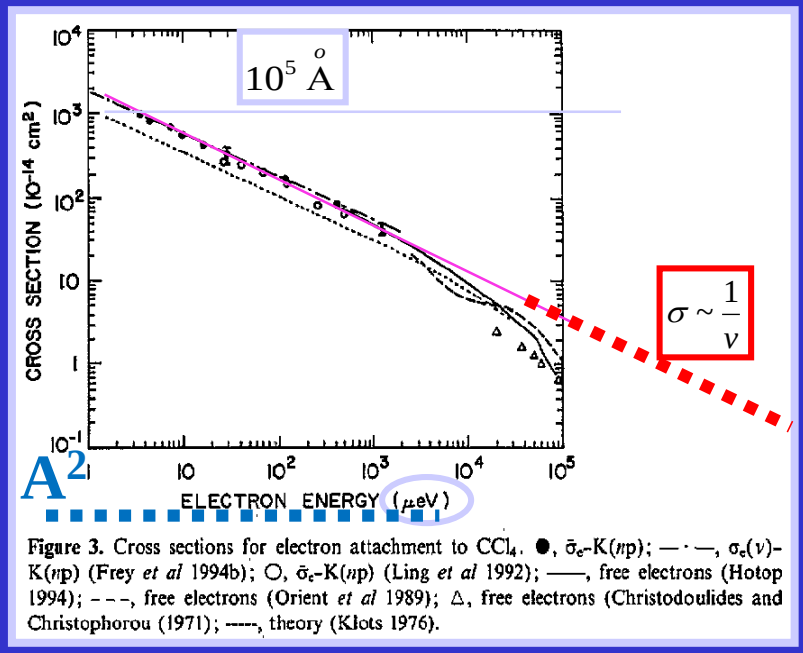

Figure 3. Cross sections for electron attachment to CCl_4. ●, $\bar{\sigma}_e$-K(*np*); —·—, $\sigma_e(v)$-K(*np*) (Frey *et al* 1994b); ○, $\bar{\sigma}_e$-K(*np*) (Ling *et al* 1992); ——, free electrons (Hotop 1994); – – –, free electrons (Orient *et al* 1989); △, free electrons (Christodoulides and Christophorou (1971); -----, theory (Klots 1976).

Interstellar medium

92.1% of nucleons in the universe are protons
7.8% are helium nuclei !
0.1%……C,N,O,S,Si….

Cosmic abundance

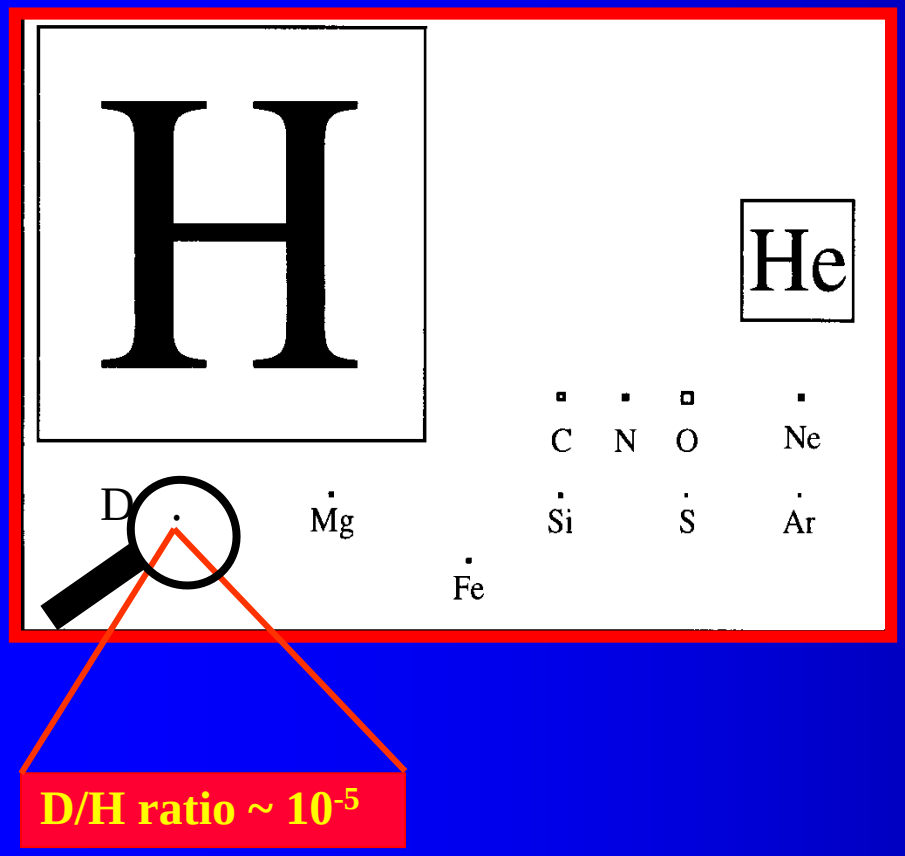

D/H ratio ~ 10^{-5}

@ 10-50K

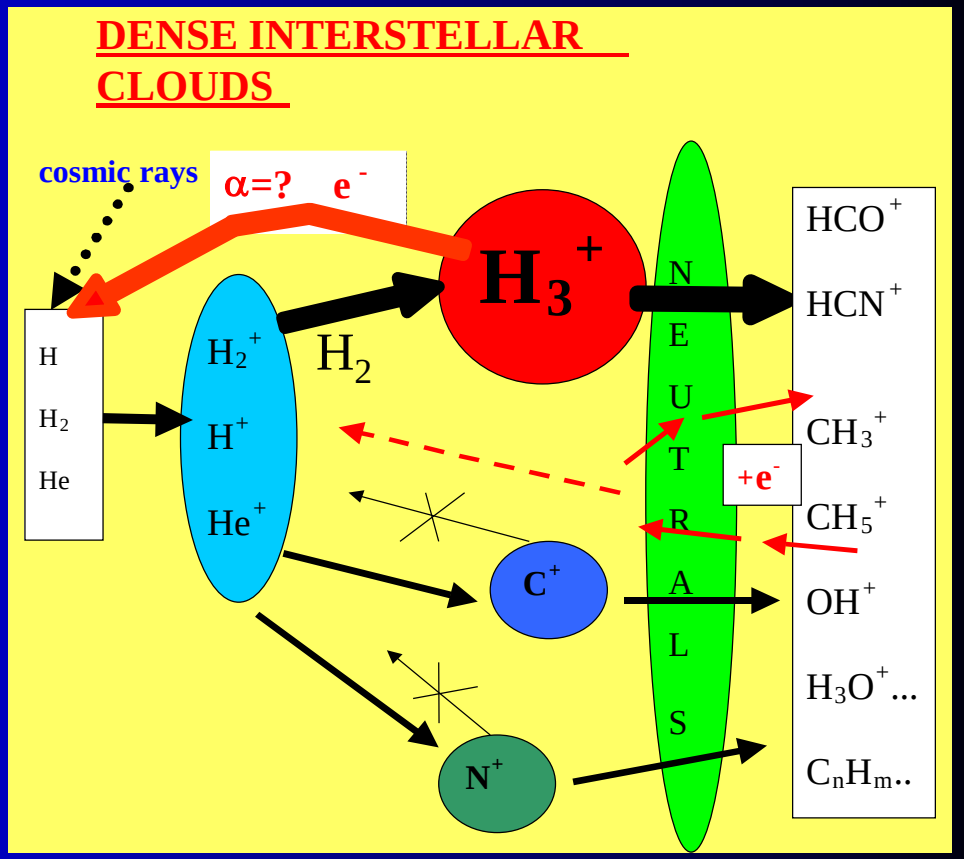

$$H_3^+ + e^- \xrightarrow{\alpha} neutral\ products$$

α (10 K) = ????

$H_3^+ + e^- \rightarrow H + H_2; 3H$

Cross section

Single collision

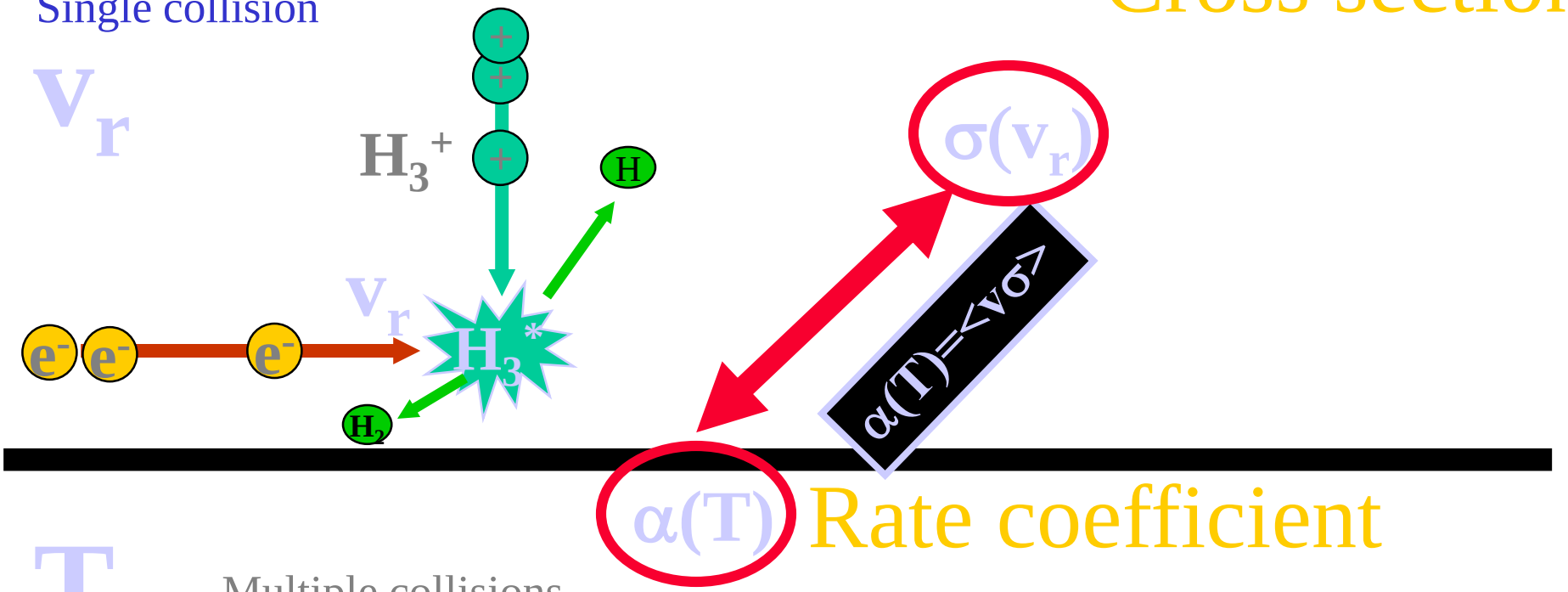

Rate coefficient

T

Multiple collisions

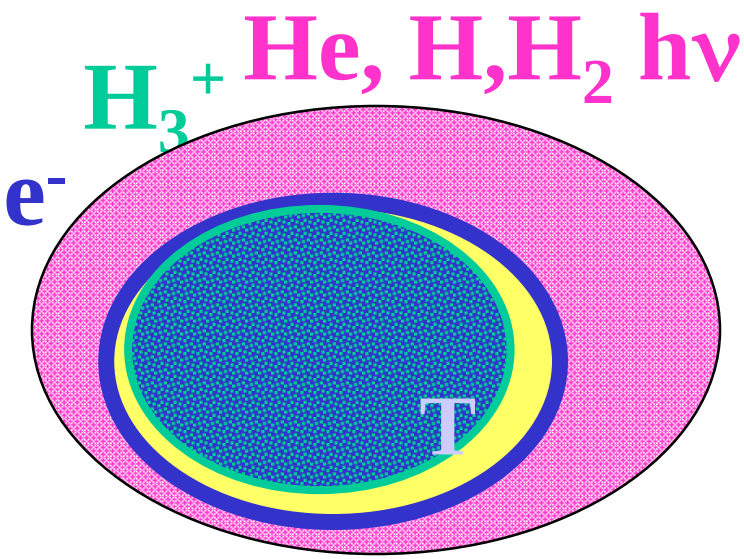

$dn_e/dt=-\alpha n_i n_e=-\alpha n_e^2$

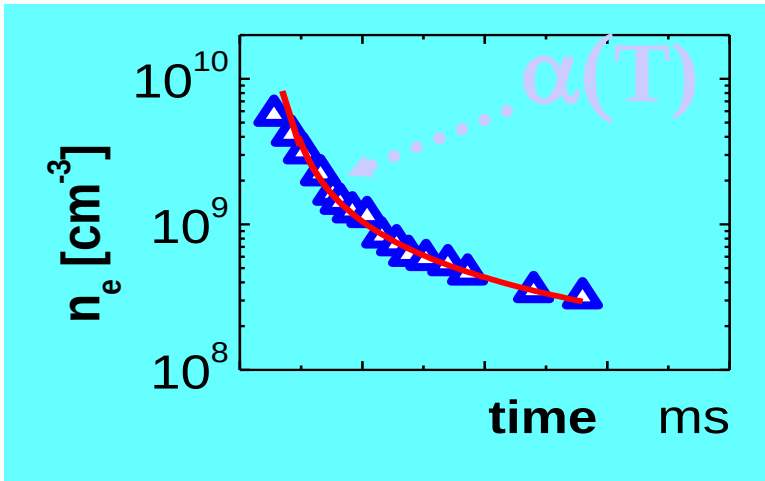

Balance in ISM

Cosmic-ray ionisation rate $\gamma \sim 3 \times 10^{-17} s^{-1}$

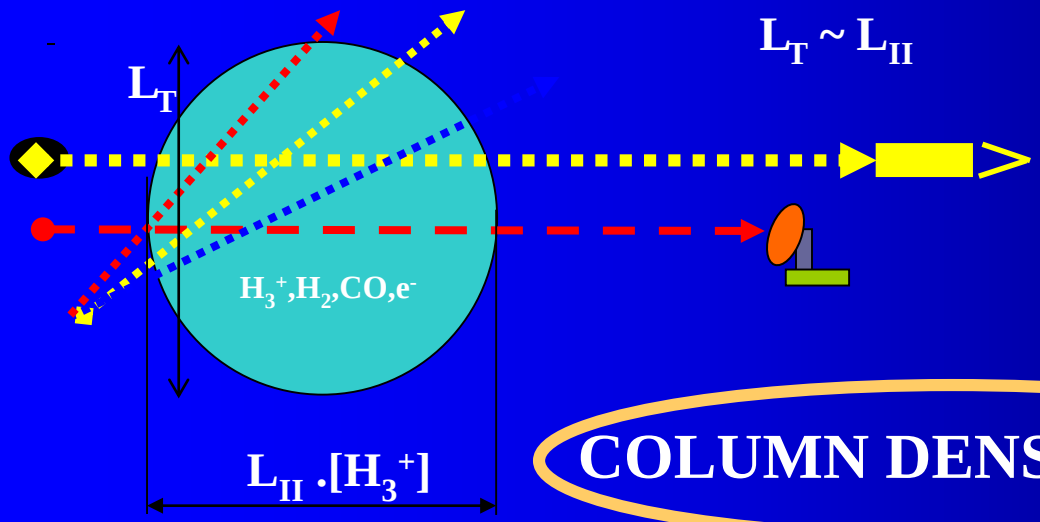

COLUMN DENSITY $N(H_3^+)$

PRODUCTION: $H_2 + h\nu(CR) \rightarrow H_2^+ + H_2 \rightarrow H_3^+$ $\quad d[H_3^+]/dt \sim \gamma . [H_2]$

a) DENSE CLOUDS: DESTRUCTION:

$H_3^+ + CO \rightarrow HCO^+ + H_2$

$k_{CO} = 2 \times 10^{-9} cm^3 s^{-1}$

$d[H_3^+]/dt \sim -k_{CO} x [H_3^+] x [CO]$

$d[H_3^+]/dt \sim \gamma . [H_2]$

$[H_3^+] = \gamma / k_{CO} . [H_2]/[CO] = \sim 1 \times 10^{-4} cm^{-3}$

~OK with observation

b) DIFFUSE CLOUDS: DESTRUCTION: $H_3^+ + e^-$

$d[H_3^+]/dt \sim - \alpha_{DR} [H_3^+][e^-]$

$[e^-] \sim [C]$

$\alpha_{DR} = 2 \times 10^{-7} cm^3 s^{-1} x (T/300)^{-0.65}$?

$[H_3^+] = \gamma / \alpha_{DR} . [H_2]/[C] = \sim 1 \times 10^{-7} cm^{-3}$

$d[H_3^+]/dt \sim \gamma . [H_2]$

~ NO with observation

Low energy collisions with molecules

Collisions of electrons with atoms (atomic beams)

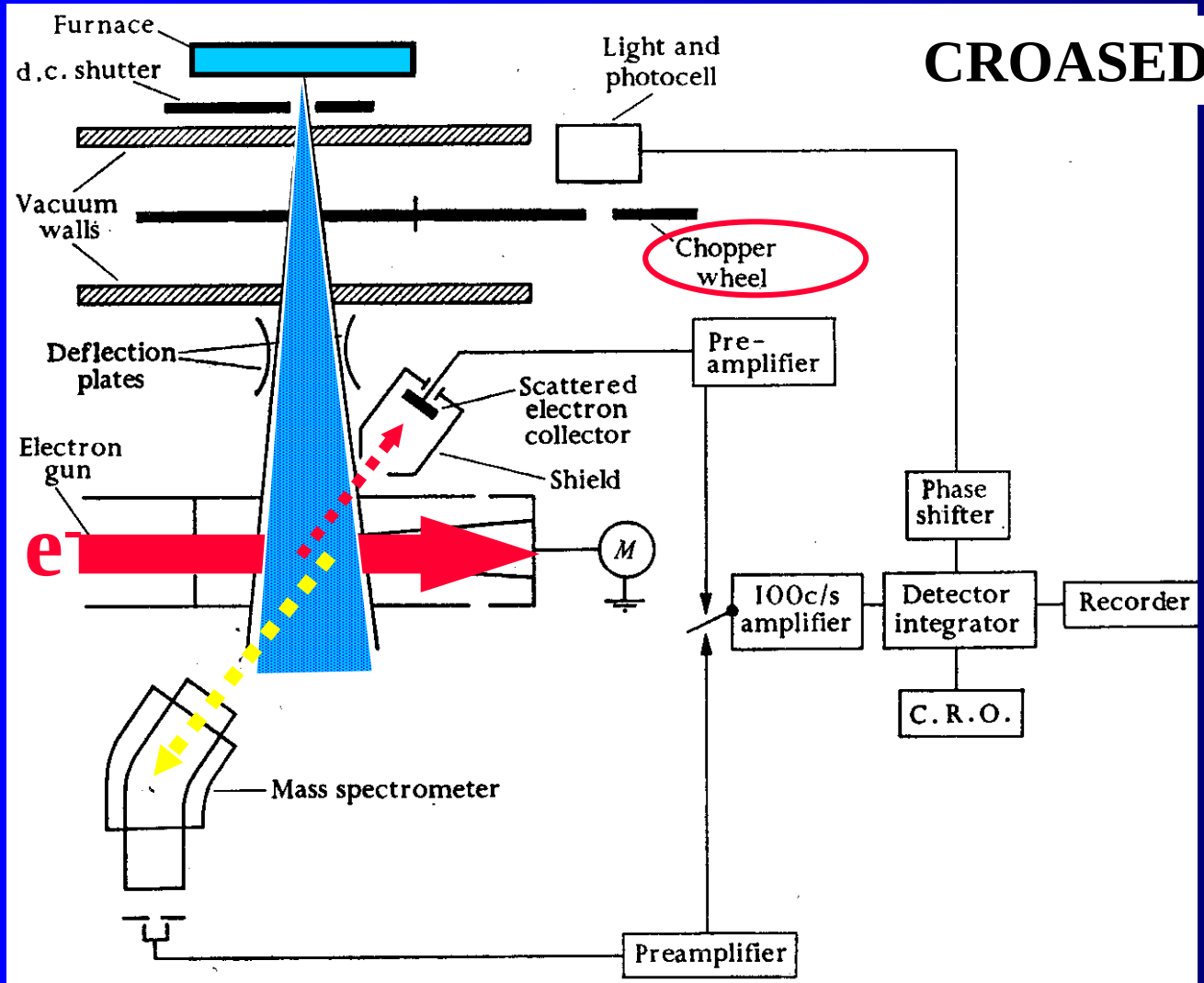

FIG. 1.2. Schematic diagram of the arrangement of apparatus used by Fite, Brackmann, and Neynaber for observation of elastic scattering of electrons by atomic hydrogen.

CROASED BEAM METHOD

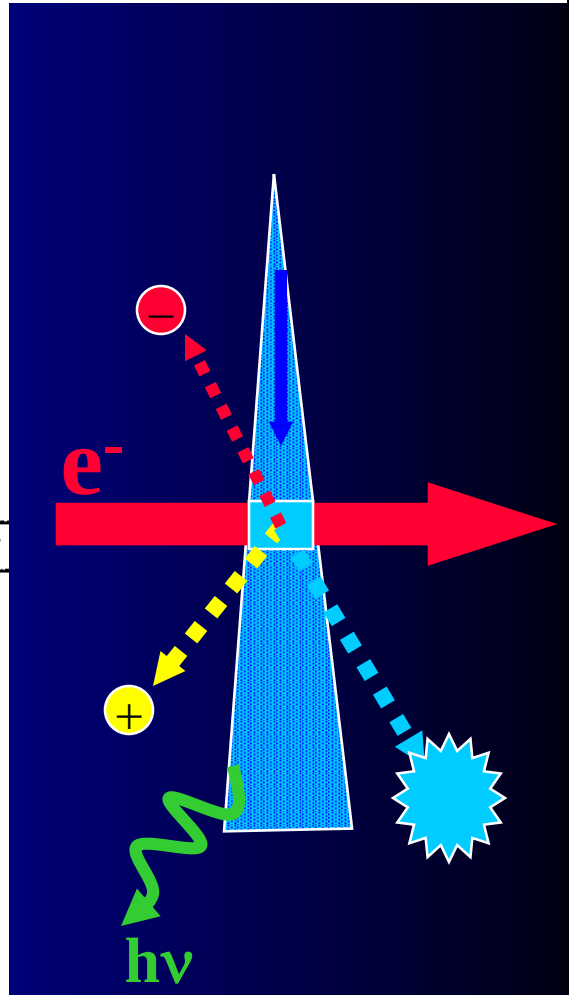

Position (angle), mass and energy sensitive detectors

Partial cross section for excitation

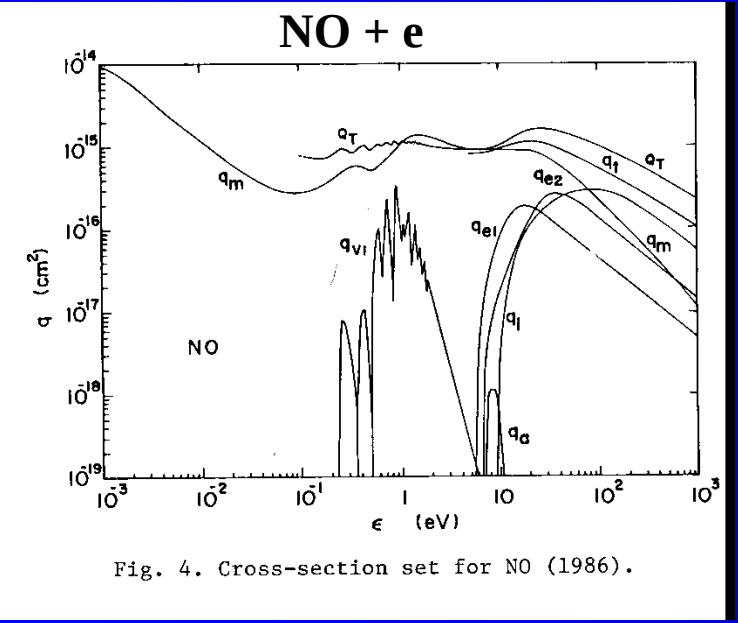

Fig. 4. Cross-section set for NO (1986).

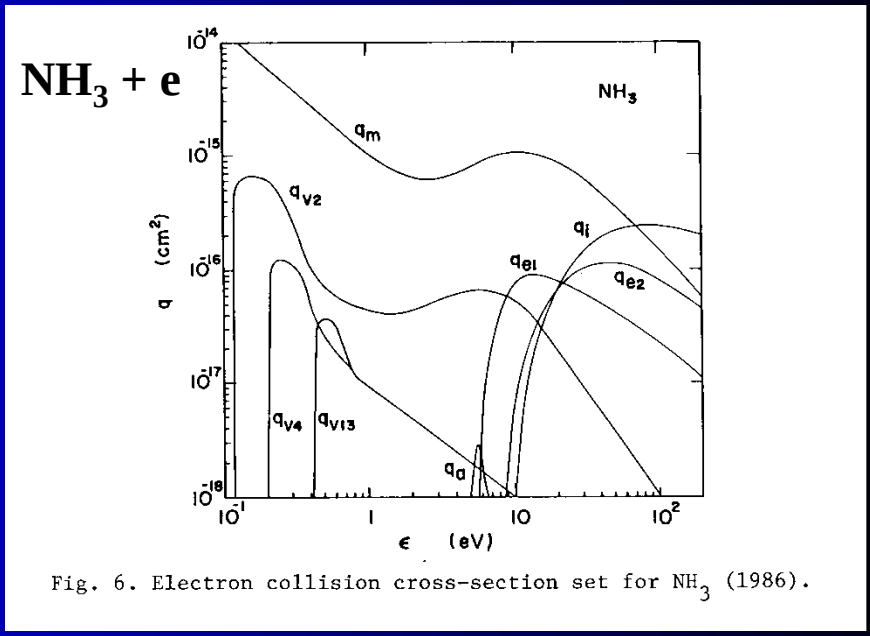

Fig. 6. Electron collision cross-section set for NH_3 (1986).

10^5 Å

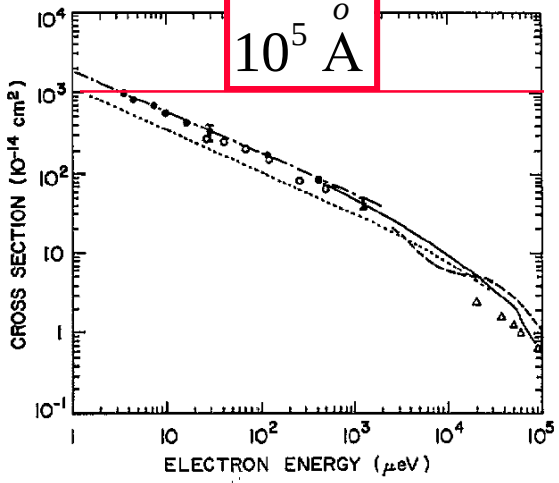

Figure 3. Cross sections for electron attachment to CCl_4. ●, $\bar{\sigma}_e$-K(np); —·—, $\sigma_c(v)$-K(np) (Frey *et al* 1994b); ○, $\bar{\sigma}_e$-K(np) (Ling *et al* 1992); ——, free electrons (Hotop 1994); – – –, free electrons (Orient *et al* 1989); △, free electrons (Christodoulides and Christophorou (1971); -----, theory (Klots 1976).

$$e^- + SF_6 \rightarrow SF_6^{-*}$$

$$e^- + CCl_4 \rightarrow CCl_4^{-*} \rightarrow CCl_3 + Cl^-$$

Total collision cross sections Na, K, Cs…

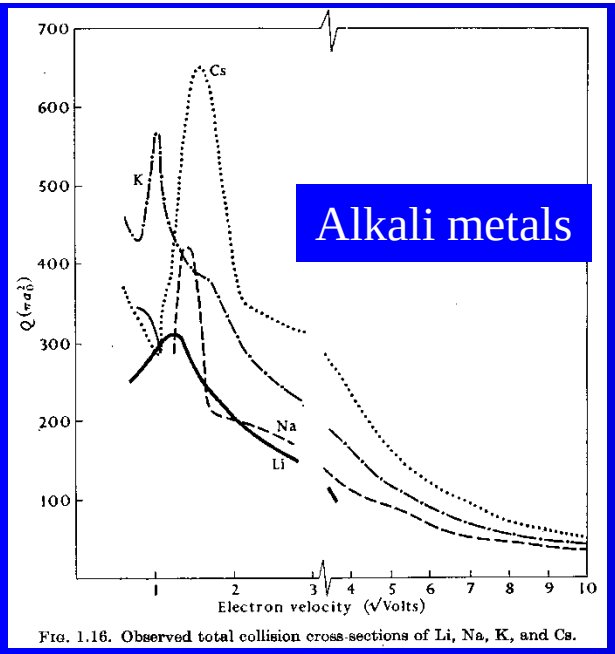

FIG. 1.16. Observed total collision cross-sections of Li, Na, K, and Cs.

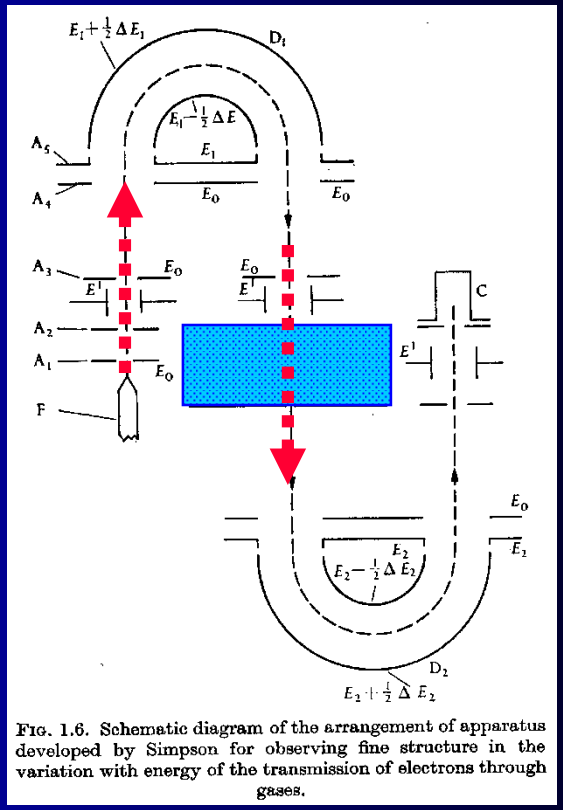

FIG. 1.6. Schematic diagram of the arrangement of apparatus developed by Simpson for observing fine structure in the variation with energy of the transmission of electrons through gases.

Cs

$e^-_{(v)}$

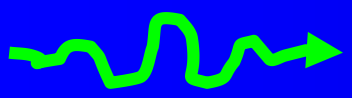

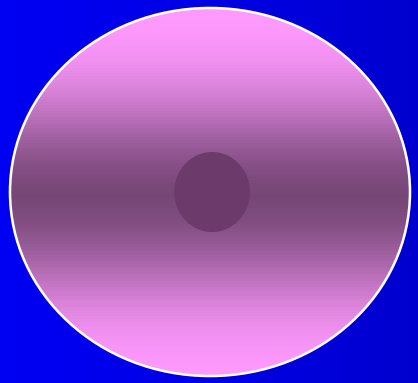

Total collision and reactive cross sections comparison

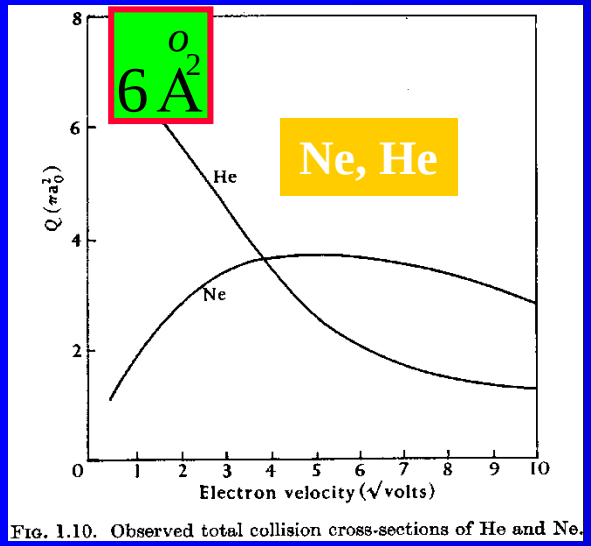

FIG. 1.10. Observed total collision cross-sections of He and Ne.

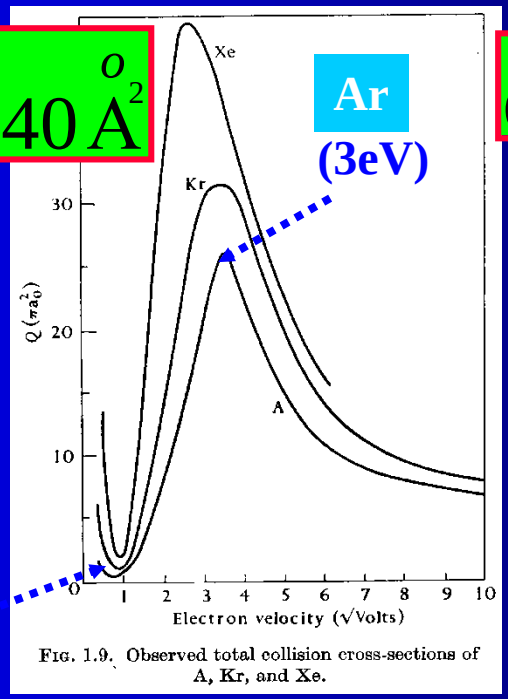

FIG. 1.9. Observed total collision cross-sections of A, Kr, and Xe.

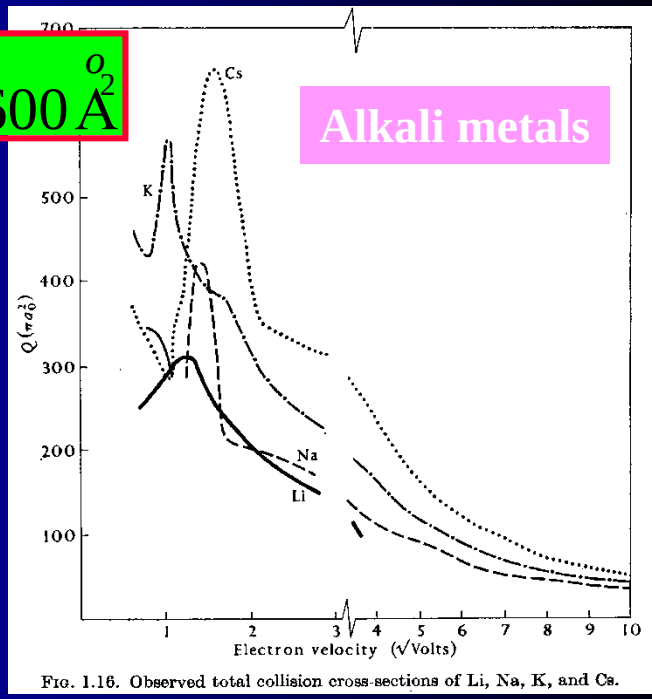

FIG. 1.16. Observed total collision cross-sections of Li, Na, K, and Cs.

(0,3eV)

σ(v)

e⁻ (v)

Ar
(3eV)

Ne

Ar
(0.3eV)

500A

Cs

(2eV)

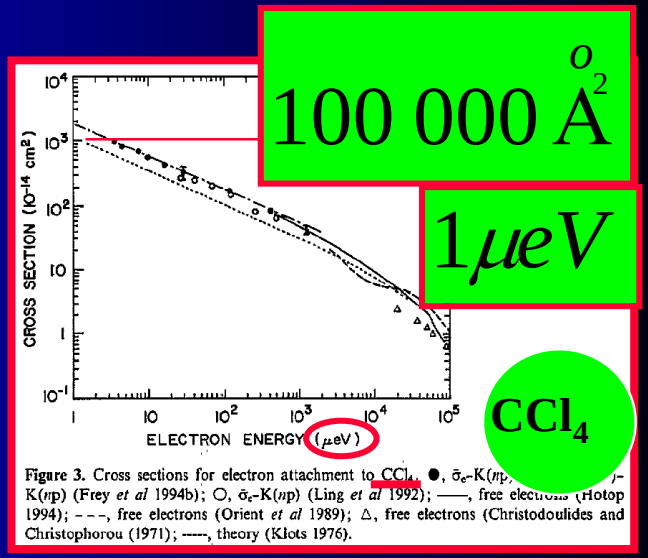

Figure 3. Cross sections for electron attachment to CCl_4. ●, $\bar{\sigma}_e$-K(np,); K(np) (Frey *et al* 1994b); ○, $\bar{\sigma}_e$-K(np) (Ling *et al* 1992); ——, free electrons (Hotop 1994); – – –, free electrons (Orient *et al* 1989); △, free electrons (Christodoulides and Christophorou (1971); ------, theory (Klots 1976).

Collisions of electrons with atoms – Ramsauer's method

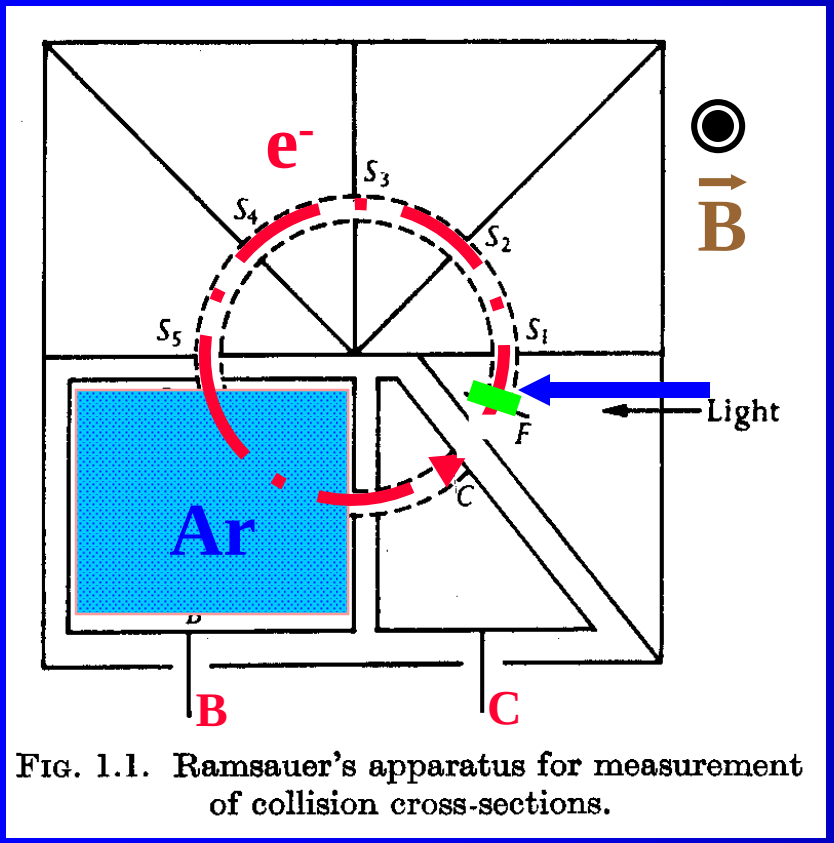

FIG. 1.1. Ramsauer's apparatus for measurement of collision cross-sections.

Lenard 1903
Akesson 1916
Ramsauer 1921

ATENUATION METHOD

$$\delta I = -N\sigma I_p \, \delta x$$

$$I_P = I_0 \exp(-\sigma N x)$$

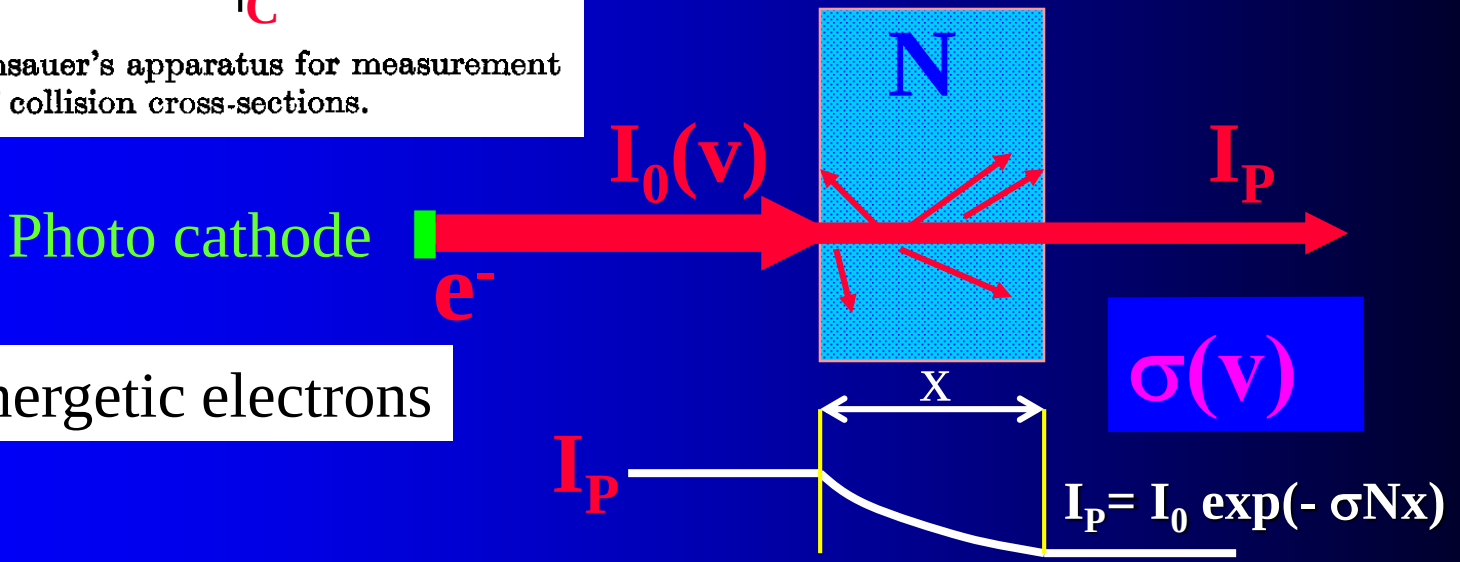

Mono energetic electrons

Collisions of electrons with atoms – Ramsauer's method

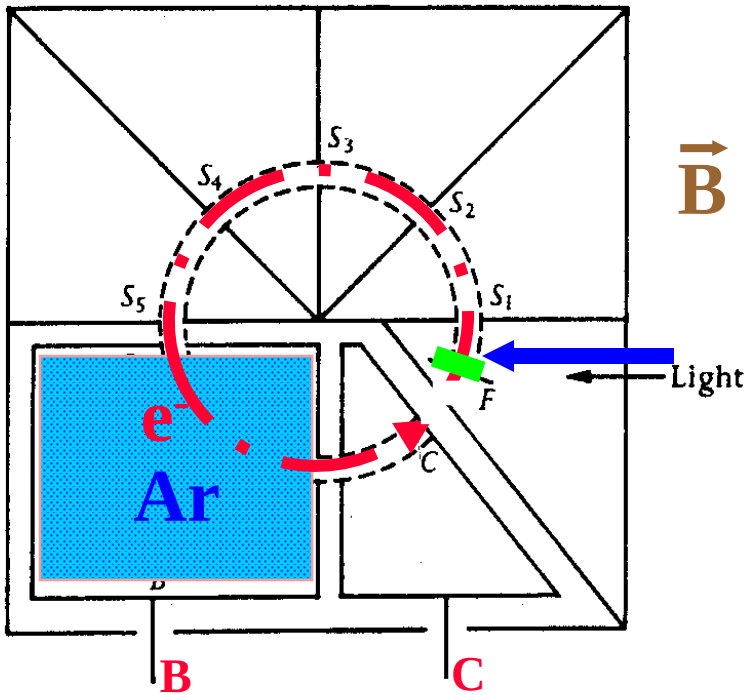

FIG. 1.1. Ramsauer's apparatus for measurement of collision cross-sections.

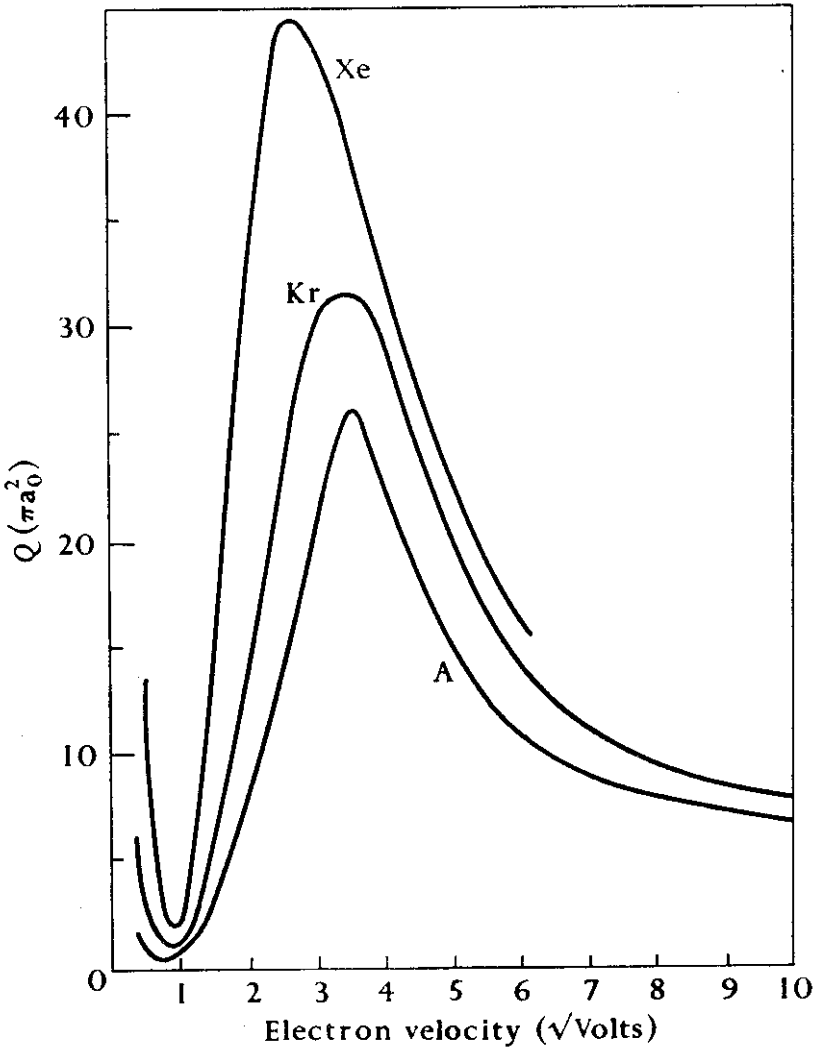

FIG. 1.9. Observed total collision cross-sections of A, Kr, and Xe.

Lenard 1903
Akesson 1916
Ramsauer 1921

Total collision cross section – e/atoms

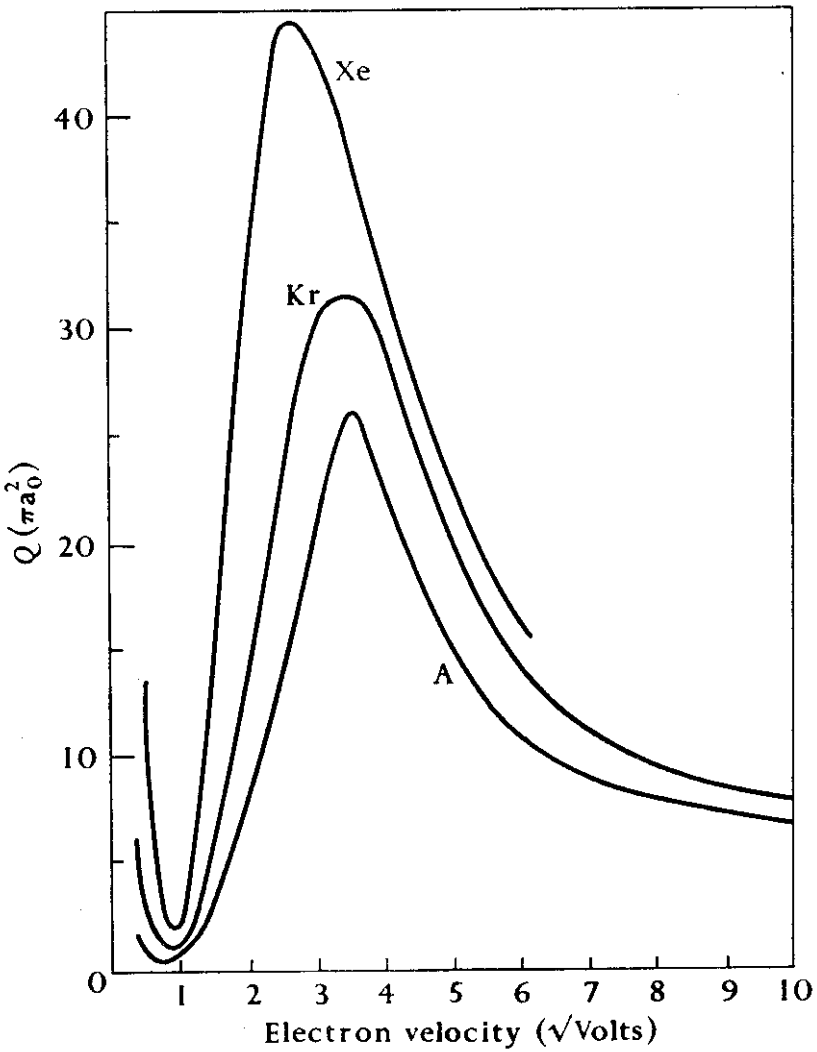

FIG. 1.9. Observed total collision cross-sections of A, Kr, and Xe.

a_0=0.53x10^{-8}cm~0.5A
Radius of the first Bohr orbit of H atom

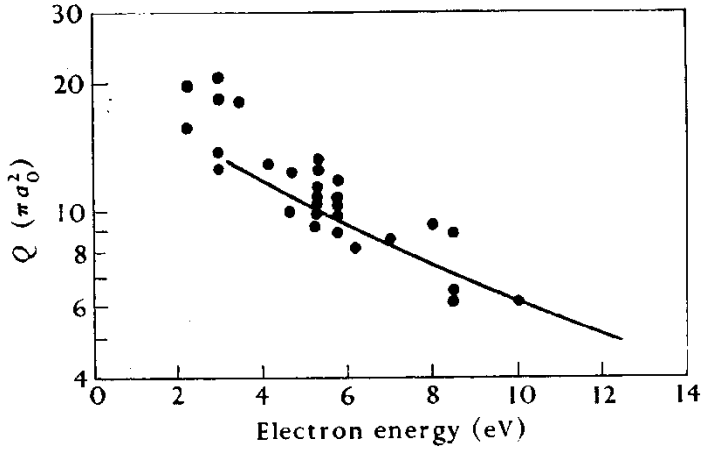

FIG. 1.11. Total collision cross-sections of atomic hydrogen. ● observed by Brackmann, Fite, and Neynaber; —— observed by Neynaber, Marino, Rothe, and Trujillo.

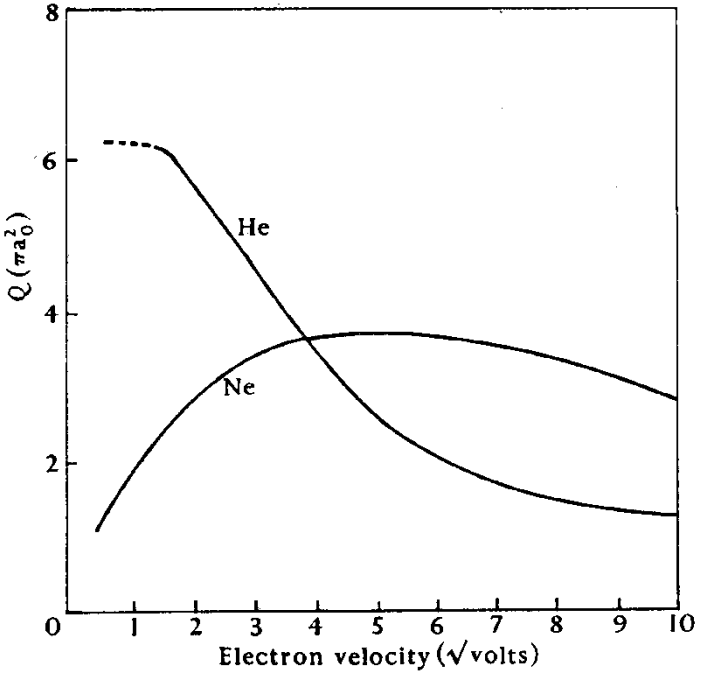

FIG. 1.10. Observed total collision cross-sections of He and Ne.

Details of Ramsauer effect

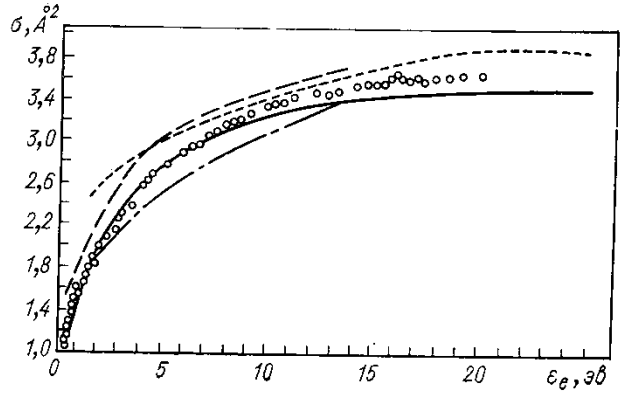

Рис. 5.8. Полное сечение рассеяния электрона на атоме неона.

Эксперимент (метод Рамзауэра): ○ — [101]; ——— — [29]; ····· —[92]; — · — — [95]. Теория: — — — [109].

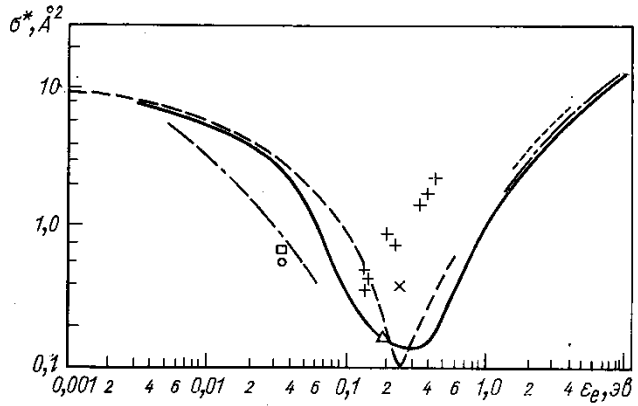

Рис. 5.9. Диффузионное сечение столкновения электрона с атомом аргона.

Эксперимент (подвижность электронов при малых полях и температурах): ····· — [21]; ——— — [47]; × — [60]; ○ — [91]; □ — [112]; △ — [44]; — · — — [16]; — — · — — — [108]; + — [43]. Теория: — — — [87].

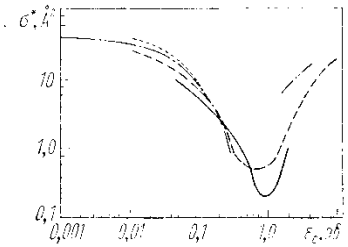

Рис. 5.12. Диффузионное сечение столкновения электрона с атомом криптона.

Эксперимент (подвижность электронов при малых полях и температурах): ····· — [34]; — ·· — — [21]; — — — — [47]; ——— — [63]. Теория: — · — — [87].

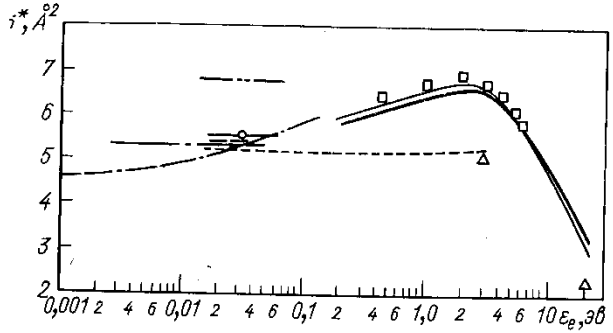

Рис. 5.3. Диффузионное сечение столкновения электрона с атомом гелия.

Эксперимент (подвижность электронов при малых полях и температурах): □ — [39]; △ — [73]; — · — — [88]; — — — — [91]; ····· — [58]; — ····· — — [13]; —○— — [62]. Теория: ——— — [75]; ——— — [32]; — · — · — — расчет по формуле (5.37).

Frequencies of elastic collisions

$\delta I = -NQI_p \delta x$

$I_P = I_0 \exp(-QNx)$

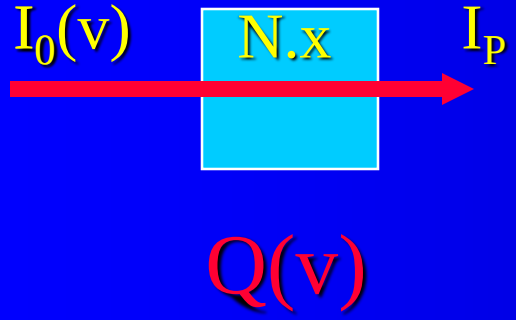

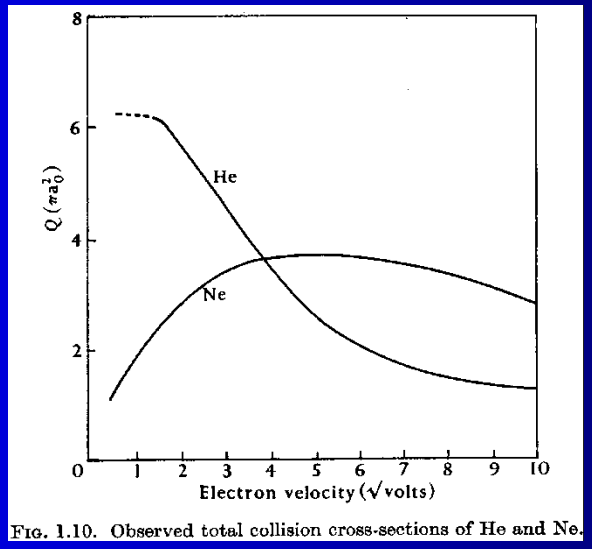

FIG. 1.10. Observed total collision cross-sections of He and Ne.

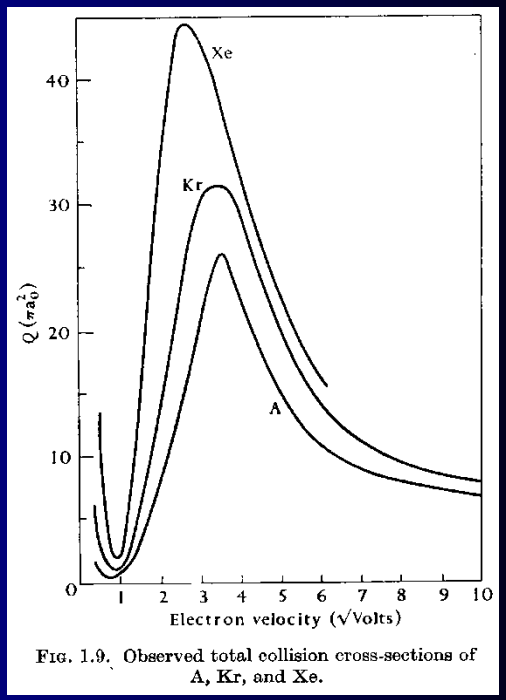

FIG. 1.9. Observed total collision cross-sections of A, Kr, and Xe.

$a_0 = 0.53 \times 10^{-8}$cm~0.5A

Radius of the first Bohr orbit of H atom

$\nu \sim n v \sigma$

Collision Frequencies

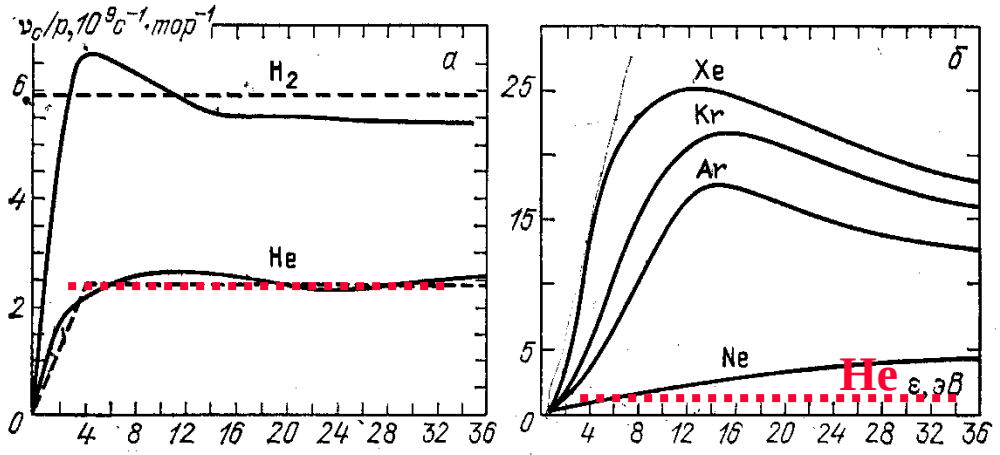

Рис. 2.5. Частоты упругих столкновений электронов, p=1 тор: *а* — в H_2 и He; *б* — в инертных газах; штриховые линии — удобная аппроксимация при расчетах [24]

Kvantová mechanika
Jednorozměrný rozptyl

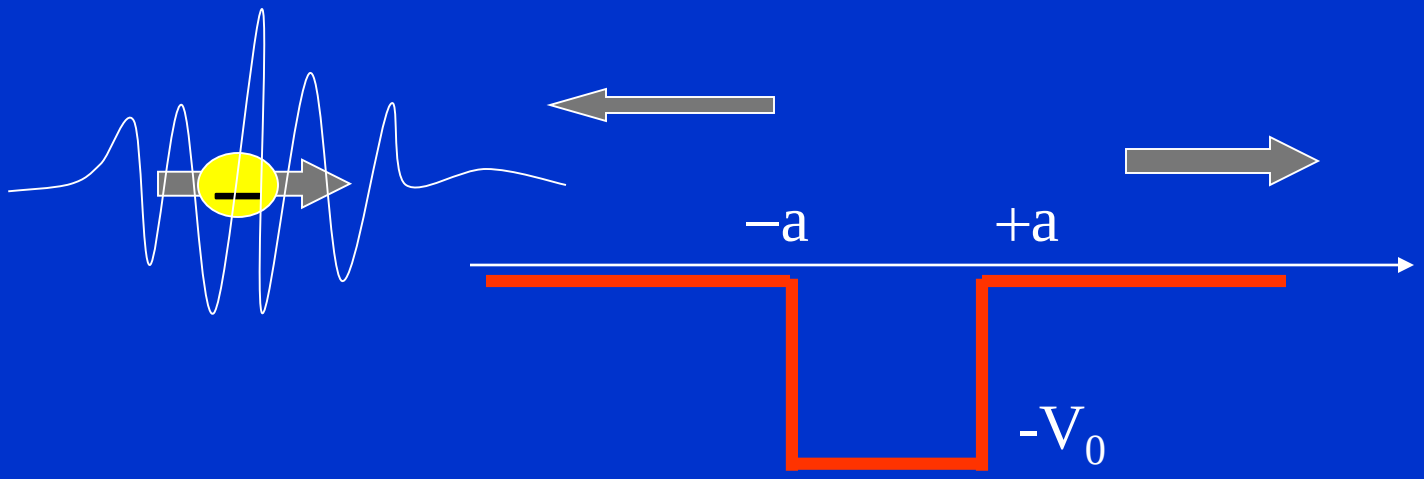

Kvantová mechanika I
J. Klíma B. Velický
MFF 1992

Jednorozměrný rozptyl

Vlnová funkce má tvar superposice Brogoliových vln

$k = \sqrt{2mE/h^2}$

$\psi_k(x,t) = (Ae^{ikx} + Be^{-ikx})e^{iE_k t/h} \quad x \le -a$

$k = \sqrt{2mE/h^2}$

$\psi_k(x,t) = (Fe^{ikx} + Ge^{-ikx})e^{iE_k t/h} \quad x > a$

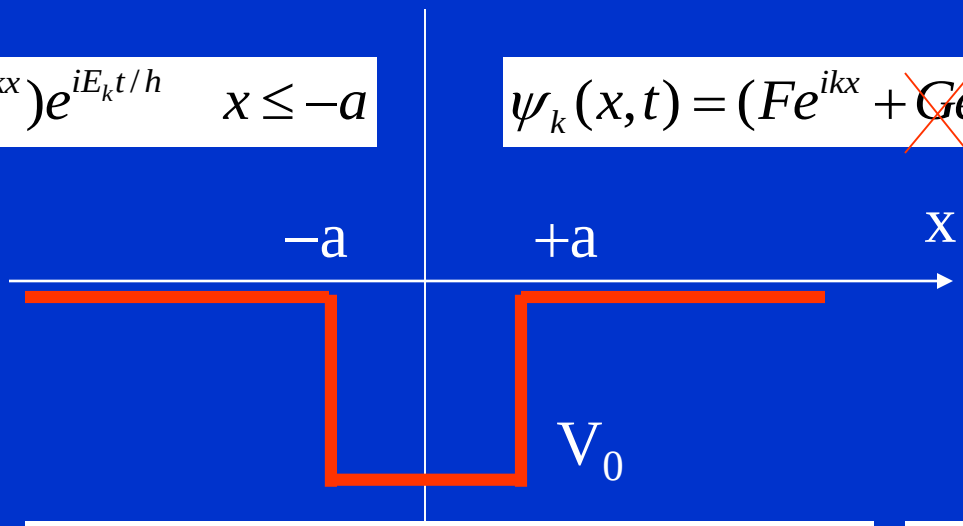

$\psi_k(x,t) = (Ce^{ik'x} + De^{-ik'x})e^{iE_k t/h} \quad |x| \le a$

$k' = \sqrt{2m(E+V_0)/h^2}$

a) dopadající částice ➔A

b) odražená částice ➔B

c) procházející částice ➔F≠0, G=0

Jednorozměrný rozptyl

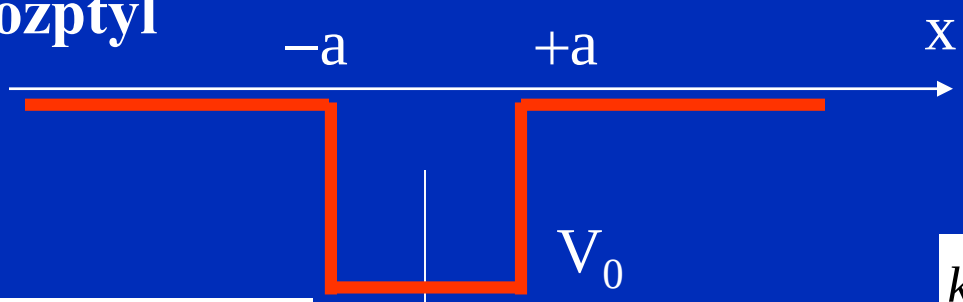

$$k = \sqrt{2mE/h^2}$$

$$k' = \sqrt{2m(E+V_0)/h^2}$$

$$\psi_k(x,t) = (Ae^{ikx} + Be^{-ikx})e^{iE_k t/h} \qquad x \le -a$$

$$\psi_k(x,t) = (Ce^{ik'x} + De^{-ik'x})e^{iE_k t/h} \qquad |x| \le a$$

$$\psi_k(x,t) = (Fe^{ikx})e^{iE_k t/h} \qquad x > a$$

Parametry jsou E, V_0 , a

Hladkost řešení v bodech ±a
Urči konstanty B, C, D, G,
Hodnota A je vstupní parametr

Tok dopadajících částic $j_{in} = \frac{hk}{m}|A|^2$

Tok odražených částic $j_{rf} = \frac{hk}{m}|B|^2$

Tok prošlých částic $j_{tr} = \frac{hk}{m}|F|^2$

Jednorozměrný rozptyl

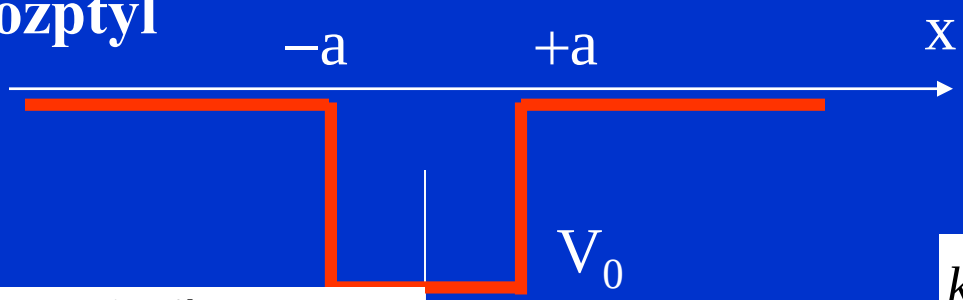

$$k = \sqrt{2mE/h^2}$$

$$k' = \sqrt{2m(E+V_0)/h^2}$$

$$\psi_k(x,t) = (Ae^{ikx} + Be^{-ikx})e^{iE_k t/h} \qquad x \le -a$$

$$\psi_k(x,t) = (Ce^{ik'x} + De^{-ik'x})e^{iE_k t/h} \qquad |x| \le a$$

$$\psi_k(x,t) = (Fe^{ikx})e^{iE_k t/h} \qquad x > a$$

Parametry jsou E, V_0 , a

Hladkost řešení v bodech ±a
Urči konstanty B, C, D, G,
Hodnota A je vstupní parametr

Tok dopadajících částic $j_{in} = \frac{hk}{m}|A|^2$

Tok odražených částic $j_{rf} = \frac{hk}{m}|B|^2$

Tok prošlých částic $j_{tr} = \frac{hk}{m}|F|^2$

$$C = \frac{F}{2}(1 + k/k')e^{i(k-k')a}$$

$$D = \frac{F}{2}(1 - k/k')e^{i(k+k')a}$$

Jednorozměrný rozptyl

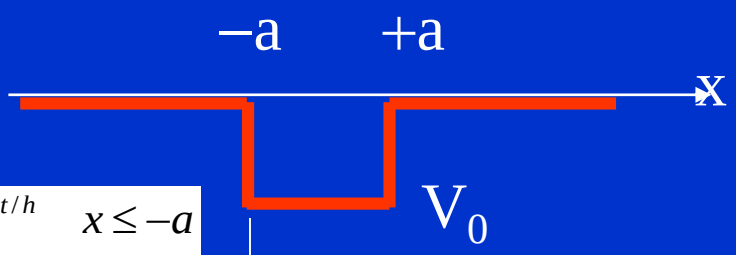

$$k = \sqrt{2mE/h^2}$$

$$k' = \sqrt{2m(E+V_0)/h^2}$$

$$\psi_k(x,t) = (Ae^{ikx} + Be^{-ikx})e^{iE_k t/h} \qquad x \le -a$$

$$\psi_k(x,t) = (Ce^{ik'x} + De^{-ik'x})e^{iE_k t/h} \qquad |x| \le a$$

$$\psi_k(x,t) = (Fe^{ikx})e^{iE_k t/h} \qquad x > a$$

Parametry jsou E, V_0 , a

$$j_{in} = \frac{hk}{m}|A|^2$$

$$j_{rf} = \frac{hk}{m}|B|^2$$

$$j_{tr} = \frac{hk}{m}|F|^2$$

Hladkost řešení v bodech ±a
Urči konstanty B, C, D, F,
Hodnota A je vstupní parametr

$$\varepsilon = \frac{k'}{k} + \frac{k}{k'}$$

$$A = e^{2ika}(\cos(2k'a) - i(\varepsilon/2)\sin(2k'a))F$$

Koeficient průchodu T, koeficient odrazu R

$$\frac{1}{T} = \left|A/F\right|^2 = 1 + \frac{V_0^2}{4E(E+V)}\sin^2(2k'a)$$

Jednorozměrný rozptyl

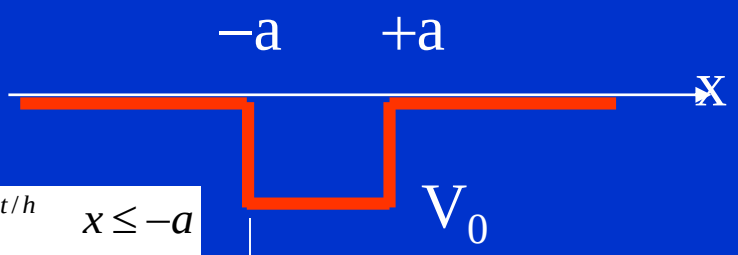

$$k = \sqrt{2mE/h^2}$$

$$k' = \sqrt{2m(E+V_0)/h^2}$$

$$\psi_k(x,t) = (Ae^{ikx} + Be^{-ikx})e^{iE_k t/h} \qquad x \le -a$$

$$\psi_k(x,t) = (Ce^{ik'x} + De^{-ik'x})e^{iE_k t/h} \qquad |x| \le a$$

$$\psi_k(x,t) = (Fe^{ikx})e^{iE_k t/h} \qquad x > a$$

Parametry jsou E, V_0 , a

$$j_{in} = \frac{hk}{m}|A|^2$$

$$j_{rf} = \frac{hk}{m}|B|^2$$

$$j_{tr} = \frac{hk}{m}|F|^2$$

Koeficient průchodu T, koeficient odrazu R

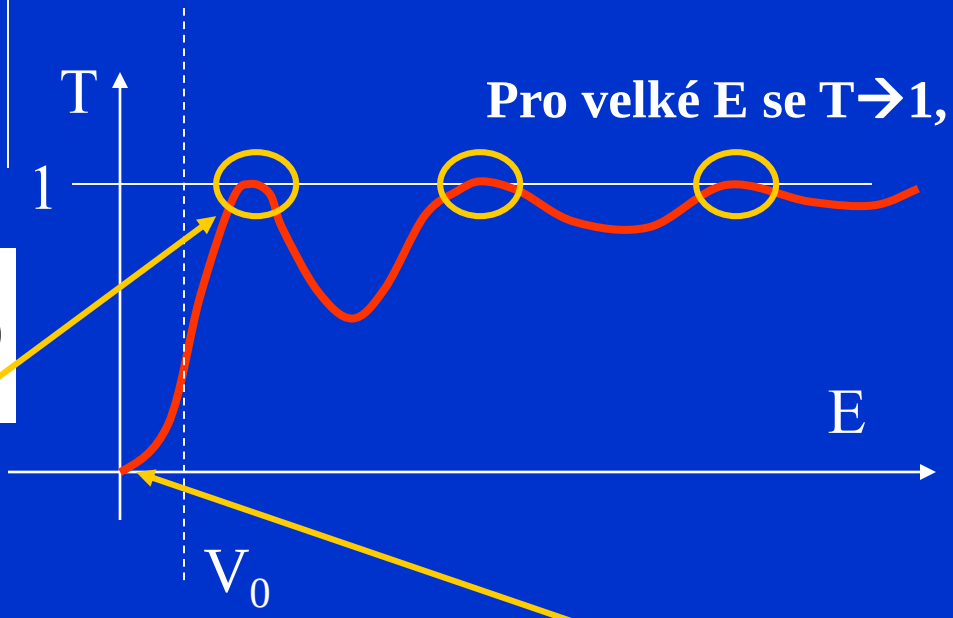

Pro velké E se T→1,

$$\frac{1}{T} = \left|\frac{A}{F}\right|^2 = 1 + \frac{V_0^2}{4E(E+V_0)}\sin^2(2k'a)$$

T=1 pro

$$2k_n'a = n\pi$$

$$\lim_{E\to 0}\frac{1}{T} \sim 1 + \frac{V_0^2}{4EV_0}\sin^2(2k'a) \sim 1 + \frac{V_0}{4E}\sin^2(2\sqrt{2mV_0/h^2}\,a) \sim 1 + \frac{V_0}{4E}const \sim \infty$$

$$\lim_{E\to 0} T \sim 0$$

Efekt Ramsauera - Kr

Parametry jsou E, V_0 , a

$$\frac{1}{T} = \left|\frac{A}{F}\right|^2 = 1 + \frac{V_0^2}{4E(E+V_0)}\sin^2(2k'a)$$

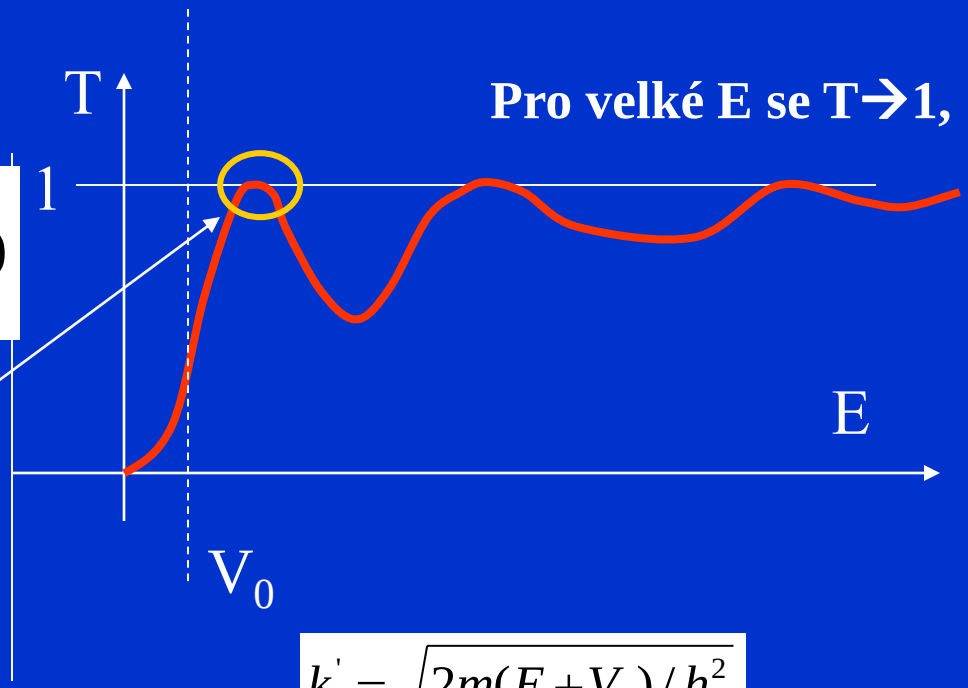

Pro velké E se T→1,

T=1 pro $2k_n'a = n\pi$

$$k' = \sqrt{2m(E+V_0)/h^2}$$

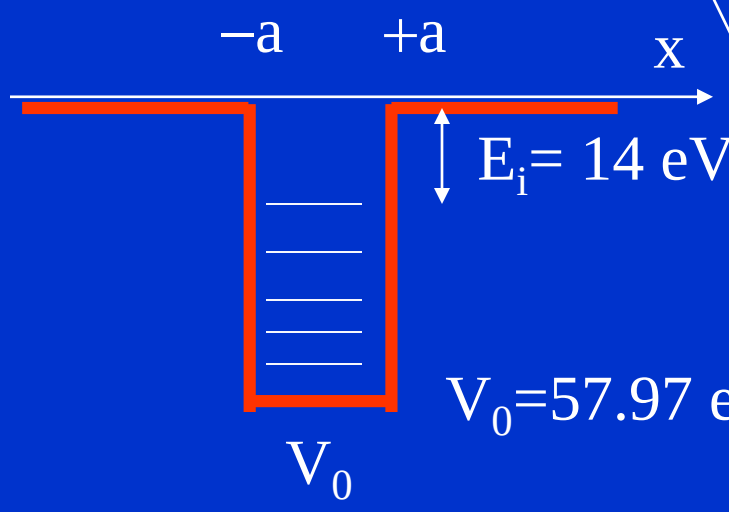

Kr; a=2Å

E_i= 14 eV ➔ V_0=57.97 eV

E=0.013 V_0=0.75 eV

Jednorozměrný rozptyl

Parametry jsou E, V_0 , a

T+R=1

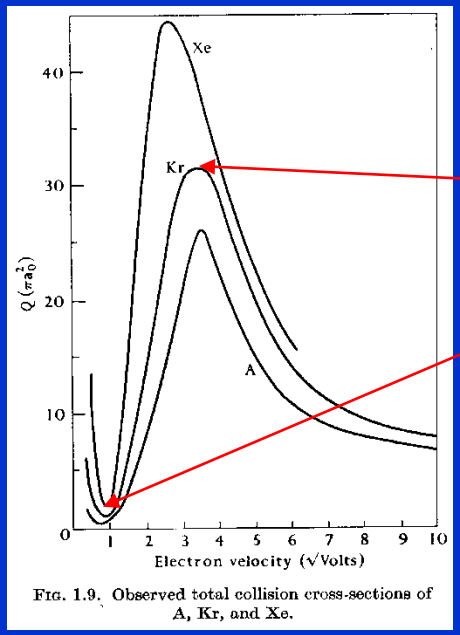

FIG. 1.9. Observed total collision cross-sections of A, Kr, and Xe.

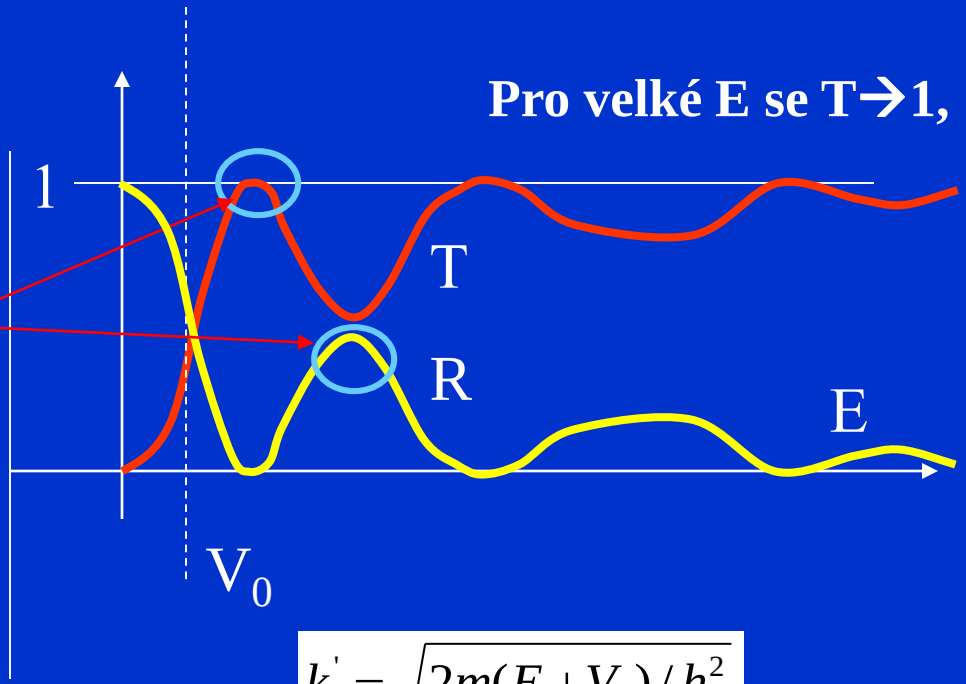

Pro velké E se T→1,

$$2k_n' a = n\pi$$

$$k' = \sqrt{2m(E+V_0)/h^2}$$

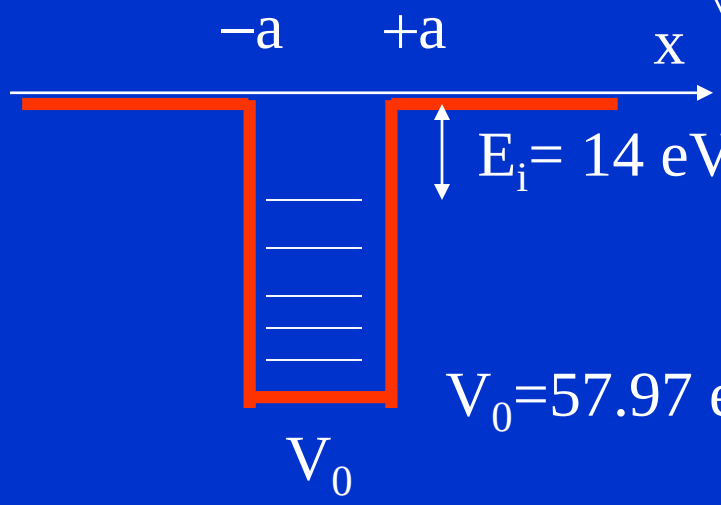

Kr; a=2Å

E_i= 14 eV ➔ V_0=57.97 eV

E=0.013 V_0=0.75 eV

Frequencies of elastic collisions

$\delta I = -NQI_p \delta x$

$I_P = I_0 \exp(-QNx)$

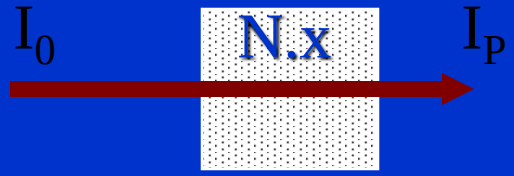

Q(v)

Collision Frequencies

$\nu \sim n v \sigma$

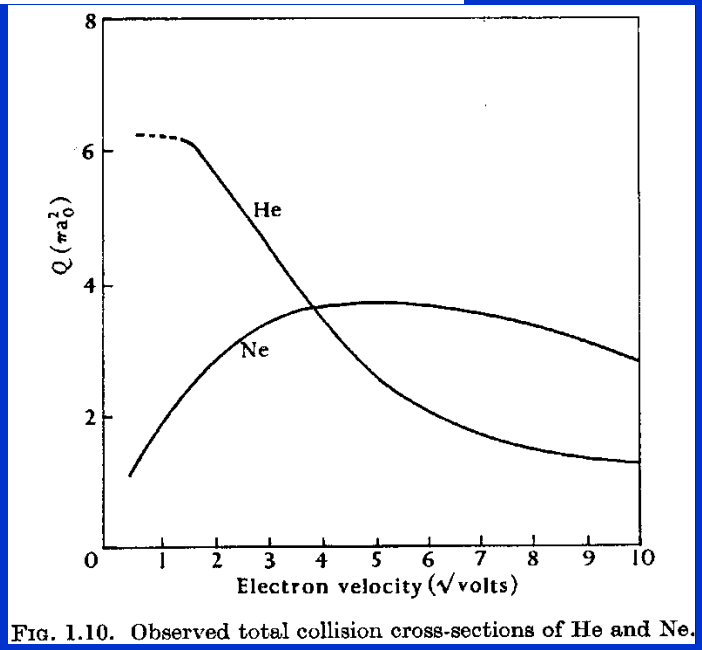

Fig. 1.10. Observed total collision cross-sections of He and Ne.

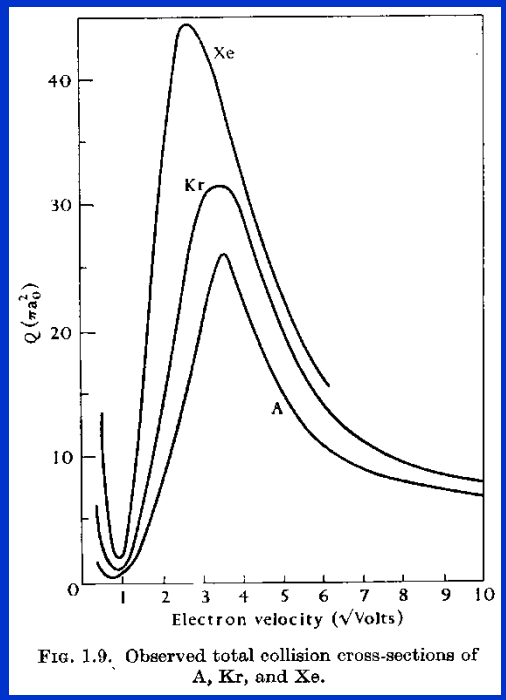

Fig. 1.9. Observed total collision cross-sections of A, Kr, and Xe.

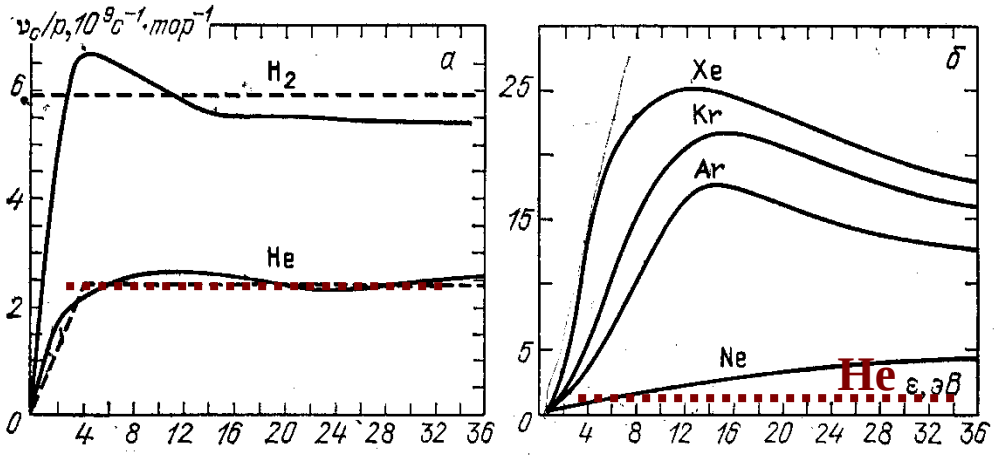

Рис. 2.5. Частоты упругих столкновений электронов, p=1 тор: *а* — в H_2 и He; *б* — в инертных газах; штриховые линии — удобная аппроксимация при расчетах [24]

$a_0 = 0.53 \times 10^{-8}$cm~0.5A

Radius of the first Bohr orbit of H atom

Very low collision energies

1995

TOPICAL REVIEW

Electron–molecule collisions at very low electron energies

F B Dunning

Department of Physics and the Rice Quantum Institute, Rice University, PO Box 1892, Houston, TX 77251, USA

J. Phys. B: At. Mol. Opt. Phys. 28 (1995) 1645–1672. Printed in the UK

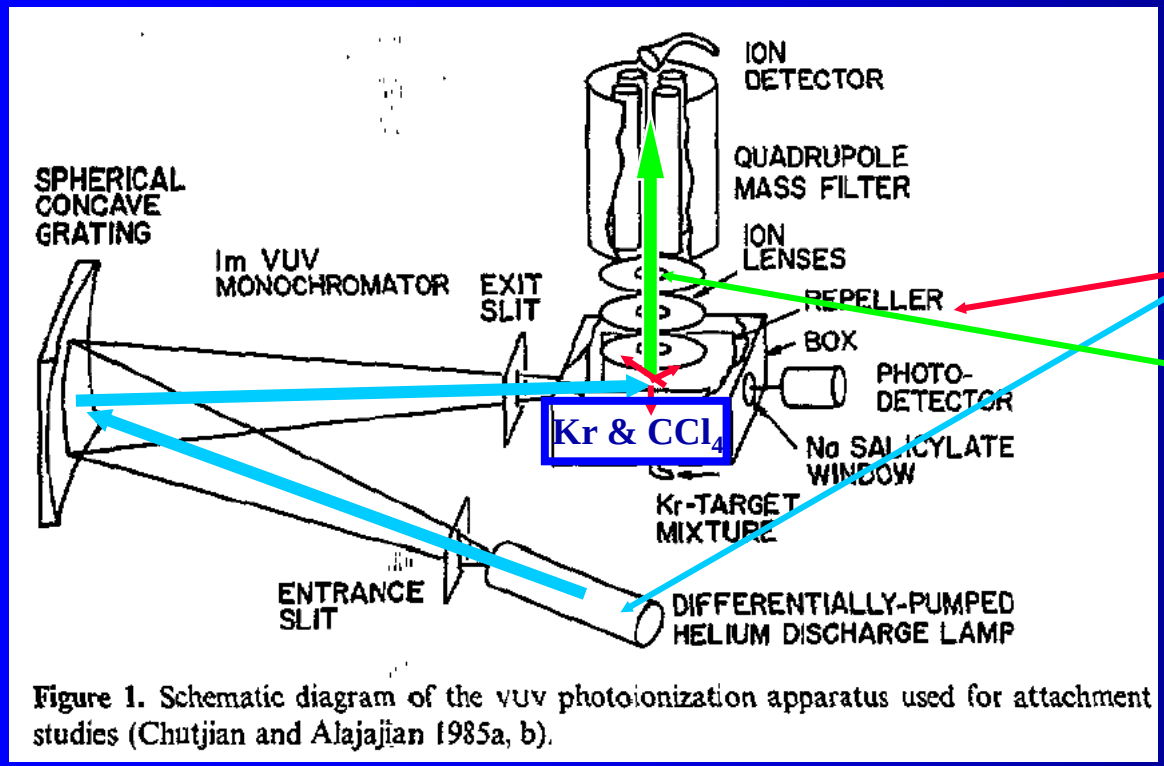

Figure 1. Schematic diagram of the VUV photoionization apparatus used for attachment studies (Chutjian and Alajajian 1985a, b).

$$Kr(^1S_0) + \hbar\omega \rightarrow Kr^+(^2P_{1/2}) + e^-(\varepsilon)$$

$$e^- + CCl_4 \rightarrow CCl_4^{-*} \rightarrow CCl_3 + Cl^-$$

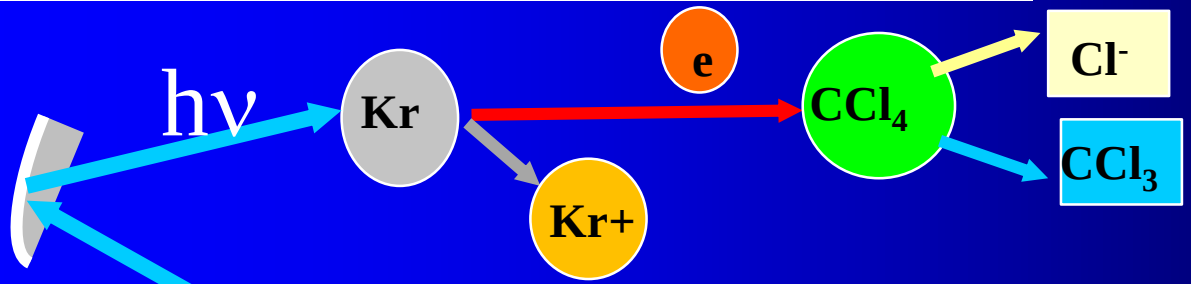

Very low collision energies

TOPICAL REVIEW

Electron–molecule collisions at very low electron energies

F B Dunning

Department of Physics and the Rice Quantum Institute, Rice University, PO Box 1892, Houston, TX 77251, USA

J. Phys. B: At. Mol. Opt. Phys. 28 (1995) 1645–1672. Printed in the UK

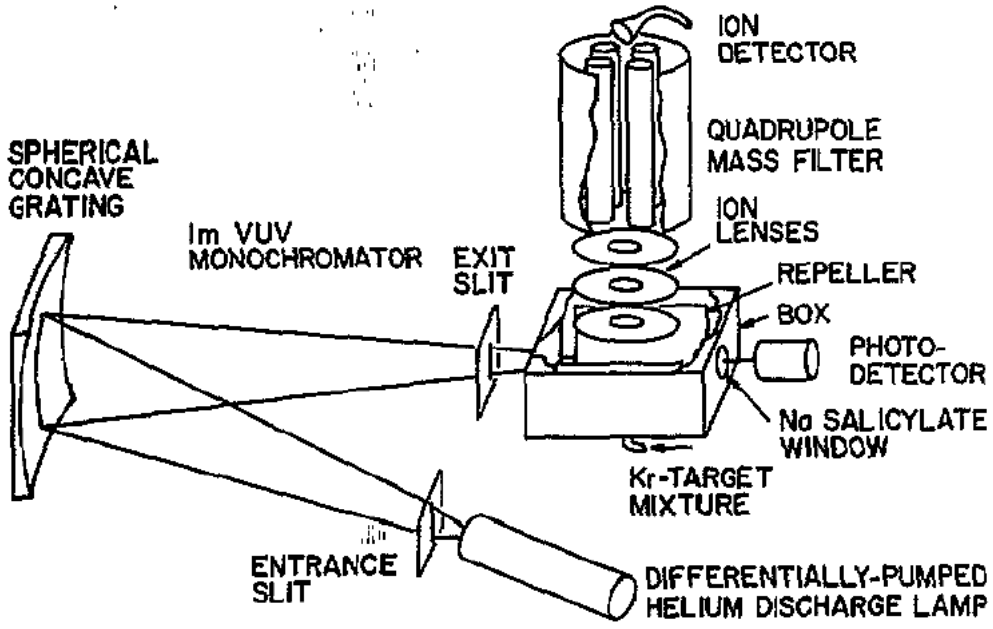

Figure 1. Schematic diagram of the VUV photoionization apparatus used for attachment studies (Chutjian and Alajajian 1985a, b).

$$Kr(^1S_0) + \hbar\omega \rightarrow Kr^+(^2P_{1/2}) + e^-(\varepsilon)$$

$$e^- + SF_6 \rightarrow SF_6^{-*}$$

$$e^- + CCl_4 \rightarrow CCl_4^{-*} \rightarrow CCl_3 + Cl^-$$

Very low collision energies

$$Kr(^1S_0) + \hbar\omega \rightarrow Kr^+(^2P_{1/2}) + e^-(\varepsilon)$$

$$e^- + SF_6 \rightarrow SF_6^{-*}$$

$$e^- + CCl_4 \rightarrow CCl_4^{-*} \rightarrow CCl_3 + Cl^-$$

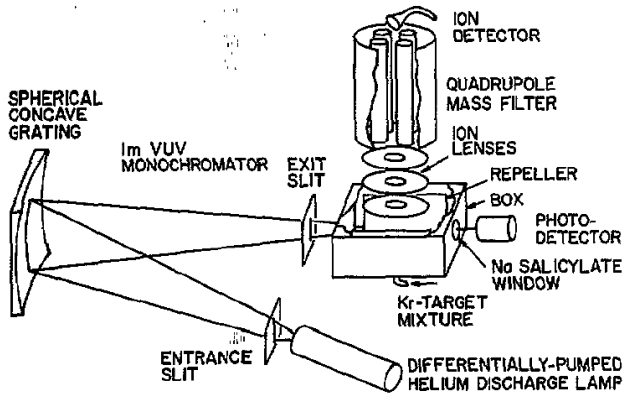

Figure 1. Schematic diagram of the VUV photoionization apparatus used for attachment studies (Chutjian and Alajajian 1985a, b).

TOPICAL REVIEW

J. Phys. B: At. Mol. Opt. Phys. 28 (1995) 1645–1672. Printed in the UK

Electron–molecule collisions at very low electron energies

F B Dunning

Department of Physics and the Rice Quantum Institute, Rice University, PO Box 1892, Houston, TX 77251, USA

10^5 $\mathring{A}^2$

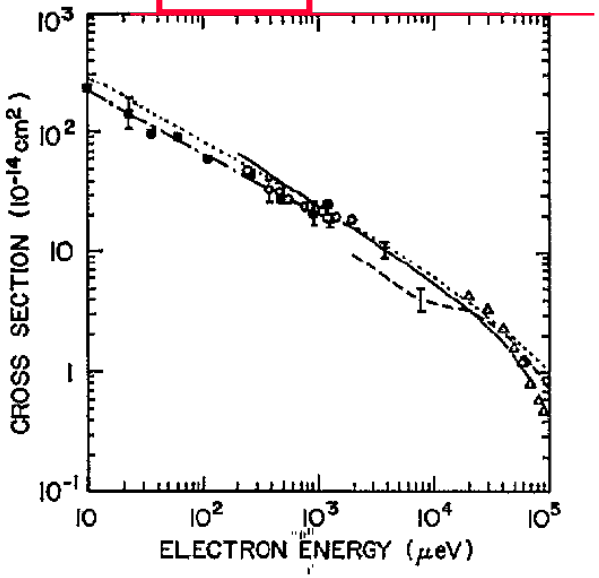

Figure 2. Cross section for electron attachment to SF_6. ■, $\bar{\sigma}_e$-K(np); — · —, $\sigma_e(v)$-K(np) (Ling *et al* 1992). ○, $\bar{\sigma}_e$-Rb(ns) (Zollars *et al* 1985); ——, free electrons (Klar *et al* 1992a, b); – – –, free electrons (Chutjian and Alajajian 1985); △, free electrons (Pai *et al* 1979, Chutjian and Alajajian 1985a); ----, theory (Klots 1976).

Electron attachment at very low electron energies

10^5 Å^2

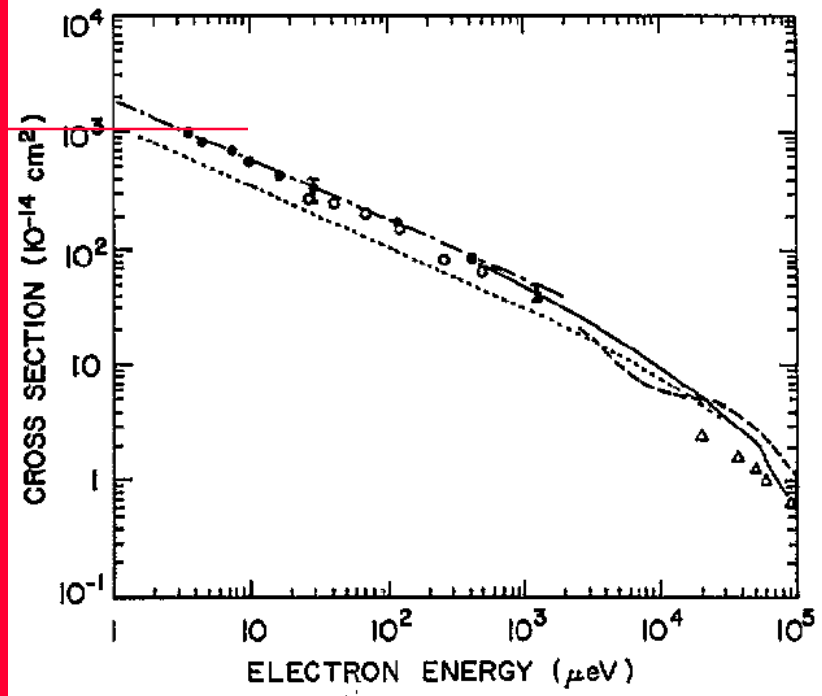

Figure 3. Cross sections for electron attachment to CCl_4. ●, $\bar{\sigma}_e$-K(np); —·—, $\sigma_e(v)$-K(np) (Frey *et al* 1994b); ○, $\bar{\sigma}_e$-K(np) (Ling *et al* 1992); ——, free electrons (Hotop 1994); – – –, free electrons (Orient *et al* 1989); △, free electrons (Christodoulides and Christophorou (1971); -----, theory (Klots 1976).

10^5 Å^2

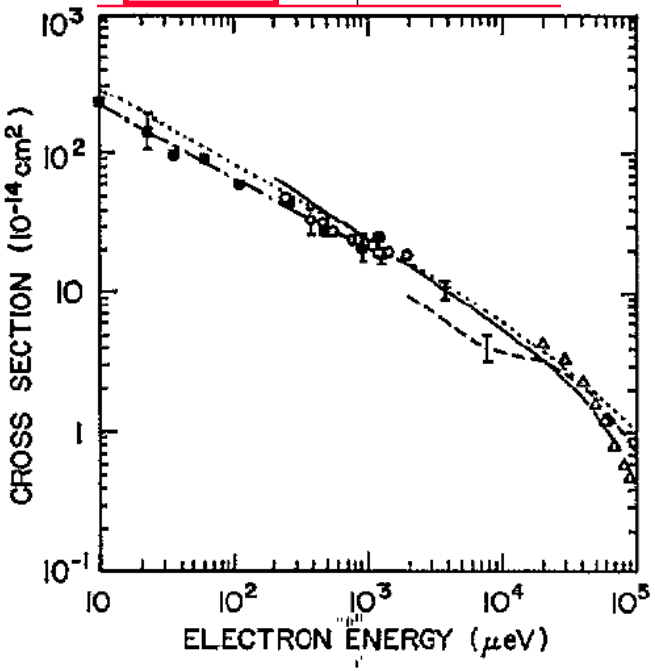

Figure 2. Cross section for electron attachment to SF_6. ■, $\bar{\sigma}_e$-K(np); —·—, $\sigma_e(v)$-K(np) (Ling *et al* 1992). ○, $\bar{\sigma}_e$-Rb(ns) (Zollars *et al* 1985); ——, free electrons (Klar *et al* 1992a, b); – – –, free electrons (Chutjian and Alajajian 1985); △, free electrons (Pai *et al* 1979, Chutjian and Alajajian 1985a); -----, theory (Klots 1976).

Molecules

2004

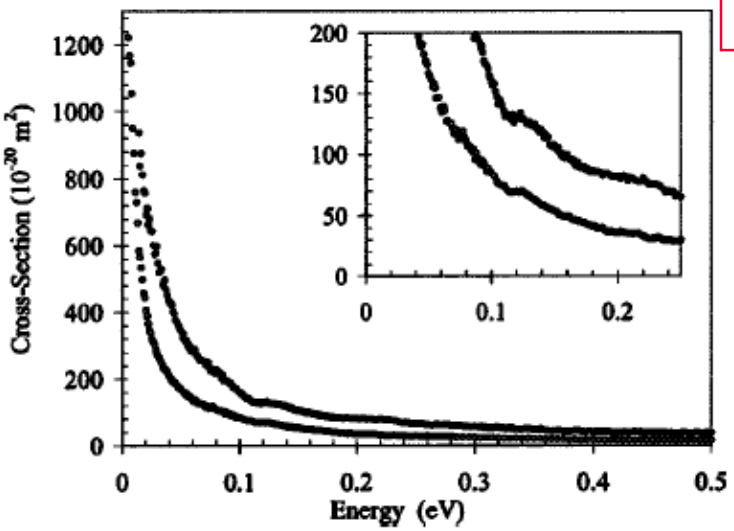

PHYSICAL REVIEW A 69, 052716 (2004)

Cold electron scattering in SF_6 and C_6F_6: Bound and virtual state channels

D. Field,[1,*] N. C. Jones,[1] and J.-P. Ziesel[2]
[1]*Department of Physics and Astronomy, University of Aarhus, DK- 8000 Aarhus C, Denmark*
[2]*Laboratoire Collisions Agrégats Réactivité (CNRS UMR5589), Université Paul Sabatier, 31062 Toulouse, France*
(Received 26 November 2003; published 20 May 2004)

The general process which we study involves electron attachment,

$$e^- + M \rightarrow M^{-*}, \quad M = SF_6, C_6F_6, \qquad (1)$$

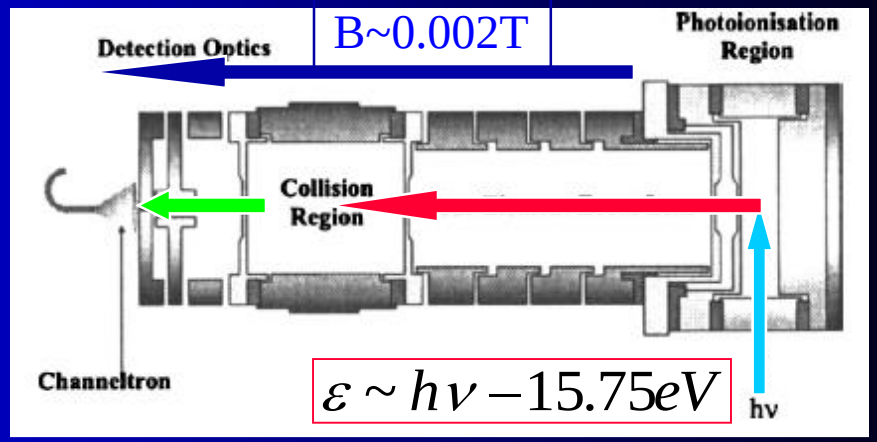

FIG. 1. A scale diagram of the apparatus. Monochromatic synchrotron radiation from ASTRID ($h\nu$) enters a photoionization region containing Ar. Photoelectrons, expelled by a weak electric field, are focused by a four-element lens [38] into a collision chamber containing the target gas. Transmitted electrons are detected at the channel electron multiplier (channeltron) situated beyond some further electron optics. The apparatus may be immersed in an axial magnetic field of 2×10^{-3} T.

B=0.002T

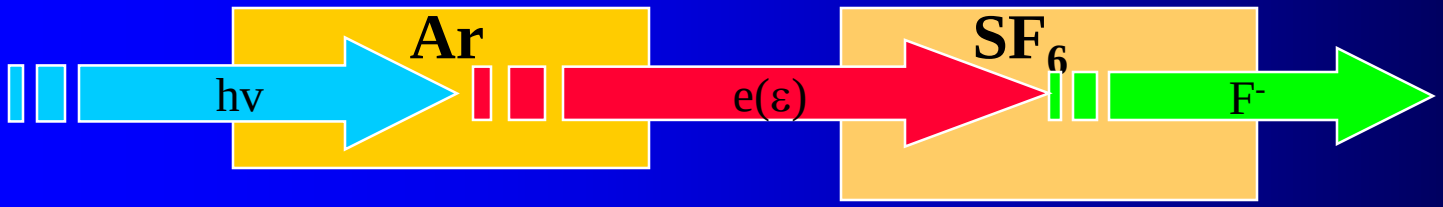

$Ar + h\nu \rightarrow Ar^+ + e(\varepsilon)$

$\varepsilon \sim h\nu - 15.75eV$

$SF_6 + e(\varepsilon) \rightarrow X^- + Y$

Molecules

2008

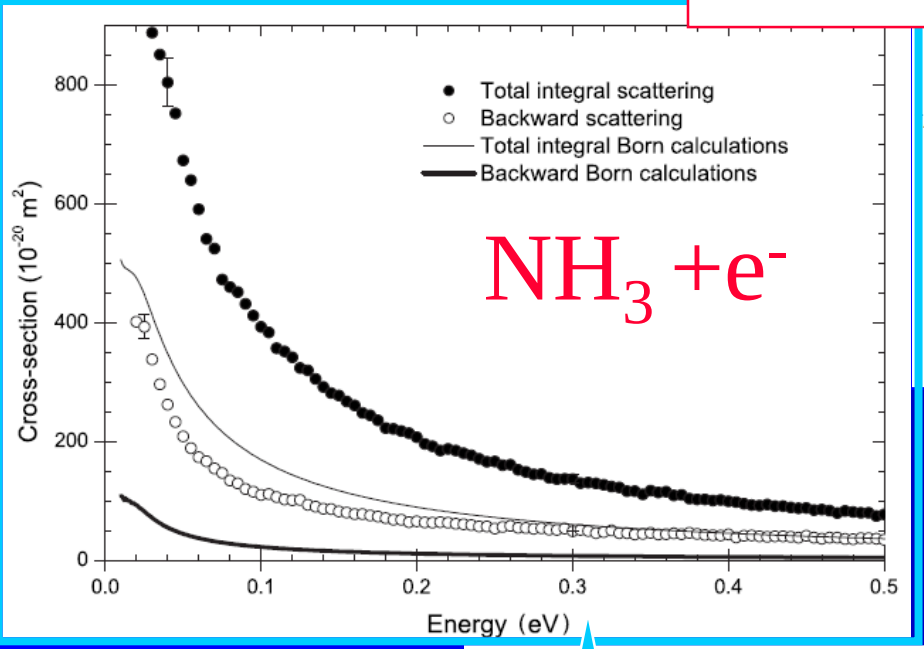

PHYSICAL REVIEW A **78**, 042714 (2008)

Scattering of cold electrons by ammonia, hydrogen sulfide, and carbonyl sulfide

N. C. Jones,[1] D. Field,[2,*] S. L. Lunt,[3] and J.-P. Ziesel[4]
[1]*Institute for Storage Ring Facilities (ISA), University of Aarhus, DK-8000 Aarhus C, Denmark*
[2]*Department of Physics and Astronomy, University of Aarhus, DK-8000 Aarhus C, Denmark*
[3]*Kittiwake Developments Ltd, Littlehampton, West Sussex BN17 7LU, United Kingdom*
Laboratoire Collisions Agrégats Réactivité (CNRS-UPS UMR5589), Université Paul Sabatier, 31062 Toulouse, France
(Received 2 July 2008; published 29 October 2008)

Experimental data obtained with a high-resolution transmission experiment are presented for the scattering of electrons in the energy range 20 meV–10 eV for NH_3, 25 meV–10 eV for H_2S, and 15 meV–2.5 eV for OCS. Data include cross sections for both integral scattering and scattering into the backward hemisphere, the latter up to 650 meV impact energy, with an electron energy resolution of between 1.6 and 3.5 meV. The new data allow the first detailed comparison with theory for the energy regime dominated by rotationally inelastic and elastic scattering for these species. It is evident that theory still lacks quantitative predictive power at low energy, although qualitative agreement is consistently good for all three species. A discussion is given of the possible presence of a virtual state in OCS scattering as recently proposed on theoretical grounds.

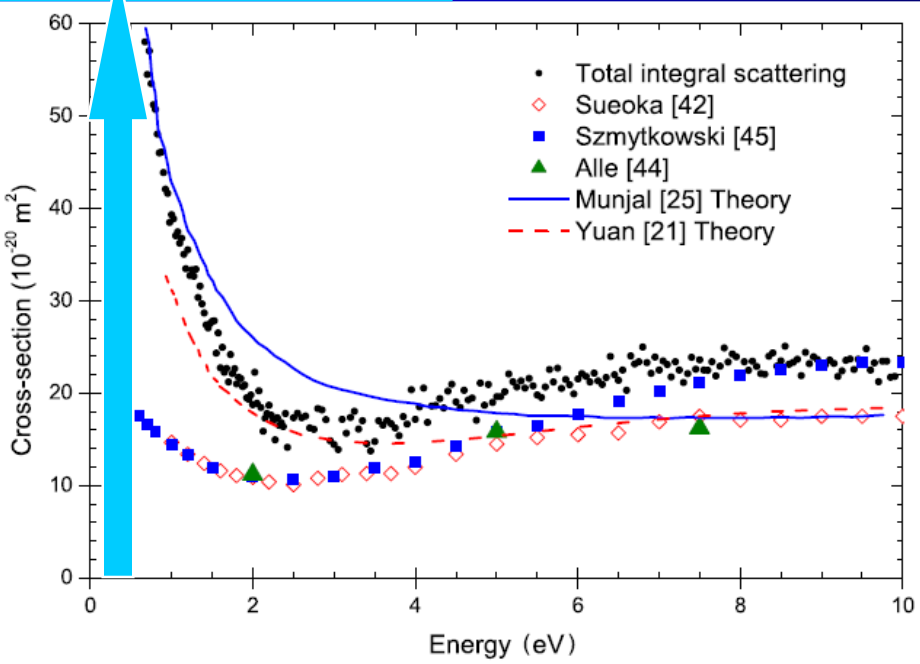

$NH_3 + e^-$

FIG. 1. (Color online) NH_3: the variation of the sum of the integral elastic and inelastic cross sections, $\sigma_{T,I}$, between 0.675 and 10 eV. Also shown are experimental data from Sueoka *et al.* [42], Szmytkowski *et al.* [45], and Alle *et al.* [44] and theoretical values from Munjal *et al.* [25] and Yuan *et al.* [21].

Molecules cross section for interaction with electrons

2008

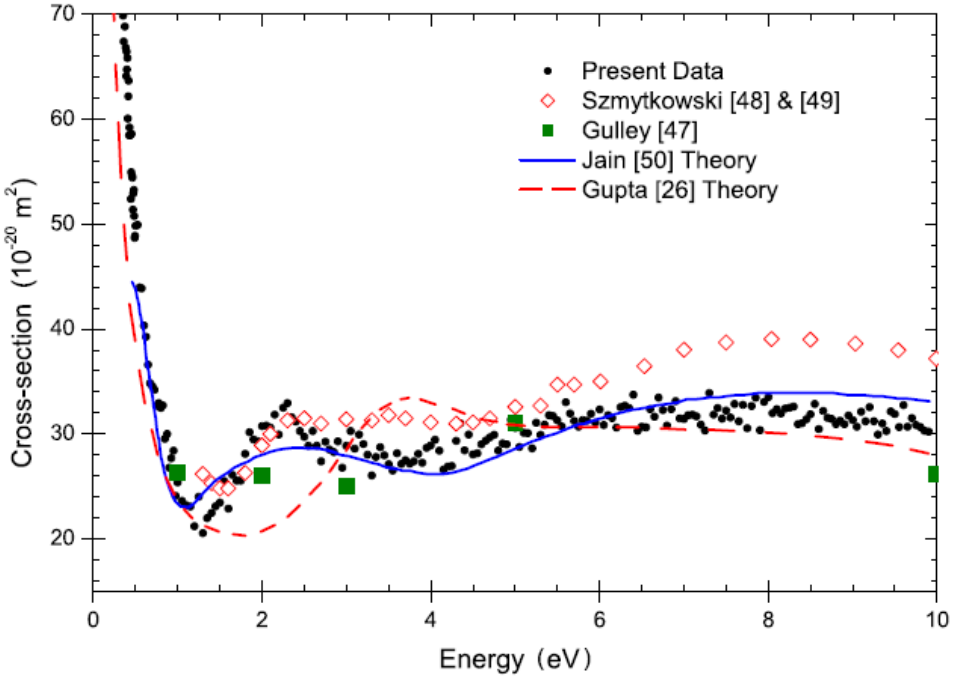

$H_2S + e^-$

FIG. 3. (Color online) H_2S: the variation of the sum of the integral elastic and inelastic cross sections, $\sigma_{T,I}$, between 380 meV and 10 eV. Also shown are experimental data in Szmytowski *et al.* [48,49] and Gulley *et al.* [47] and theoretical values from Jain *et al.* [50] and Gupta *et al.* [26].

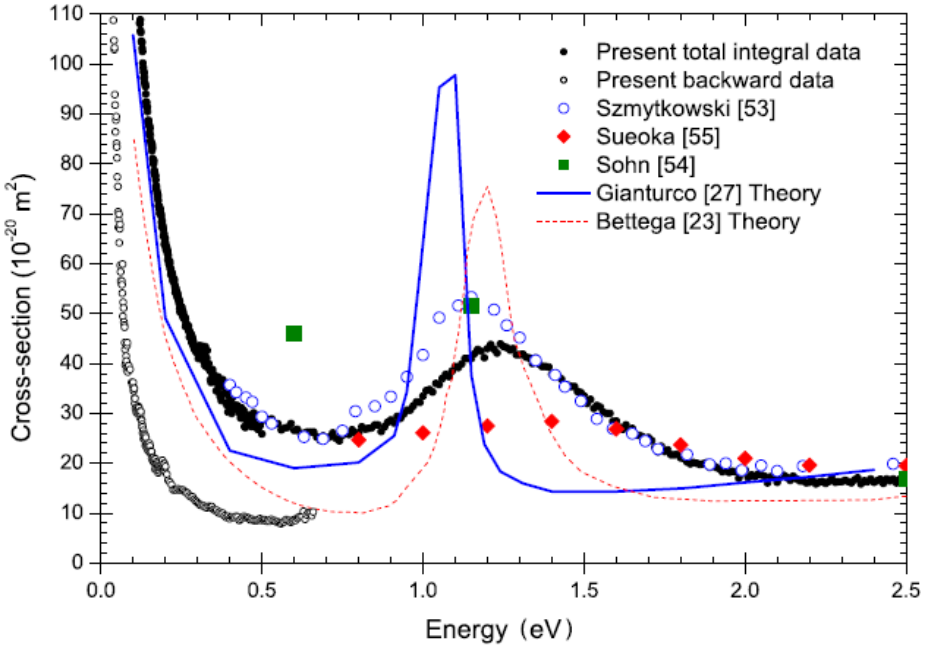

$OCS + e^-$

FIG. 5. (Color online) OCS: the variation of the sum of the integral elastic and inelastic cross sections, $\sigma_{T,I}$, between 120 meV and 2.5 eV, and the elastic and inelastic backward scattering cross section into the backward 2π sr, between 39 and 650 meV. Also shown are experimental values from Szymtkowski *et al.* [53], Sueoka *et al.* [55], and Sohn *et al.* [54] and theoretical values of integral cross sections from Gianturco *et al.* [27] and Bettega *et al.* [23].

Molecules

2006

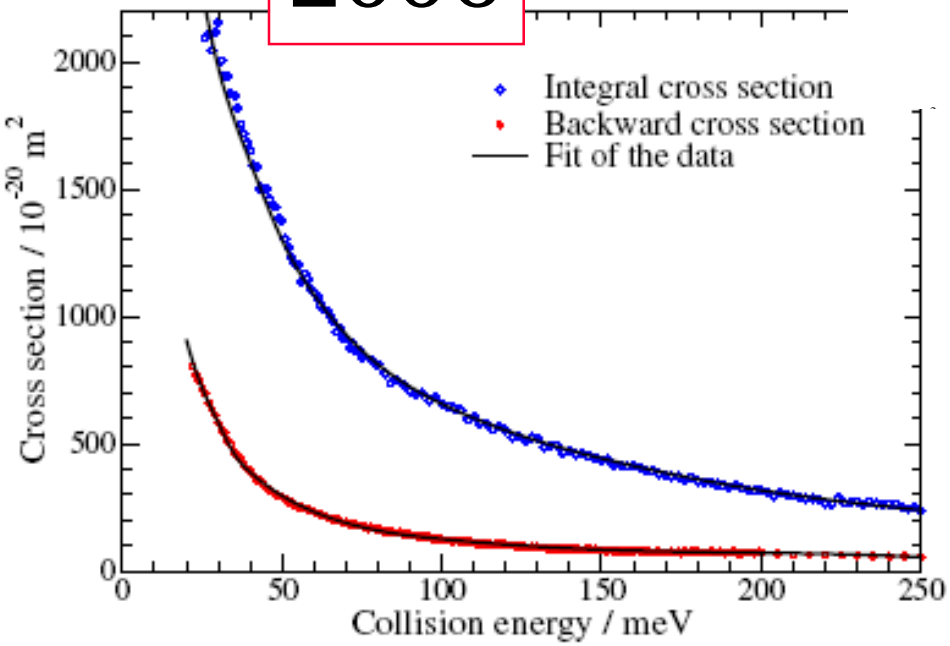

PRL 97, 123202 (2006) PHYSICAL REVIEW LETTERS week ending 22 SEPTEMBER 2006

Rotational Excitation of H_2O by Cold Electrons

R. Čurík,[1] J. P. Ziesel,[2] N. C. Jones,[3] T. A. Field,[4] and D. Field[3,*]
[1]*J. Heyrovský Institute of Physical Chemistry, Dolejškova 3, 18223 Prague 8, Czech Republic*

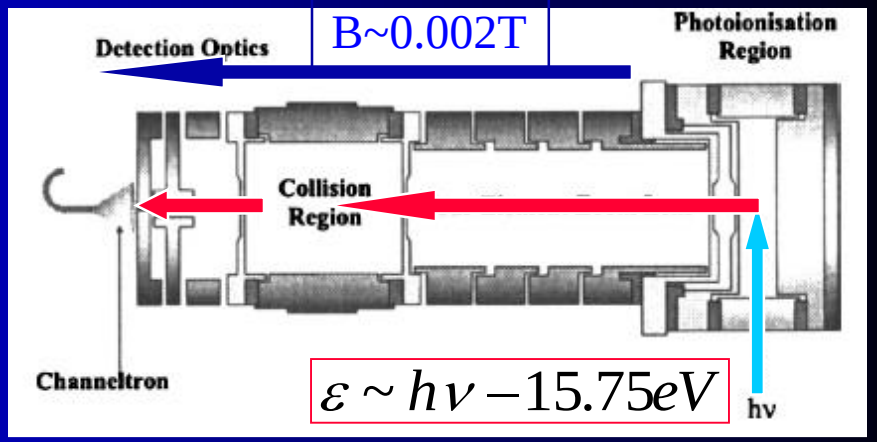

Experimental data are presented for the scattering of electrons by H_2O between 17 and 250 meV impact energy. These results are used in conjunction with a generally applicable method, based on a quantum defect theory approach to electron-polar molecule collisions, to derive the first set of data for state-to-state rotationally inelastic scattering cross sections based on experimental values.

B=2x10^{-3}T

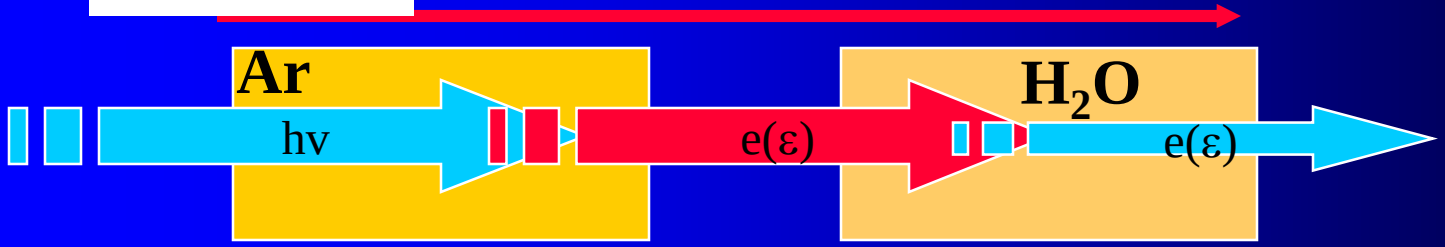

Ar +hν➔Ar$^+$+e(ε)

$\varepsilon \sim h\nu - 15.75eV$

H_2O (j_0) + e(ε_1)➔ H_2O($j>j_0$) + e(ε_2)

Molecules

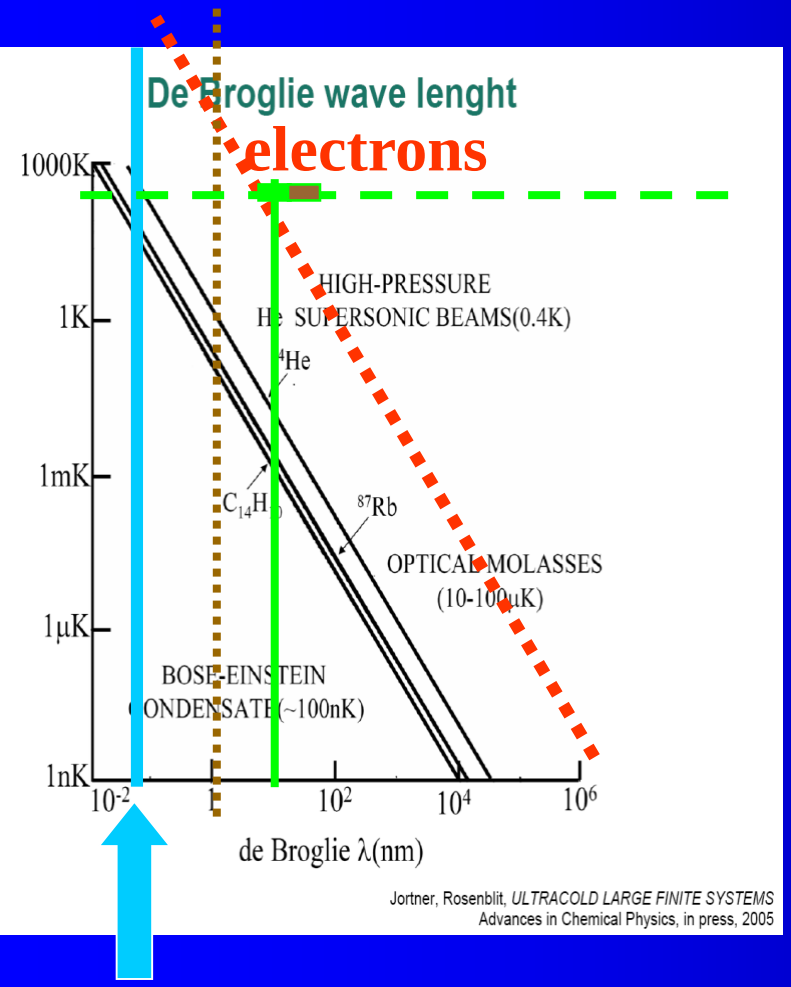

Jortner, Rosenblit, *ULTRACOLD LARGE FINITE SYSTEMS*
Advances in Chemical Physics, in press, 2005

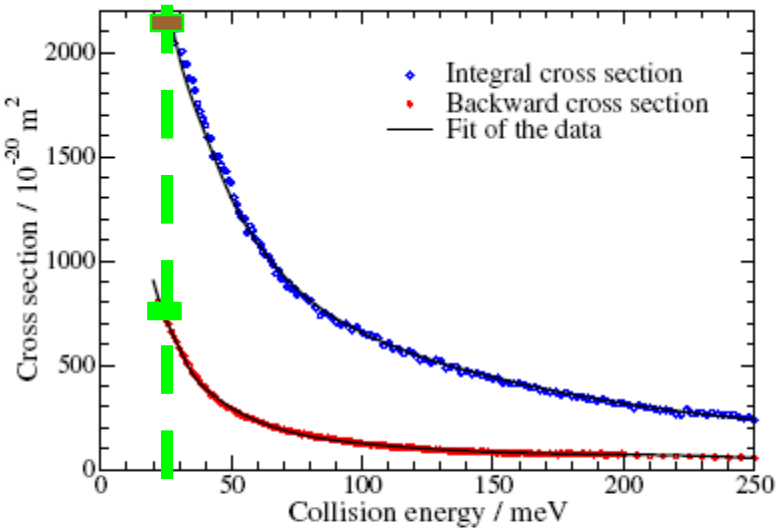

FIG. 1 (color online). Integral (upper set) and backward cross sections (lower set) for scattering of electrons by H_2O as a function of electron impact energy. Values are ±5%. The solid lines are fits to theory (see text).

$$\lambda = \frac{h}{p} = \frac{h}{mv}\sqrt{1 - \frac{v^2}{c^2}}$$

$$\sigma \sim \pi\lambda^2 \sim 1/\varepsilon$$

Molecules -rotational excitation

2006

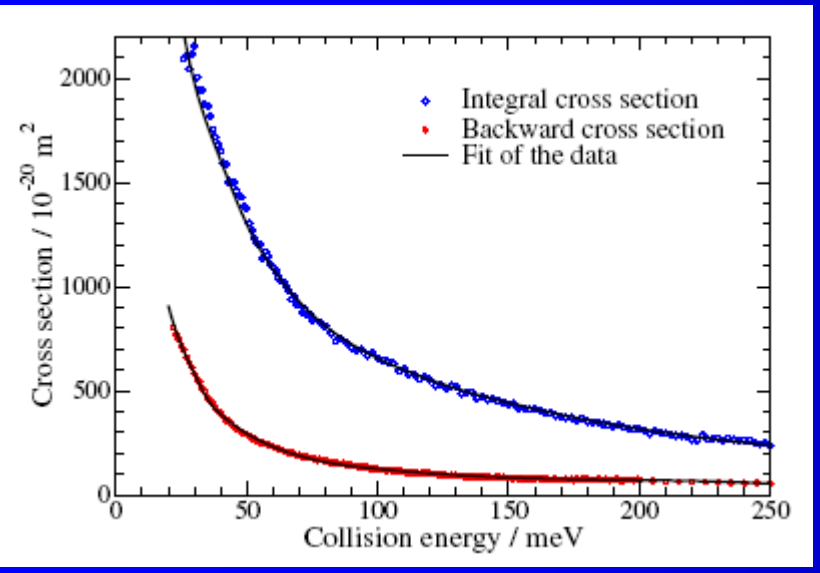

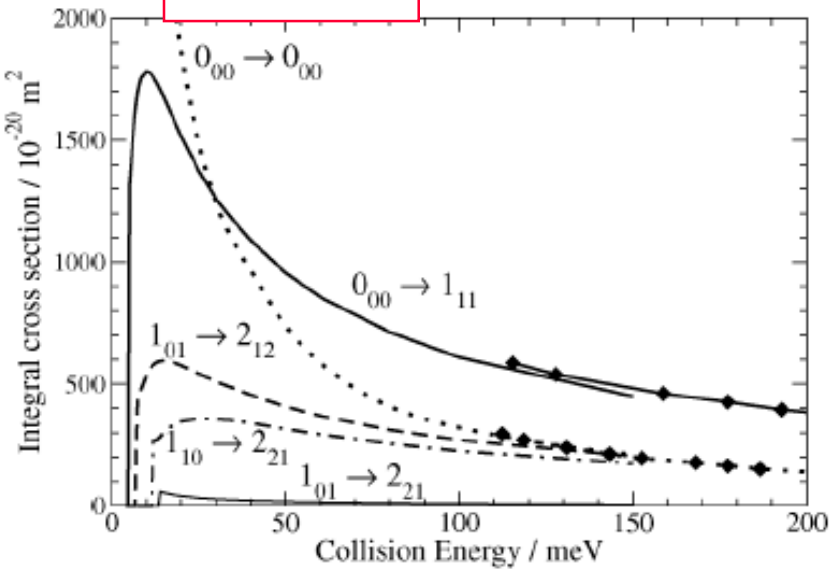

FIG. 3. Selected state-to-state integral cross sections for rotational excitation of the H_2O molecule determined from experimental data. Full curves represent results for para-H_2O and dashed for ortho-H_2O. The dotted curve represents elastic scattering for para-H_2O in its lowest rotational state. Curves with diamonds show the results of *R*-matrix calculations in Ref. [12].

$H_2O\ (j_0) + e(\varepsilon_1) \rightarrow H_2O(j>j_0) + e(\varepsilon_2)$

End of story 25 10 2024

Collisions of electrons with atoms

Classical or quantum approach?

Electron:

1eV → $v=5.9\times10^{7}$cm s^{-1}

$\tau\sim a_0/v \sim 10^{-8}/ 5.9\times10^{7}=2\times10^{-16}$s

$\lambda\sim 2A = 2\times10^{-8}$cm de Broglie

Ar+:

1eV → $v=2\times10^{5}$cm s^{-1}

$\tau\sim a_0/v \sim 10^{-8}/ 2\times10^{5}\sim 6\times10^{-14}$s

$\lambda\sim 9\times10^{-11}$cm de Broglie

H_3^* + e at 10 K ????

$$\lambda_e(4K) \sim 540\,A \sim 54x10^{-9}\,m$$

Rydberg atom

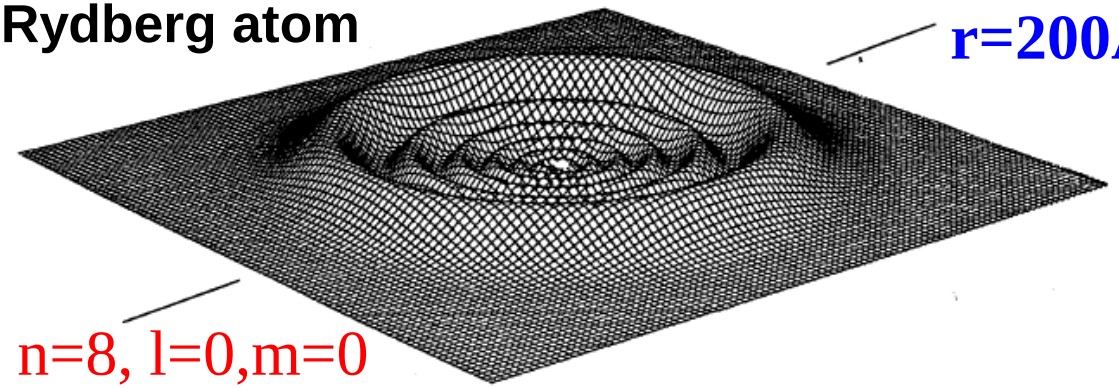

Low energy collisions of electrons with molecules

De Broglie wave length

$$\lambda = \frac{h}{p} = \frac{h}{mv}\sqrt{1 - \frac{v^2}{c^2}}$$

$$\lambda_e(4K) \sim 540\,A \sim 54x10^{-9}\,m$$

$$\lambda_e(1eV) \sim 11.6\,A \sim 1.16x10^{-9}\,m$$

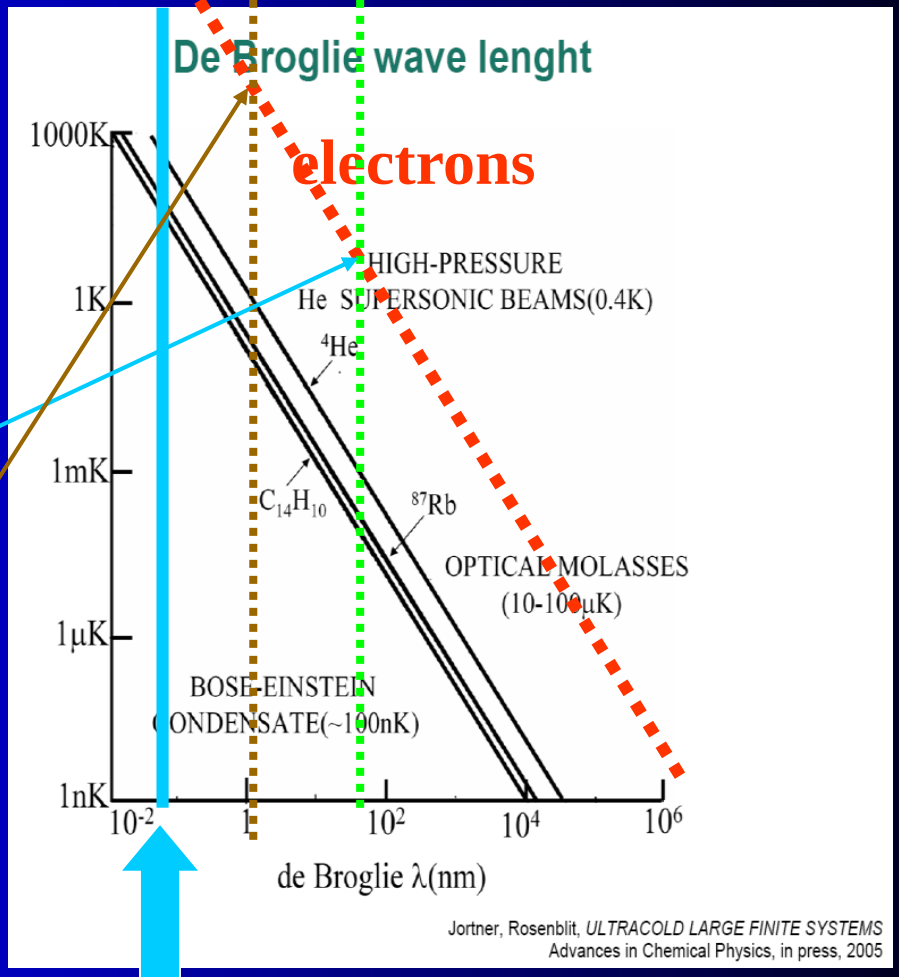

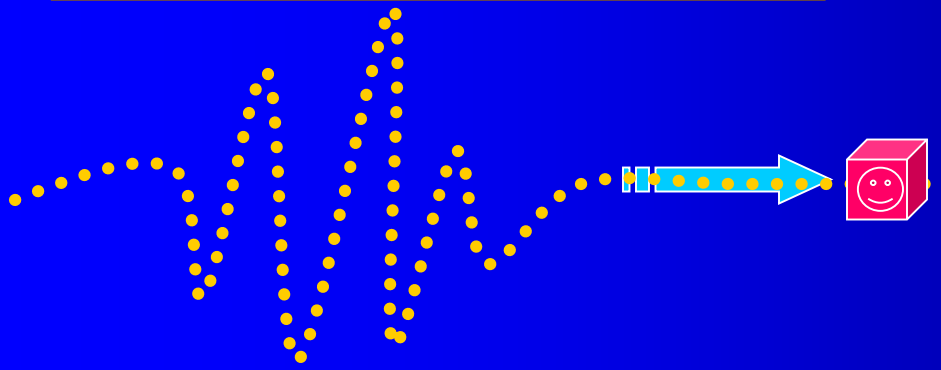

a_0

Cross section

$$A^+ + B \rightarrow C^+ + D$$

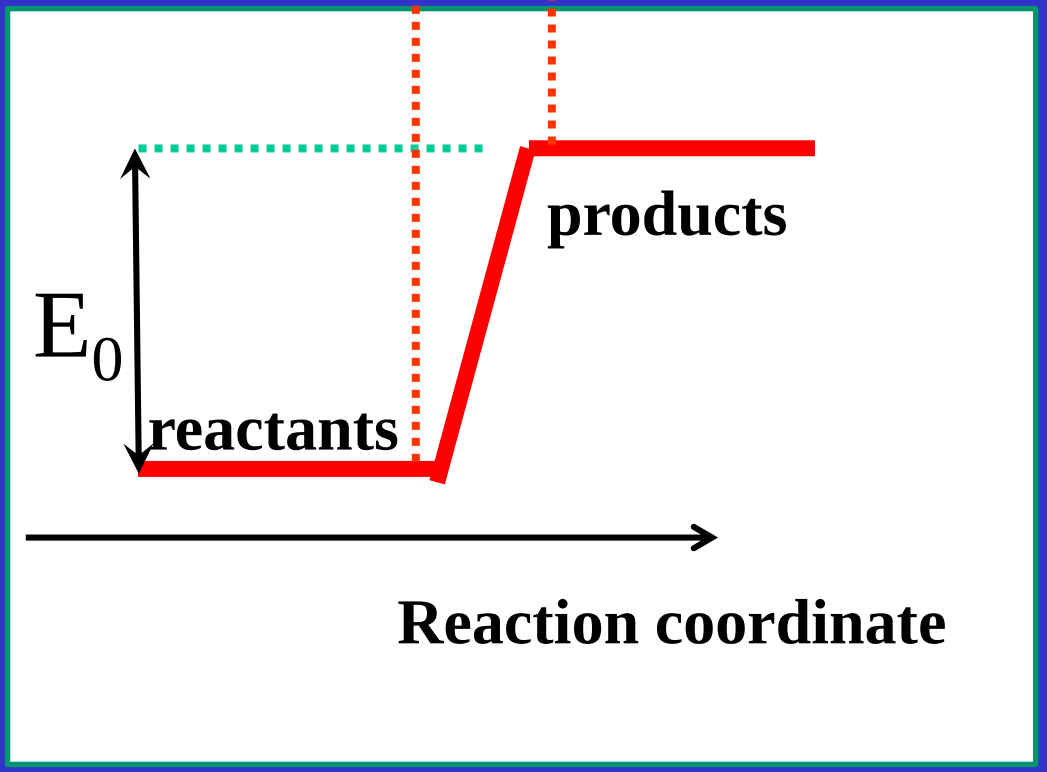

Reaction cross section

Collisional cross section

$H_2^+ + Ar \Rightarrow ArH^+ + H$

Single collision

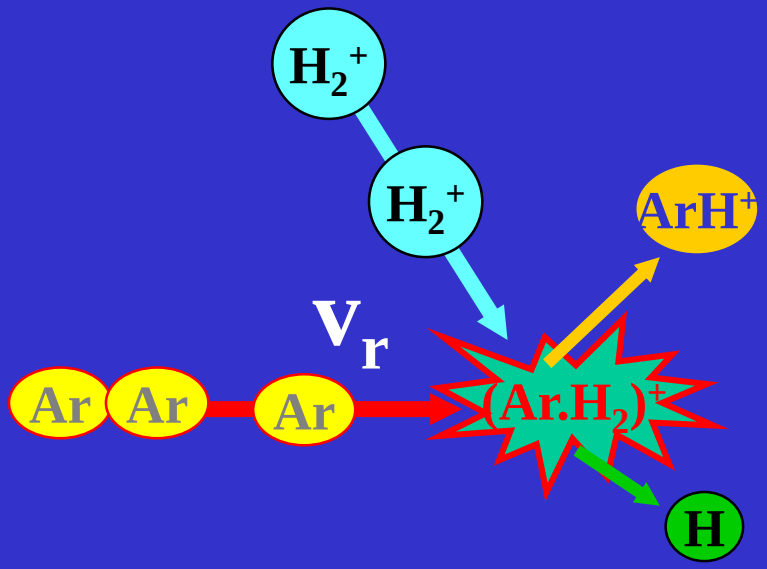

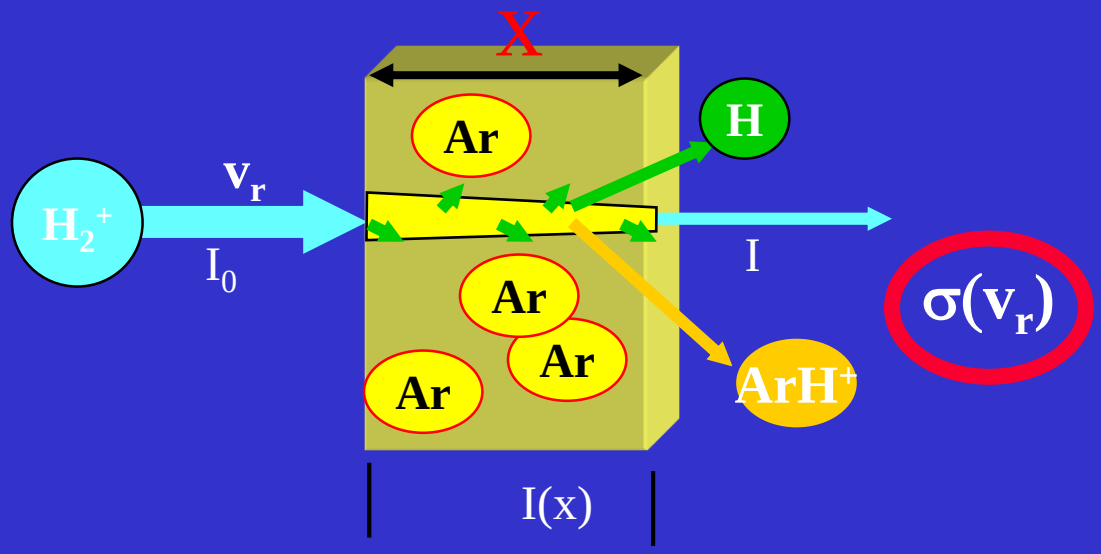

Reaction cross section

Collisional cross section

$$I = I_0 \exp(-\sigma n_{Ar} x)$$

Single collision

$$H_2^+ + Ar \Rightarrow ArH^+ + H$$

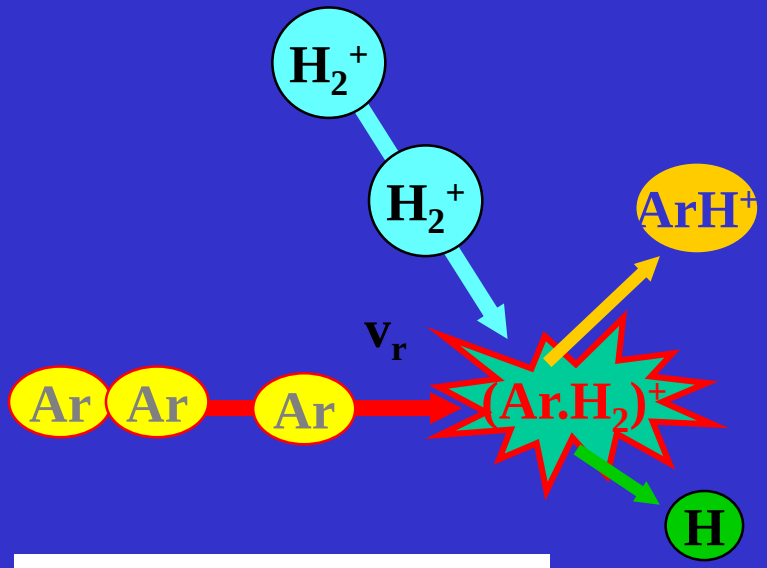

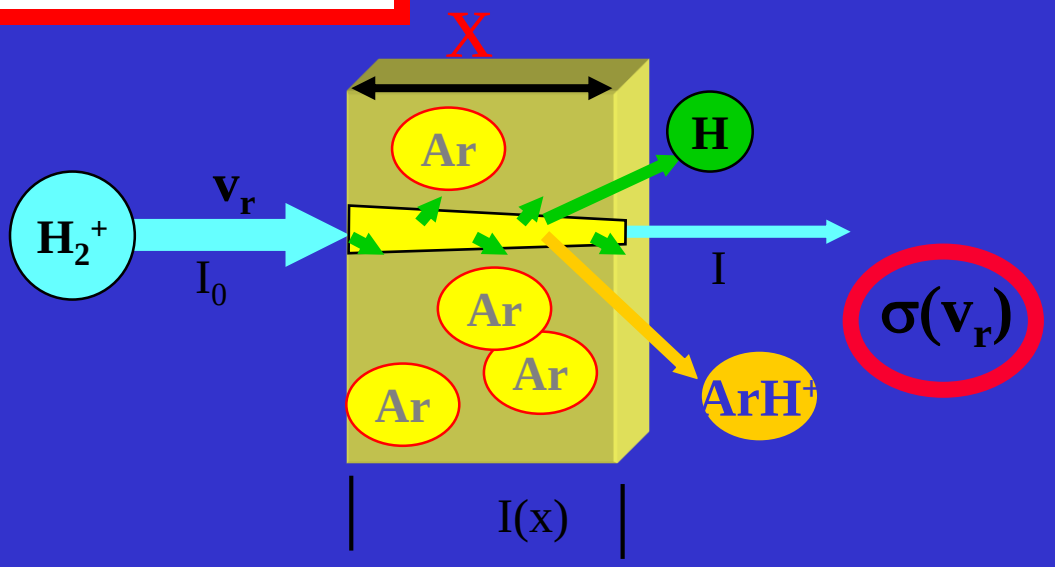

reaction cross section

$$I = I_0 \exp(-\sigma n_{Ar} x)$$

$$\nu_{coll} = +nV_{rel} = +n\nu S = +n\nu\pi\delta^2 = +n\nu\sigma$$

Collisional cross section

$$\frac{dI}{dt} = -\frac{I}{\tau_{coll}} = -I\nu_{coll}$$

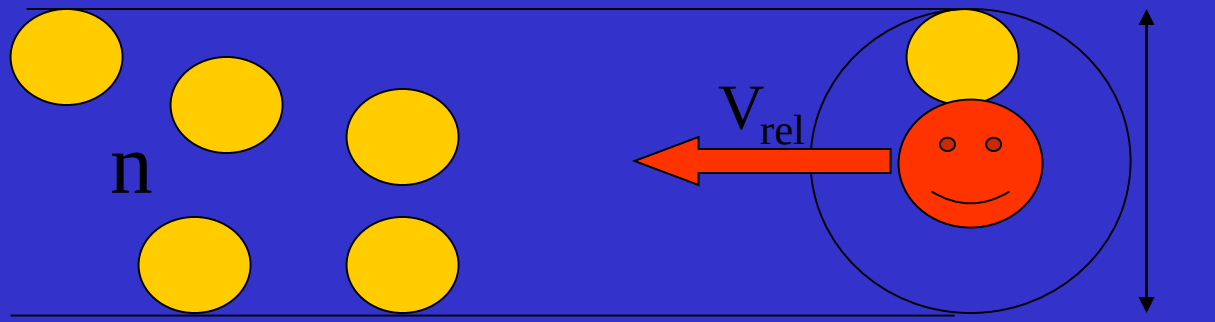

$$I(t) = I_0 \exp(-\nu_{coll} t) = I_0 \exp(-\sigma n \nu_{rel} t)$$

$$I = I_0 \exp(-\sigma n_{Ar} x)$$

Single collision

$$H_2^+ + Ar \Rightarrow ArH^+ + H$$

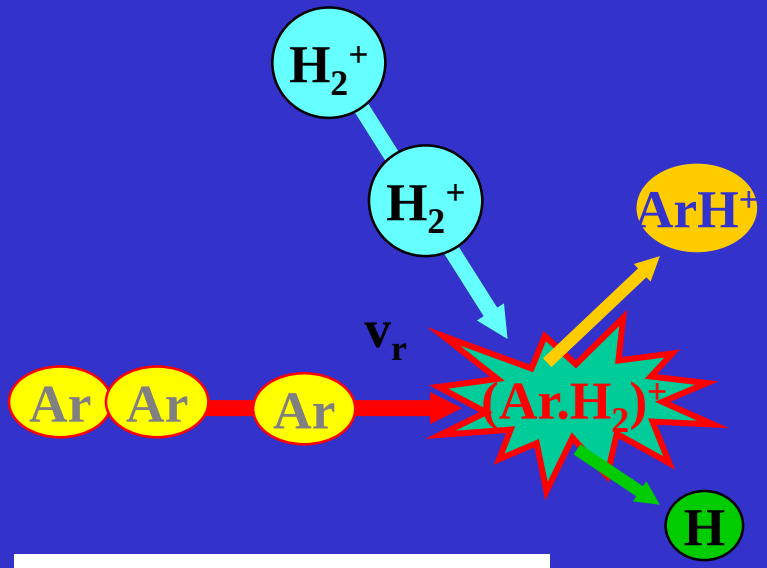

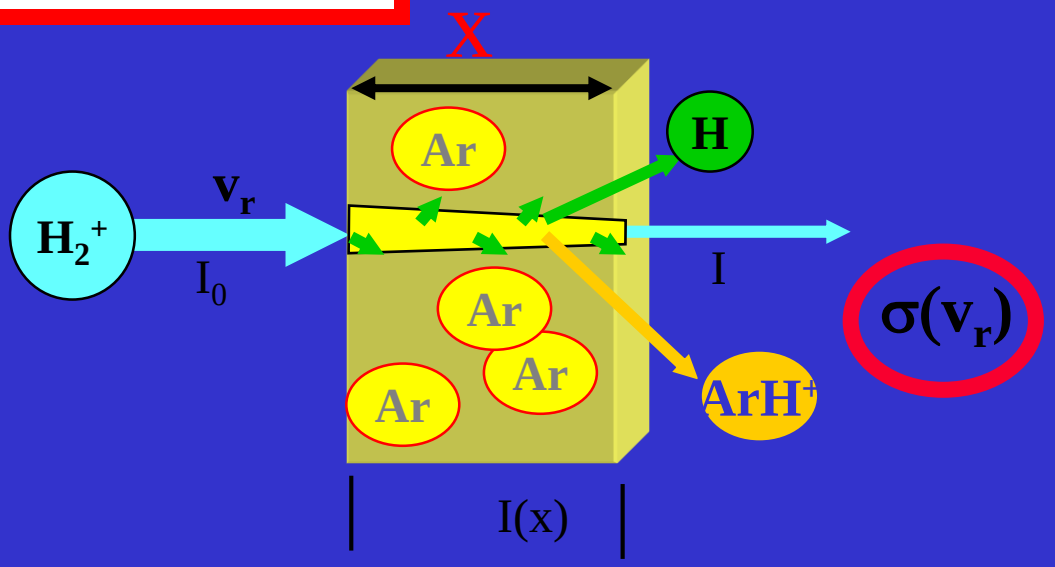

reaction cross section

$I=I_0\exp(-\sigma n_{Ar} x)$

Proportionality factor

$$\frac{dI}{dx} \sim -INx \qquad \frac{dI}{dx} = -\sigma INx$$

$$\frac{dI}{Idx} = \frac{d\ln(I)}{dx} = -\sigma Nx$$

$$I(x) = I_0 \exp(-\sigma Nx)$$

Impact ionization

2.3. Electron impact ionization

The electron impact ionization is the most fundamental ionization process for the operation of ion sources.

Why?

- The cross section for the impact ionization is by orders of magnitudes higher than the cross section for the photo ionization.
- The cross section depends on the mass of the colliding particle. Since the energy transfer of a heavy particle is lower, a proton needs for an identical ionization probability an ionization energy three orders of magnitudes higher than an electron

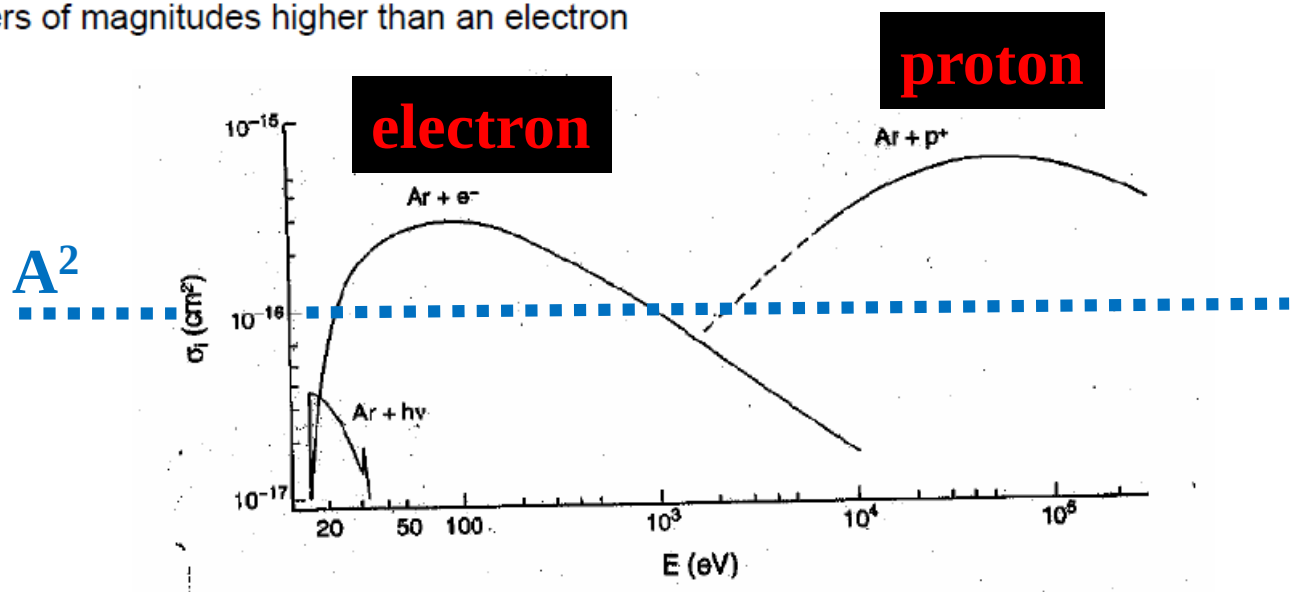

FIGURE 4
Ionization cross sections as functions of energy for ionizing collisions with fast electrons, protons, and photons. (From Winter, H., in *Experimental Methods in Heavy Ion Physics*, Springer-Verlag,

Cross sections for vibrational excitation, dissociation, ionization…H_2

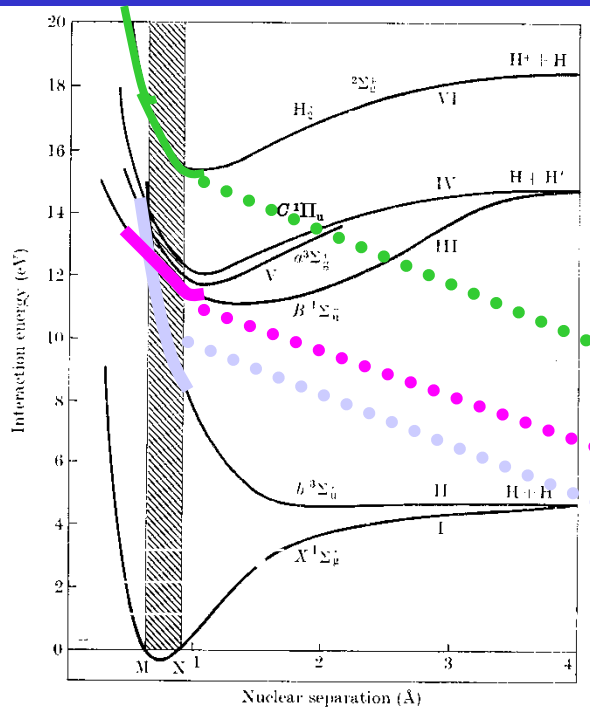

FIG. 13.1. Potential energy curves for electronic states of H_2 and H_2^+ lying within 20 eV of the ground state.

$H_2(v) + e$	Vibrational excitation
$H + H + e$	Dissociation
$H_2^* + h\nu + e$	Photon excitation
$H_2^+ + e + e$	Ionization
$H^+ + H + e + e$	Dissociative Ionization

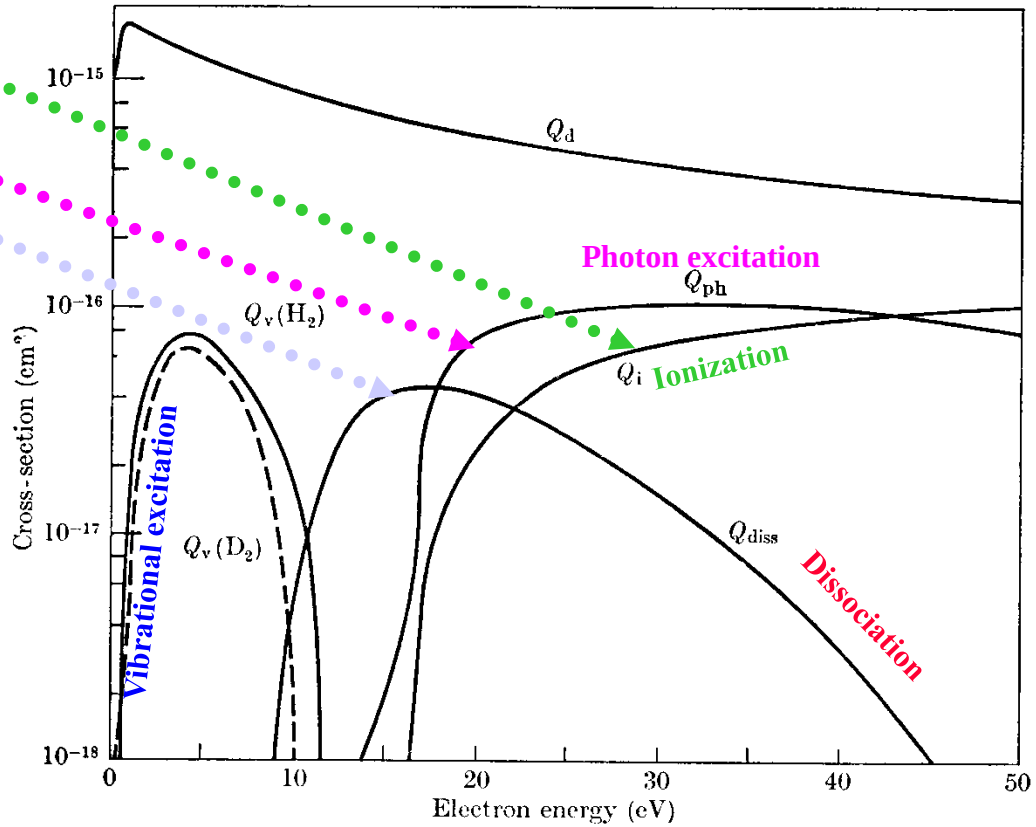

FIG. 13.37. Cross-sections assumed by Engelhardt and Phelps in their analysis of swarm data in H_2 and D_2 for electrons of characteristic energy greater than 1 eV. Q_d momentum-transfer cross-section, Q_i, ionization cross-section, Q_{diss} dissociation cross-section, Q_{ph} photon excitation cross-section, Q_v vibrational excitation cross-section (—— H_2, — — — D_2).

Cross sections for vibrational excitation, dissociation, ionization…H_2

$H_2(v) + e$	Vibrational excitation
$H + H + e$	Dissociation
$H_2^* + h\nu + e$	Photon excitation
$H_2^+ + e + e$	Ionization
$H^+ + H + e + e$	Dissociative Ionization

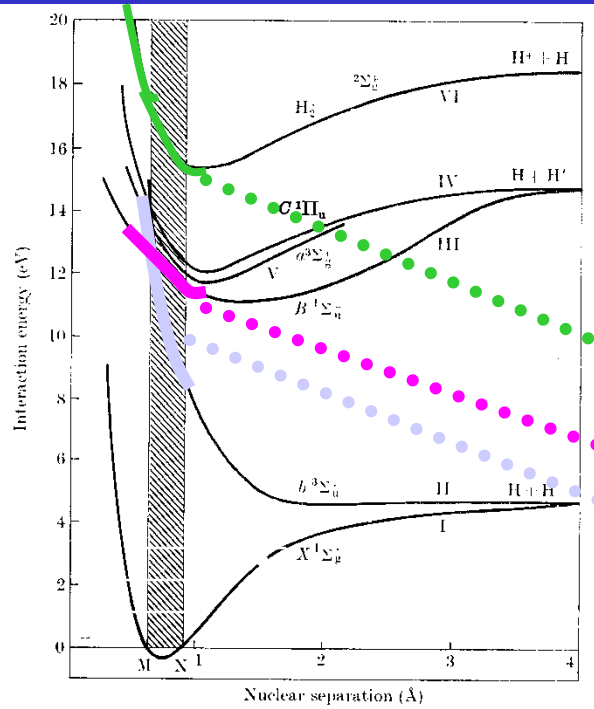

FIG. 13.1. Potential energy curves for electronic states of H_2 and H_2^+ lying within 20 eV of the ground state.

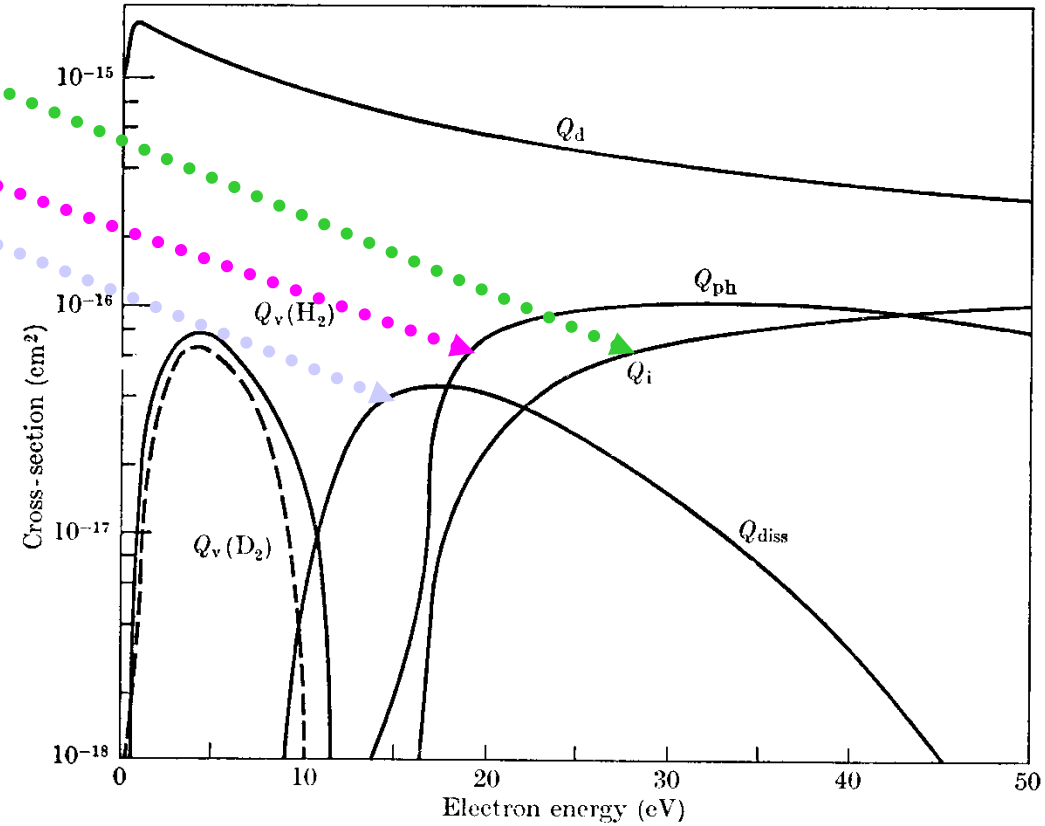

FIG. 13.37. Cross-sections assumed by Engelhardt and Phelps in their analysis of swarm data in H_2 and D_2 for electrons of characteristic energy greater than 1 eV. Q_d momentum-transfer cross-section, Q_i, ionization cross-section, Q_{diss} dissociation cross-section, Q_{ph} photon excitation cross-section, Q_v vibrational excitation cross-section (—— H_2, ——— D_2).

Debye shielding Linear

$$n_e = n_\infty \exp(eV / kT_e)$$

$$\nabla^2 V = \frac{-\rho}{\varepsilon_0} = \frac{-e}{\varepsilon_0}(n_i - n_e) = \frac{-e}{\varepsilon_0} n_\infty [1 - \exp(\frac{eV}{kT_e})]$$

$eV \ll kT_e$, exponential can be approximated by linear term ➔

$$\nabla^2 V = \frac{-e}{\varepsilon_0} n_\infty [\frac{-eV}{kT_e}] = \frac{e}{\varepsilon_0} n_\infty \frac{eV}{kT_e} = \frac{V}{\lambda_D^2}$$

$$\lambda_D = (\varepsilon_0 kT_e / e^2 n_\infty)^{1/2}$$

$$\nabla^2 V = \frac{V}{\lambda_D^2} \rightarrow V \sim \exp \pm \frac{x}{\lambda_D}$$

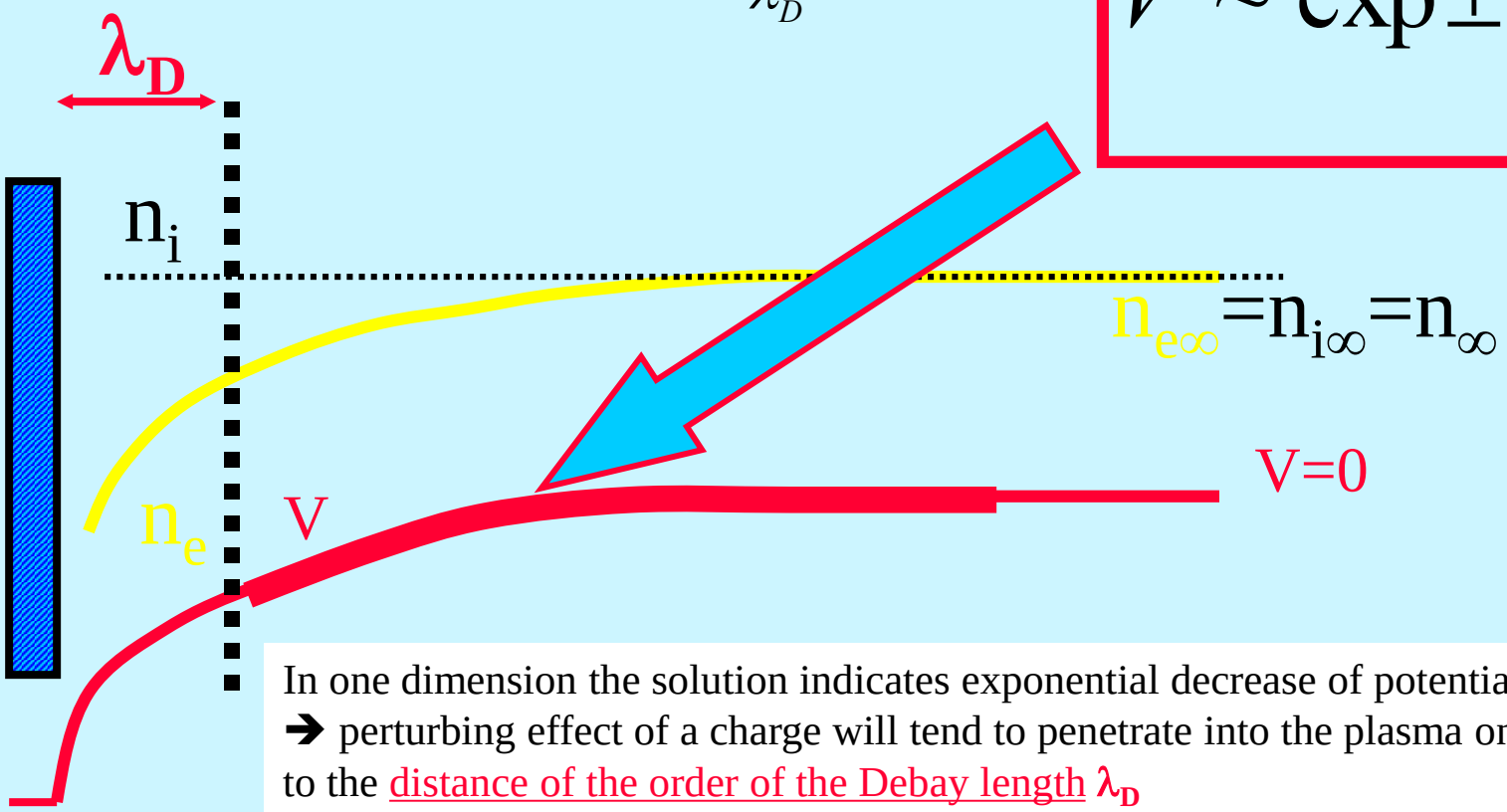

In one dimension the solution indicates exponential decrease of potential ➔ perturbing effect of a charge will tend to penetrate into the plasma only to the distance of the order of the Debay length λ_D

Linear approximation just to understand problem

Debye shielding

Spherical symmetry

$$V = \frac{e}{r}\exp(-r/\lambda_{DX})$$

$$\lambda_{DX} = (kT_e / 4\pi e^2 n_\infty)^{1/2}$$

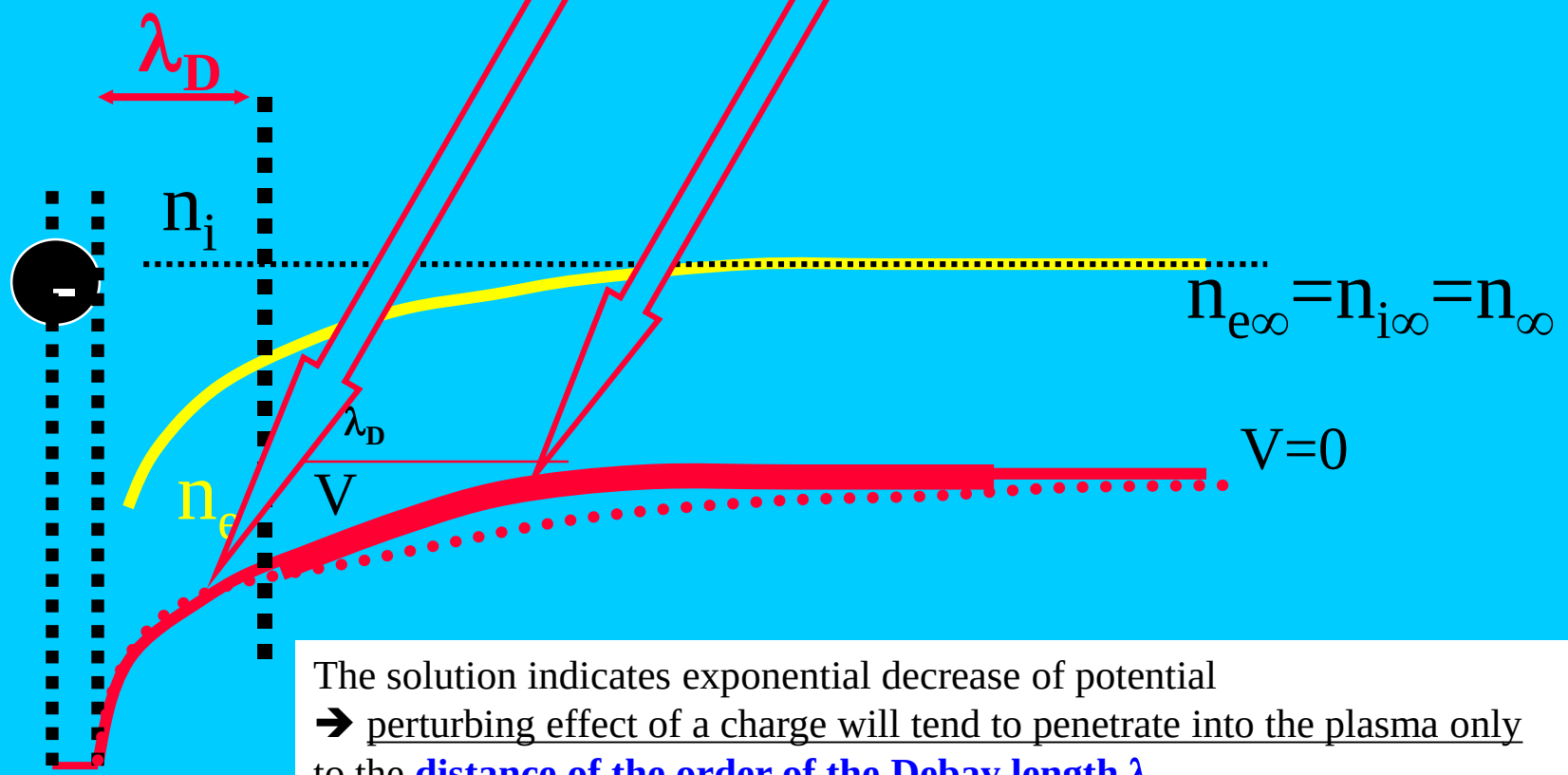

The solution indicates exponential decrease of potential
➔ perturbing effect of a charge will tend to penetrate into the plasma only to the **distance of the order of the Debay length** λ_D

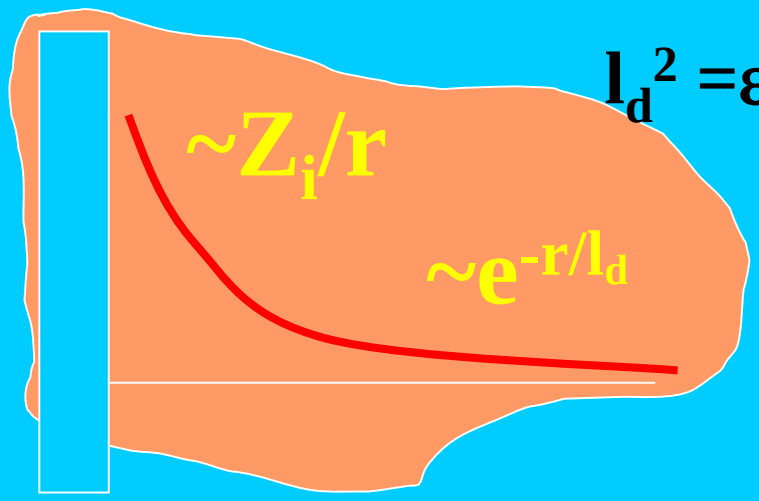

$$l_d^2 = \varepsilon_0 kT/ne^2$$

$$\phi(r) = (Z_i e/4\pi\varepsilon_0)/r \; {}_{*}e^{-r/l_d}$$

$$\sigma_c(v) = 2\pi \int b \, db$$

Problem can be ….

calculation

$$l_d = 69\sqrt{\frac{T}{n}}, \quad T \text{ in } K, n \text{ in } m^{-3}$$

at 1000K, n=4.8×10^{12}m^{-3}= 4.8×10^{6} cm^{-3}

l_d=1 mm = 0.001m

at 10K, n=1×10^{10}m^{-3}= 1×10^{4} cm^{-3}

l_d~2 mm ~ 0.002m

$$l_d = 69\sqrt{\frac{T}{n}}, \quad T \text{ in } K, n \text{ in } m^{-3}$$

$$\lambda_{De} \equiv \sqrt{\frac{\epsilon_0 T_e}{n_e e^2}} \simeq 7434\sqrt{\frac{T_e(\text{eV})}{n_e(\text{m}^{-3})}}\ \text{m}, \quad \text{electron Debye length.}$$

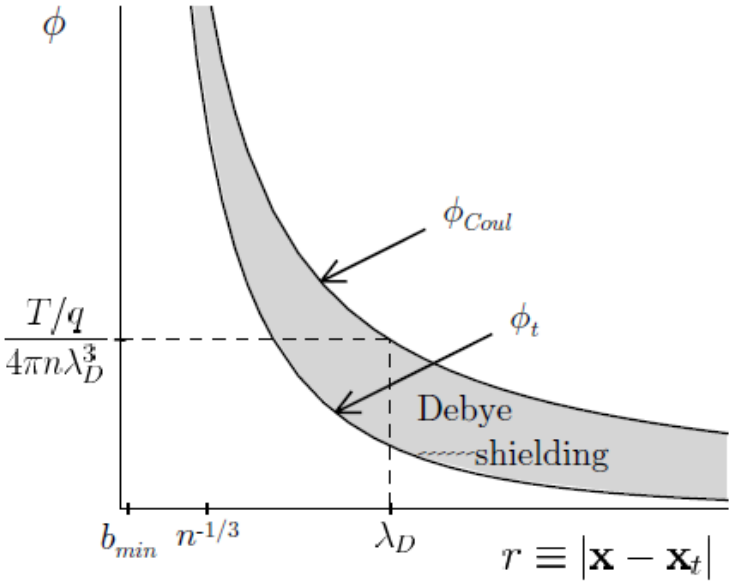

Figure 1.1: Potential ϕ_t around a test particle of charge q_t in a plasma and Coulomb potential ϕ_{Coul}, both as a function of radial distance from the test particle. The shaded region represents the Debye shielding effect. The characteristic distances are: λ_D, Debye shielding distance; $n_e^{-1/3}$, mean electron separation distance; $b_{\text{min}}^{\text{cl}} = q^2/(\{4\pi\epsilon_0\}T)$, classical distance of "closest approach" where the $e\phi/T << 1$ approximation breaks down.

$$l_d^2 = \frac{\varepsilon_0 k T_1 T_2}{e^2 (Z_1^2 n_{10} T_2 + Z_2^2 n_{20} T_1)}$$

For quasineutral plasma,
$n_{10} = n_{20} = n/2 =$ with $T_1 = T_2$ we obtain

$$l_d^2 = \frac{\varepsilon_0 k T}{n e^2}$$

$$b_0 = \frac{Z_1 Z_2 e^2}{4\pi\varepsilon_0 \mu g^2}$$

$$b_0 = \frac{e^2}{4\pi\varepsilon_0 \mu g^2}$$

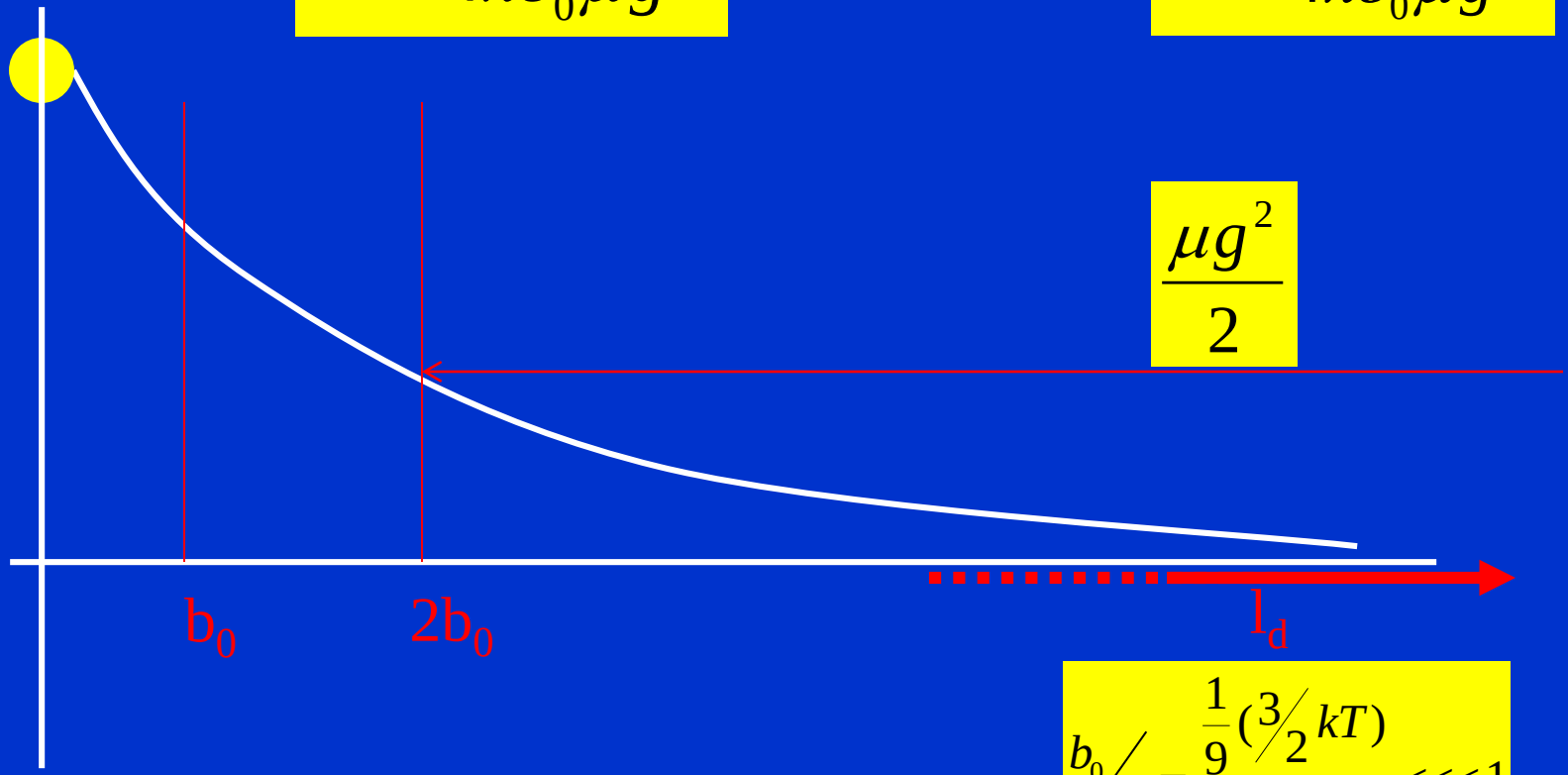

$$\frac{b_0}{l_d} = \frac{\frac{1}{9}(\frac{3}{2} kT)}{N \frac{1}{2} \mu g^2} <<< 1$$

Oscilation

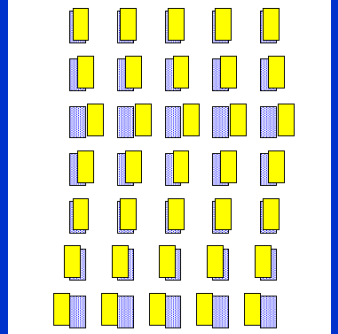

A plasma oscillation: displaced electrons oscillate around fixed ions. The wave does not necessarily propagate.

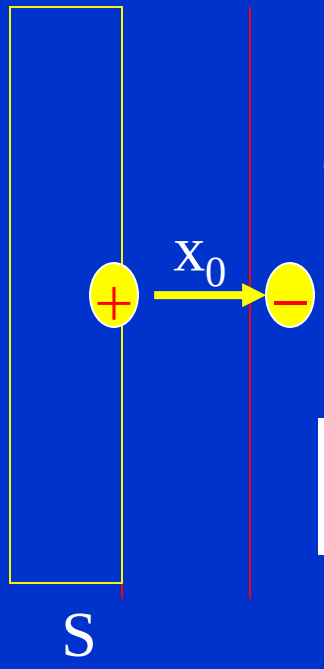

Gaus equation

$$\oint_s \vec{E}.d\vec{S} = Q/\varepsilon_0$$

$$E = enx \ / \varepsilon_0$$

$$m_e d^2(x)/dt^2 = -eE$$

$$\varpi_p = (4\pi ne^2/m_e)^{1/2}$$

$$d^2x \ /dt^2 = -\varpi_p^2 x$$

Langmuir, or plasma, frequency

$$f_p = 9\sqrt{n(10^{12}\,\mathrm{cm}^{-3})}\ \mathrm{GHz}$$

$$l_d \varpi_p = (2T/m_e)^{1/2} \approx thermal \quad electron \quad velocity$$

oscilations and collisions

$$\omega_p = (4\pi n e^2 / m_e)^{1/2}$$

$$\tau_{collision} \sim 1/\omega_{collision}$$

Condition of ideal plasma

$$\omega_p / \omega_{collision} > 1$$

Many types of collisions …..

Coulomb Logarithm

Coulombic interaction

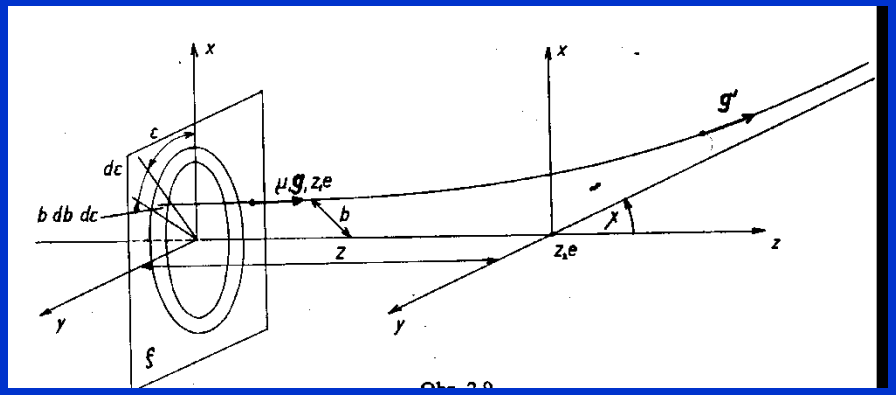

$$F = -\frac{\mathrm{d}}{\mathrm{d}t}\sum_{(i)} p_{1i} = -\frac{g}{g}\mu\sum_{(i)}\frac{\mathrm{d}}{\mathrm{d}t}g_z\,,$$

Coulombovský rozptyl

Coulombic interaction … formula for angle

Literatura:
„Velký Kracík“ … čísla rovnic…

Coulomb Logarithm

kde suma přes i značí sečítání přes všechny částice svazku. Výraz $\sum_{(i)}(\mathrm{d}g_z/\mathrm{d}t)$ je možno celkem snadno určit: fyzikálně totiž znamená změnu relativní rychlosti svazku částic za jednotku času, nebo — což je totéž — změnu relativní rychlosti jedné částice svazku vlivem srážky, vynásobenou počtem srážek za jednotku času (předpokládáme, že interakci svazku můžeme rozdělit na jednotlivé binární srážky).

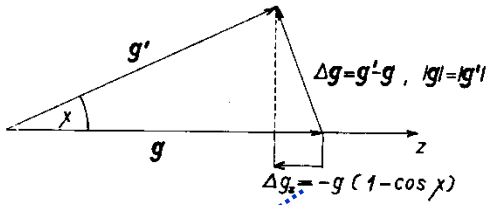

Obr. 2.10.

Změnu relativní rychlosti jedné částice svazku Δg_z určíme snadno z obr. 2.10. Snadno zjistíme, že

(2.136) $$\Delta g_z = -g(1-\cos\chi) = -2g\sin^2\frac{\chi}{2}.$$

Počet srážek za jednotku času závisí zřejmě na průřezu svazku; za jednotku času „dosáhnou“ silového centra pouze ty částice, jejichž vzdálenost $Z \leqq g \,.\, 1$ sec. Počet částic, které projdou elementární plochou $b\,\mathrm{d}b\,\mathrm{d}\varepsilon$ za jednotku času a „dosáhnou“ silového centra, pak zřejmě bude

(2.137) $$g n_1 b\,\mathrm{d}b\,\mathrm{d}\varepsilon\,,$$

kde n_1 je koncentrace částic svazku. Vynásobíme-li nyní (2.136) výrazem (2.137) a zintegrujeme-li výsledek přes celou rovinu ξ, dostaneme, že

(2.138) $$\sum_{(i)}\frac{\mathrm{d}}{\mathrm{d}t}g_z = \int_0^\infty \mathrm{d}b\int_0^{2\pi}\mathrm{d}\varepsilon\left(-2g\sin^2\frac{\chi}{2}g n_1 b\right)$$

a odtud

(2.139) $$F = \frac{g}{g}\,2g^2 n_1\mu\,2\pi\int_0^\infty b\sin^2\frac{\chi}{2}\,\mathrm{d}b\,.$$

Uvážíme-li nyní, že podle (2.106) $\operatorname{tg}\chi/2 = b_0/b$, můžeme dále psát, že

(2.140) $$F = \frac{g}{g}\,\mu\,4\pi n_1 g^2 b_0^2\int_0^\infty\frac{b\,\mathrm{d}b}{b_0^2+b^2}\,.$$

Integrál

(2.141) $$L = \int_0^\infty\frac{b\,\mathrm{d}b}{b_0^2+b^2}$$

$$F = \frac{g}{g}\,\mu\, 4\pi n_1 g^2 b_0^2 \int_0^\infty \frac{b\,\mathrm{d}b}{b_0^2 + b^2}\,.$$

$$L = \int_0^\infty \frac{b\,\mathrm{d}b}{b_0^2 + b^2}$$

ln(E.kinetic/E.potential) at distance l_d

Už jsme ukázali, že platí….

$$b_0 = \frac{e^2}{4\pi\varepsilon_0 \mu g^2} \qquad l_d^2 = \frac{\varepsilon_0 kT}{ne^2}$$

$$b_0/l_d = \frac{\frac{1}{9}(\frac{3}{2}kT)}{N\frac{1}{2}\mu g^2} <<< 1$$

logaritmicky diverguje pro velké hodnoty parametru b. Abychom dostali pro F konečné hodnoty, musíme v L nějakým způsobem omezit horní integrační mez.

V předchozím odstavci jsme si ukázali, že efektivní interakční potenciál částic je řádově dosahu l_d; binární coulombovské srážky je pak možno uvažovat pouze pro srážkový parametr $b \leqq l_d$. Za horní integrační mez L je tedy možno zvolit l_d. Dostaneme

(2.142) $$L = \int_0^{l_d} \frac{b\,\mathrm{d}b}{b_0^2 + b^2} = \ln \sqrt{\left(\frac{b_0^2 + l_d^2}{b_0^2}\right)}\,.$$

Jestliže dále platí, že $l_d \gg |b_0|$, můžeme (2.142) přepsat do tvaru

(2.143) $$L = \ln\left(\frac{l_d}{|b_0|}\right) = \ln \frac{l_d}{\frac{Z_1 Z_2 e^2}{4\pi\varepsilon_0 \mu g^2}}\,,$$

kde jsme za b_0 dosadili (2.97) a síla F, určená rovnicí (2.140), má nyní tvar

(2.144) $$F = L \frac{g}{g^3} \frac{Z_1^2 Z_2^2 e^4}{4\pi\varepsilon_0} \frac{n_1}{\mu}\,.$$

Veličina L určená rovnicí (2.143) se nazývá coulombovský logaritmus.

Předpokládali jsme, že platí

(2.145) $$l_d \gg b_0\,.$$

Tato podmínka však plyne přímo z předpokladů (2.120), které mají platit pro libovolné r. Položme tedy $r = l_d$ a předpokládejme pro jednoduchost, že $Z_1 = Z_2 = 1$. Sečtením nerovností (2.120) ($\varphi(r)$ bereme v prvním přiblížení jako coulombovský) dostaneme

(2.146) $$\frac{2e^2}{4\pi\varepsilon_0}\frac{1}{l_d} \ll k(T_1 + T_2)\,,$$

což je možno přepsat jako

(2.147) $$l_d \gg \frac{2e^2}{4\pi\varepsilon_0 k(T_1 + T_2)}\,.$$

Protože ale $3k(T_1 + T_2) \sim \mu g^2$, je možno (2.147) dále přepsat na

(2.148) $$l_d \gg \frac{6e^2}{4\pi\varepsilon_0 \mu g^2} \sim b_0\,.$$

Odtud již vidíme, že nerovnost (2.145) je již splněna, platí-li (2.120), nebo jinými slovy, předpokládáme (stejně jako v 1. kapitole), že interakční energie částic je mnohem menší ve srovnání s jejich tepelnou energií. K tomuto výsledku je možno dojít ještě trochu jiným způsobem. Aby „ořezání“ integrálu L(2.141) mělo fyzikální smysl,

Coulomb logarithm

F= const .L

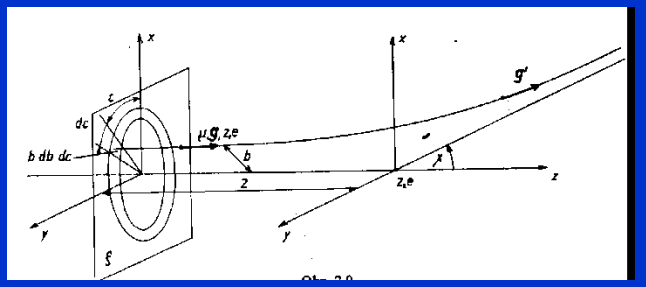

(2.140) $$F = \frac{g}{g}\,\mu\, 4\pi n_1 g^2 b_0^2 \int_0^\infty \frac{b\,\mathrm{d}b}{b_0^2 + b^2}.$$

Integrál

(2.141) $$L = \int_0^\infty \frac{b\,\mathrm{d}b}{b_0^2 + b^2}$$

(2.151) $$|F| = \text{konst}\, L,$$

kde L je dáno rovnicí (2.142), resp. (2.143). Sledujme dále, jak závisí $|F|$ na úhlu rozptylu částic. Na základě (2.106) můžeme tvrdit, že pro $b \gg b_0$ je

(2.152) $$\chi = \frac{2b_0}{b} \ll 1$$

a tedy rozptyl na malé úhly odpovídá dalekým průletům. Hranici mezi dalekými a blízkými průlety stanovme pro $b = 2b_0$. Rovnici (2.151) můžeme nyní psát ve tvaru

(2.153) $$|F| = \text{konst} \int_0^{l_d} \frac{b\,\mathrm{d}b}{b_0^2 + b^2} = \text{konst}\,(L_{\mathrm{b.p.}} + L_{\mathrm{d.p.}}),$$

kde

(2.154) **closed** $$L_{\mathrm{b.p.}} = \int_0^{2b_0} \frac{b\,\mathrm{d}b}{b_0^2 + b^2} = \ln 3 \sim 1$$

je coulombovský logaritmus odpovídající blízkým průletům a

distant

(2.155) $$L_{\mathrm{d.p.}} = \int_{2b_0}^{l_d} \frac{b\,\mathrm{d}b}{b_0^2 + b^2} = \ln \frac{l_d}{b_0} \sim \ln 3 \sim \ln \frac{l_d}{b_0} = L \gg 1$$

je coulombovský logaritmus odpovídající dalekým průletům. Z (2.153) je zřejmé, že střední sílu, která působí na částici 2 ze strany svazku částic 1, můžeme rozdělit na dvě části a to na sílu $F_{\mathrm{b.p.}}$, odpovídající blízkým průletům, a $F_{\mathrm{d.p.}}$, odpovídající dalekým průletům; pro $F_{\mathrm{b.p.}}$ a $F_{\mathrm{d.p.}}$ platí

(2.156) $$|F_{\mathrm{b.p.}}| \sim L_{\mathrm{b.p.}}$$

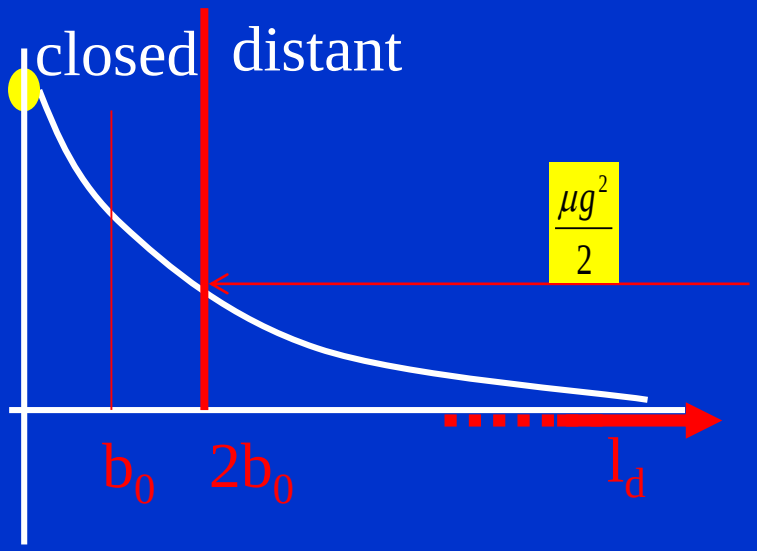

$$\frac{b_0}{l_d} = \frac{\frac{1}{9}\left(\frac{3}{2}kT\right)}{N\,\frac{1}{2}\mu g^2} \ll\ll 1$$

$F_{dp} / F_{bp} \sim L >> 1$

F= const .L

Temperature dependence

V závěru tohoto odstavce uvedeme ještě několik poznámek, týkajících se coulombovského logaritmu L. Z (2.143) vidíme, že L závisí logaritmicky na μg^2. V důsledku této logaritmické závislosti je možno v mnoha případech nahradit μg^2 střední hodnotou této veličiny nebo tepelnou rychlostí částic, tj. můžeme položit $\mu g^2 \sim \frac{3}{2}k(T_1 + T_2)$. Abychom si utvořili představu, jak závisí L na teplotě a koncentraci, předpokládejme pro jednoduchost, že $T_1 = T_2 = T$. Coulombovský logaritmus má pak jednoduchý tvar

(2.159) $$L = \ln\left[\frac{12\pi}{n^{1/2}}\left(\frac{\varepsilon_0 kT}{e^2}\right)^{3/2}\right].$$

V jednoduchém případě, kdy $\mu g^2 \sim \frac{3}{2}k(T_1 + T_2)$, $T_1 = T_2 = T$ a $|Z_1| = |Z_2| = 1$, je možno (2.161) přepsat na tvar

(2.162) $$L_{kv} = L_{kl} + \ln\left(\frac{4{,}2 \cdot 10^5}{T}\right)^{1/2},$$

kde L_{kl} je dáno vztahem (2.159). Hodnoty coulombovského logaritmu vypočtené z (2.159) a (2.161) jsou uvedeny v tab. 1; nejsou zde uvedeny hodnoty coulombovského logaritmu pro vysoké koncentrace a nízké teploty, protože v těchto případech je námi uvedená teorie neplatná.

kl - klasický
kv - kvantový

Coulomb logarithm

L~ 5 – 20 ……

F= const .L

Tabulka 1. Hodnoty coulombovského logaritmu L.

Koncentrace elektronů [m^{-3}]	Teplota K									
	50	100	5.10^2	10^3	5.10^3	10^4	5.10^4	10^5	5.10^5	10^6
10^{10}	10,69	11,73	14,14	15,18	17,60	18,63	21,05	22,09	24,42	25,11
10^{11}	9,54	10,58	12,99	14,03	16,44	17,48	19,88	20,94	23,26	23,96
10^{12}	8,39	9,42	11,84	12,88	15,29	16,33	18,75	19,79	22,11	22,81
10^{13}	7,23	8,27	10,69	11,73	14,14	15,18	17,60	18,63	20,96	21,65
10^{14}	6,08	7,12	9,54	10,58	12,99	14,03	16,44	17,48	19,81	20,50
10^{15}	4,93	5,97	8,39	9,42	11,84	12,88	15,29	16,33	18,66	19,36
10^{16}	—	4,82	7,23	8,27	10,69	11,73	14,14	15,18	17,51	18,20
10^{17}	—	—	6,08	7,12	9,54	10,58	19,99	14,03	16,36	17,05
10^{18}	—	—	4,93	5,97	8,39	9,42	11,84	12,88	15,21	15,90
10^{19}	—	—	—	4,82	7,23	8,27	10,69	11,73	14,06	14,75
10^{20}	—	—	—	—	6,08	7,12	9,54	10,58	12,90	13,60
10^{21}	—	—	—	—	4,93	9,57	8,39	9,42	11,75	12,45
10^{22}	—	—	—	—	—	4,92	7,23	8,27	10,60	11,30
10^{23}	—	—	—	—	—	—	6,08	7,12	9,45	10,14
10^{24}	—	—	—	—	—	—	4,93	5,97	8,30	8,99

Literatura ke kap. 2.

Jancel R., Kahan Th.: Electrodynamics of plasmas. J. Wiley & Sons, London (1966).
Delcroix J. L.: Plasma physics. J. Wiley & Sons, London (1965).
Landau L. D., Lifšic E. M.: Kvantovaja mechanika. Moskva (1963).
Sivuchin D. V.: Voprosy těorii plazmy *4.*, red. M. A. Leontovič, Moskva (1964).
Trubnikov B. A.: Voprosy těorii plazmy *1.*, red. M. A. Leontovič, Moskva (1963).
Spitzer L.: Physics of fully ionized gases. Interscience, New York (1956) (ruský překlad Spitzer L.: Fizika polnosťju ionizovannogo gaza. Moskva (1965)).

Electron collisions with atoms, ions, molecules, and surfaces: Fundamental science empowering advances in technology

Klaus Bartschat[a,1] and Mark J. Kushner[b]

Edited by David A. Weitz, Harvard University, Cambridge, MA, and approved May 16, 2016 (received for review April 16, 2016)

Electron collisions with atoms, ions, molecules, and surfaces are critically important to the understanding and modeling of low-temperature plasmas (LTPs), and so in the development of technologies based on LTPs. Recent progress in obtaining experimental benchmark data and the development of highly sophisticated computational methods is highlighted. With the cesium-based diode-pumped alkali laser and remote plasma etching of Si_3N_4 as examples, we demonstrate how accurate and comprehensive datasets for electron collisions enable complex modeling of plasma-using technologies that empower our high-technology–based society.

cesium-based diode-pumped alkali laser (DPAL)

Species in the Model:

$Cs(6^2S_{1/2})$, $Cs(6^2P_{1/2,3/2})$, $Cs(5^2D_{5/2,3/2})$,
$Cs(7^2S_{1/2})$, $Cs(7^2P_{1/2,3/2})$, $Cs(Ryd)$, Cs^+, Cs_2, Cs_2^+;
$He(1s^2)^1S$; $He(1s2s)^{3,1}S$; $He(1s2p)^3P,^1P$;
$He(1s3s)^3S,^1S$; $He(1s3p)^3P,^1P$; He^+, He_2^*, He_2^+;
N, $N(^2D)$, N^+; N_2, $N_2(v)$, $N_2(A)$, $N_2(B,C)$, N_2^+, N_4^+

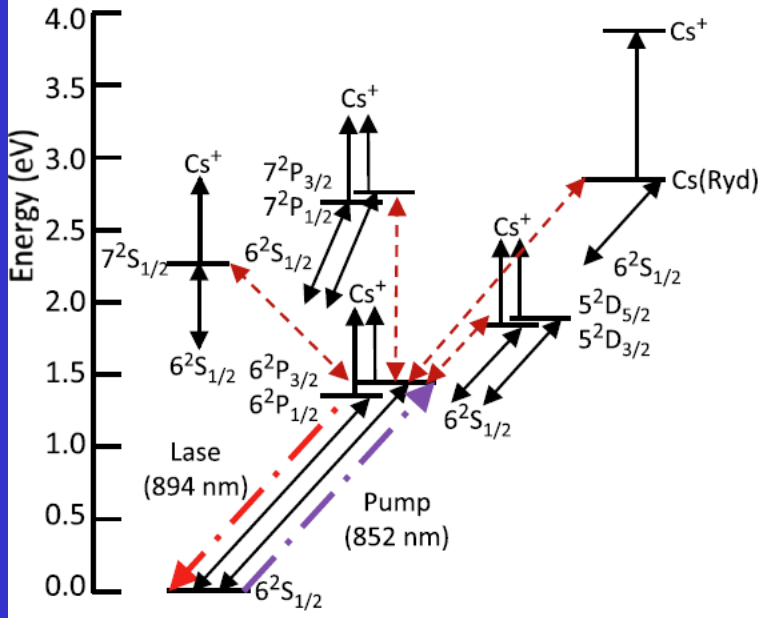

Fig. 1. Scheme for modeling a Cs-based DPAL. The solid lines denote electron collisions that induce transitions between the ground state and all excited states, and to the ion. The dotted lines are representative of electron impact collisions that produce transitions between all excited states. Additional reactions include collisions between atoms and molecules, and radiative transitions. Also shown (thick dashed-dotted lines) are the pump and lasing transitions.

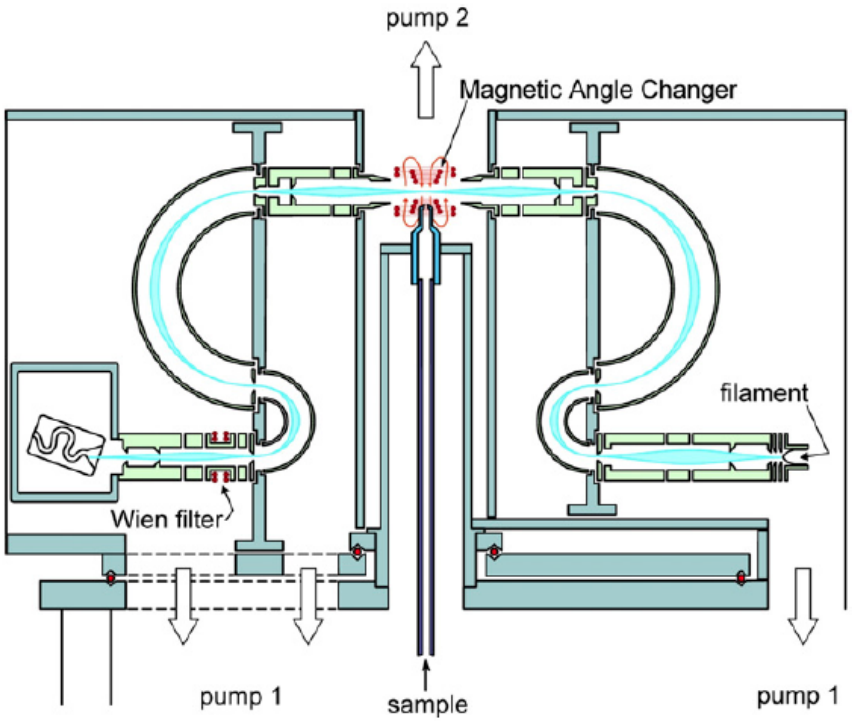

Fig. 3. The electron spectrometer of Allan (6).

Two Experimental Advances. The basic workhorse used in a large number of electron-scattering studies is the electron spectrometer. Free electrons are formed into a beam and energy selected by various combinations of electrostatic and magnetic fields. The use of electrostatic fields is most common, because they are more easily controlled and shielded than their magnetic counterparts. This is particularly important when it is essential to preserve the direction of low-energy electrons following the collision process.

Fig. 3 exhibits an example of such a spectrometer (6), which combines the characteristics of a conventional electrostatic device with an important innovation. It can be used for elastic scattering and electron impact excitation studies. The electron gun consists of a source of electrons produced by thermionic emission from a heated filament. The electrons are collimated and focused by an electrostatic lens system onto the input aperture of a double hemispherical energy selector. Those electrons within a narrow band of energies satisfying the criteria for transmission through the selector are then focused on the gas beam produced by a nozzle arrangement. Scattered electrons from the interaction region traveling in the direction of the scattered electron analyzer are similarly focused onto the input aperture of its double hemispherical analyzer, and the transmitted electrons are finally being focused into a single-channel electron multiplier detector.

One drawback of conventional electron spectrometers is that the angular range of the electron analyzer is limited by the physical presence of other components of the spectrometer. This limitation was overcome by Read and Channing (4) who applied a localized static magnetic field to the interaction region of a conventional spectrometer. The incident electron beam and the scattered electrons are, respectively, steered to and from the interaction region through angles set by the field (hence, the common name "magnetic angle changer" or "MAC"). This steering means that electrons normally scattered into inaccessible scattering angles are rotated into the accessible angular range of the electron analyzer while the magnetic field design is such that it leaves the angular distribution of the electrons undistorted. The spectrometer shown in Fig. 3 has a MAC fitted, thereby enabling the full angular range 0–180° to be accessed.

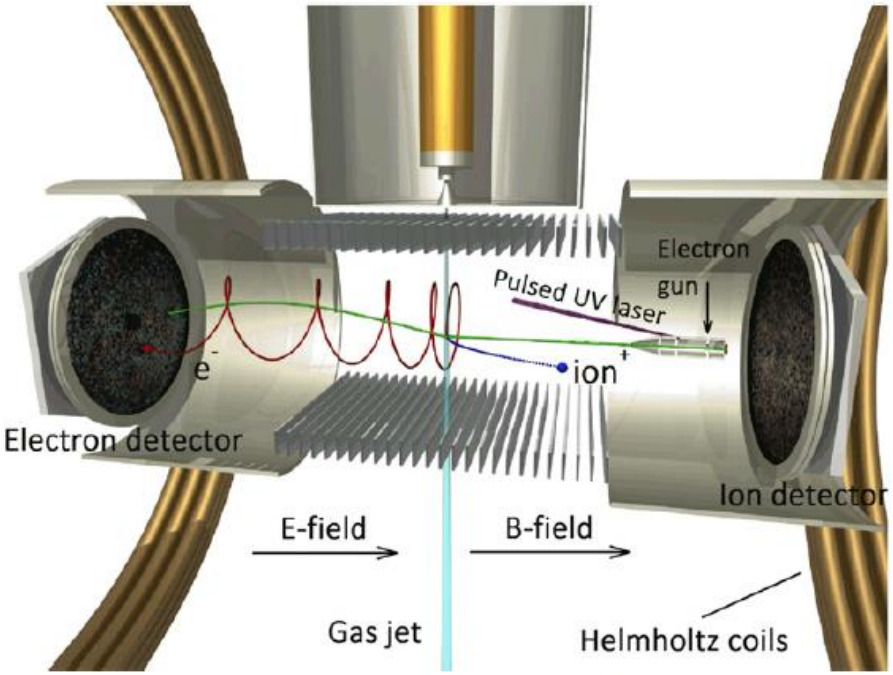

Fig. 4. The reaction microscope of Ren et al. (7). The projectile-electron beam is crossed with a supersonic gas beam. The projectile is created by a pulsed UV laser illuminating a photocathode. The outgoing electrons and ions are extracted by a homogeneous electric (E) field, created by a series of parallel electrodes, and detected by 2D position- and time-sensitive multihit detectors. A pair of Helmholtz coils generates a uniform magnetic (B) field, which forces the electrons into cyclotron trajectories and guides them onto the detector. The time of flight for each particle from the collision region to the respective detector is determined by the clock signals from the projectile pulse and the detectors.

A recent version, developed by Ren et al. (7) to study single ionization processes is shown in Fig. 4. The RM operates on entirely different principles from conventional electron spectrometers. Briefly, a pulsed beam of electrons crosses a supersonic atom beam. The ejected electrons and the recoiling ions are extracted in opposite directions by a weak uniform electric field parallel to the incident electron beam direction. A uniform magnetic field is also applied in this direction to confine electrons emitted perpendicular to the electric field. After passing through field-free drift regions, the slow ejected electrons are detected in two time- and position-sensitive multihit detectors, allowing for the vector momenta of all particles to be calculated. Unlike most conventional coincidence electron spectrometers, which only enable measurements in a single plane at any one time, this technique allows for data to be collected over a large part of the entire 4π solid angle simultaneously.

Without going into detail, we emphasize the difficulty of obtaining absolute cross sections. Most of the time, some cross-normalization to "known" (or believed to be known) other data, such as cross sections for another target in a mixed-flow setup, data for angle-integrated state-to-state transitions after performing angle-differential measurements, total (summed over all accessible exit channels) cross sections, or even theoretical predictions, is required. Only in exceptional cases, absolute total ionization or recombination cross sections can be obtained directly (after carefully determining many experimental parameters) and fed into plasma models. An example is the crossed-beam apparatus developed by Müller and collaborators (8, 9).

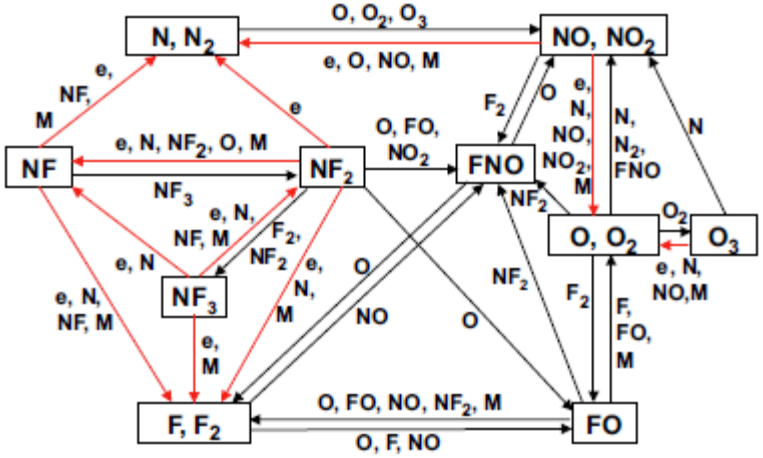

Fig. 2. Reaction mechanism in NF_3/O_2 mixtures. "M" denotes a third body.

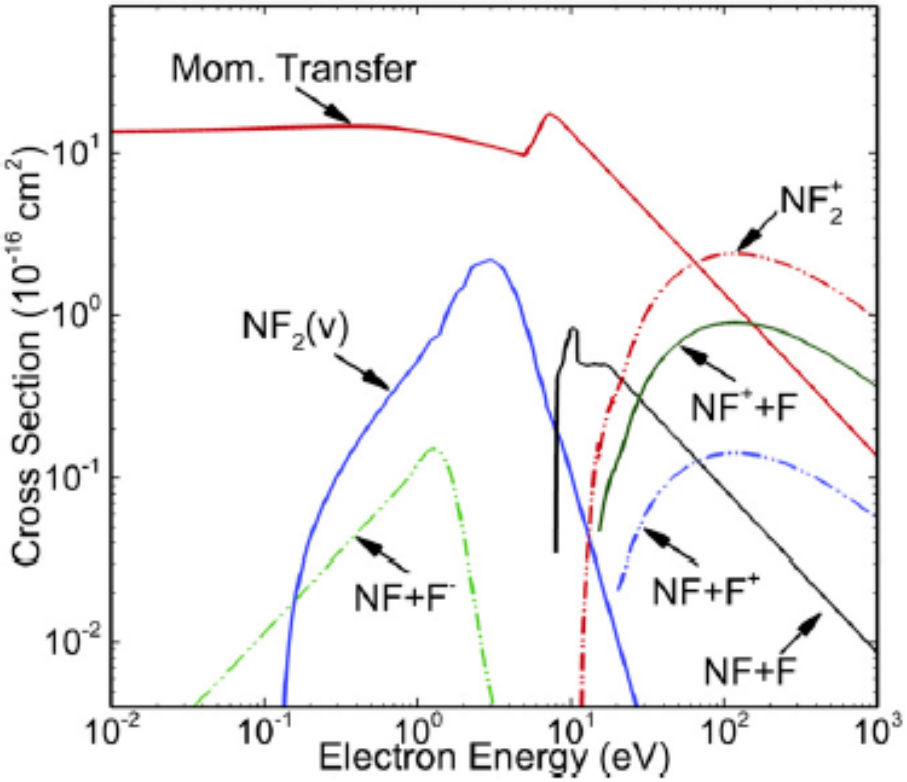

Fig. 12. Some cross sections used for the processes depicted in Fig. 2. The data for electron collisions with NF_2, including momentum transfer, vibrational excitation (v), and dissociation into combinations of various molecular ions were generated by Tennyson and collaborators (42) with the UK molecular R-matrix codes (43).